Experimental comparison of slalom concepts

Ella Pirttikangas

Åbo Akademi University
Faculty of Science and Engineering
Laboratory of Thermal and Flow Engineering

Abstract

Studies on paper and board machine runnability began in the late 20th century and most of the studies focused on machine speed increase. Today, the most high-speed paper machines have a single-run construction and machine speeds can reach speeds over 2000 m/min. Runnability equipment is developed to enable the high velocities and the objective is to diminish the negative effects associated with the machine speed increase. Currently, studies focus on energy and cost efficiency, where finding the optimum solution for the certain framework is required.

The objective of the thesis was to study the forces and the phenomena at a single-run paper or board machine, which causes harmful effects on the web. In the thesis, a selection of runnability concepts are compared at different machine speeds and the comparison analyses their functionality, energy consumption and cost. The concepts were tested at pilot scale in the Technology Centre of Valmet in Raisio.

The comparison of the functionality focused on how the different concepts stabilised the web at the closing nip and over the rotation of the bottom cylinder. The comparison concluded that the existence of a surface pattern was beneficial both for the closing nip over pressures as well as the support over the rotation. Furthermore, having a stabiliser nozzle targeting the closing nip was useful especially at low machine speeds and the suction roll concepts were found to be over dimensioned at machine speeds below 1400 m/min.

The energy consumption and cost evaluation, combined with the functionality analysis suggests that the concepts using a suction roll are the most fitting for higher velocities, as the functionality of the concepts with the passive bottom rolls decrease or the operational cost become higher compared to the suction roll concepts.

Keywords: Slalom concepts, functionality, cost-efficiency

Acknowledgements

First and foremost, I would like to extend my gratitude to the M.Sc. Lari Heinonen and B.Sc. Paavo Sairanen, who gave me the opportunity to dive in to the peculiar world of paper and board machine runnability. Their help and support have been invaluable and I am truly grateful that they kept me on track and answered every question or concern I might have had during the process.

I want to thank my supervisor Professor Henrik Saxén, who showed genuine interest in my work and encouraged me to challenge myself and gave great guidance when needed. His help was irreplaceable in creating the simulation models used to explain some of the phenomena and I am grateful for his input during the writing process and for evaluating my work.

As the pilot plant trials are a major part of my thesis I cannot forget the great input of B.Sc. Kalle Muhonen. His input was key in executing the experiments and I thank him for having the patience to explain the measuring systems and for taking the time to support me in my thesis, even though it was not expected of him. Additionally, I shall not forget the whole team at the Valmet Technology Centre, who enabled the trials and rebuilds of the concepts and made it possible to keep the experiments within schedule. I want to also thank the team in Rautpohja and B.Sc. Reijo Rautiainen, who helped in creating the economic evaluation of the concepts.

And of course, I would like to thank for the love and support I have received from my family. Thank you for supporting me throughout my studies and my thesis work and a special thanks to my brother, whose technical knowledge and our shared interest in understanding how things work have been a great asset throughout my studies and thesis work. And last but definitely not the least, I thank my partner for his never-ending patience and support.

Ella Pirttikangas

October 2018, Turku

Contents

Nomenclature and abbreviations

A	Surface area
D_h	Hydraulic diameter
F_c	Centrifugal force
F_{con}	Contact force
F_g	Gravitational force
F_p	Pressure force
F_s	Support force
g	Gravitational constant
G_f	Groove fraction
K	Permeability constant
L	Lower nozzle
m	mass
$\dot{m}$	mass flow
m_g	Grammage
P	Power
p	Pressure
r	Cylinder radius
Re	Reynolds number
S	Perimeter
s	Position
T	Tension
U	Upper nozzle
v	Velocity

$\dot{V}$	Volumetric flow
w	Average velocity
$\bar{x}$	Surface roughness
x	Molecular fraction
y	Normalised volumetric airflow
Z	Compressibility factor

Greek

α	Closing nip tangential point angle
ε	Eddy viscosity
ζ	Friction coefficient
η	Molecular viscosity
θ	Angle between gravitational and centrifugal forces
μ	Dynamic viscosity
ξ	Correction factor
ρ	Density
τ	Shear force

Subscripts

a	Air
cs	Cross-section
dim	Dimensioned
dyn	Dynamic
f	Fabric
GR	Groove
p	Pressure

s	Suction
tot	Total
rel	Relative
RL	Roll land
v	water vapor
w	Paper web

1. Introduction

In recent years relatively large changes have occurred in the paper and paperboard industry. Within a decade the Finnish production of graphic and printing paper has declined by 43%, as seen from Figure 1 and the same development has been seen globally (Lukkari, 2018). The decrease has partly been explained by digitalisation, which has led to the decrease of newsprint production. On the other hand, digitalisation has increased the e-commerce activity, which has accelerated the packaging material production and within a decade the Finnish production of paperboard has increased by 20% (Lukkari, 2018). This shift in the market has forced companies to adapt their production in accordance, in order to cost-efficiently produce products that also have a market (Krabbe, 2017).

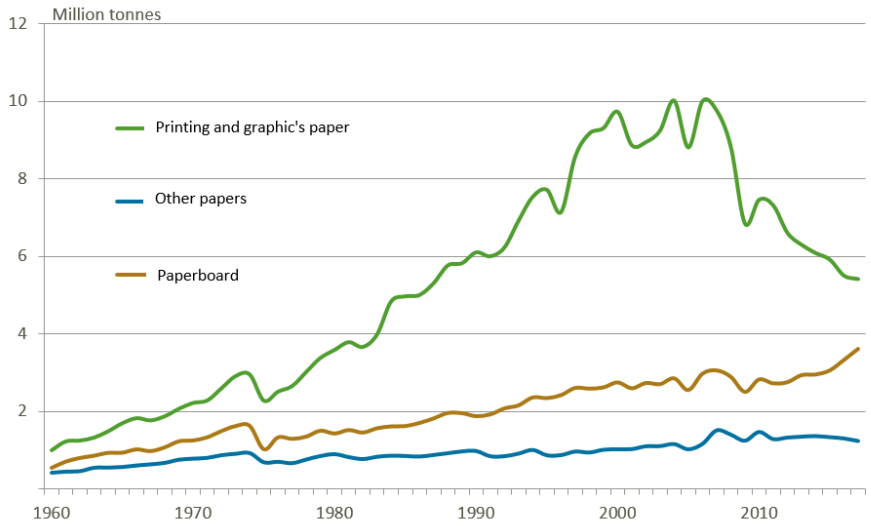

Figure 1 Finnish production of paperboard and paper (Metsäteollisuus ry, 2018).

The transition has led to shutdowns of production lines or rebuilds of the lines to produce more demanded grades, e.g. paperboard. Also, existing board lines must consider, how they could cost efficiently increase their production. Normally, production increase is done by changing the geometries of the production lines or by increasing production speed.

The production speed is limited by the runnability of the production line. Runnability is a complex concept, which defines how well the web travels through the production

line without being subject to excessive strain, which could lead to web breaks and production losses. Most high-speed machines utilise a single run or slalom construction combined with a selection of runnability equipment, such as suction rolls and stabilisers. Many of these concepts were developed in the late 20th century, when the focus lied on increasing the production speed. Now however, the focus is put on producing products both energy and cost efficiently (Siverä, 2017).

The aim of this thesis is to compare different runnability concepts and determine the concept that fits a certain production situation. The focus lies on rebuilds and upgrades of existing production lines. The thesis studies the phenomena in web handling, focusing on the closing nip region and the bottom roll, as well as addressing which variables to consider in the choice of the appropriate solution. Chosen concepts were tested in pilot plant scale in the Valmet Technology Centre in Raisio.

2. Paper and paperboard drying

The objective of a paper and board machine is to remove water from the pulp, both energy efficiently and without compromising quality of the paper. The paper machine can be divided to three sections, wire or forming section, press section and drying section.

2.1. Wire and press section

The structural properties of the paper are largely determined on the wire section. Different paper grades have different quality and furnish requirements and these should be taken into consideration in the wire section. For instance, thicker paper webs require larger drainage capacities, due to the increase in cake resistance, which results in an increase in the pressure difference over the web. Also, more beaten pulp creates a bigger pressure difference, which requires additional capacity (Häggblom-Ahnger & Komulainen, 2005, p. 137). The exiting water mostly comes from the wire section, as shown in Figure 2. The consistency at the machine head box is approximately 0.2 % - 1%, or in other words 2-10 grams fibre per kilogram water. The water is mostly removed by gravity, pulsation or vacuum, leading to a consistency increase to 15 - 25% after the wire section (Karlsson & Paltakari, 2010, p. 14).

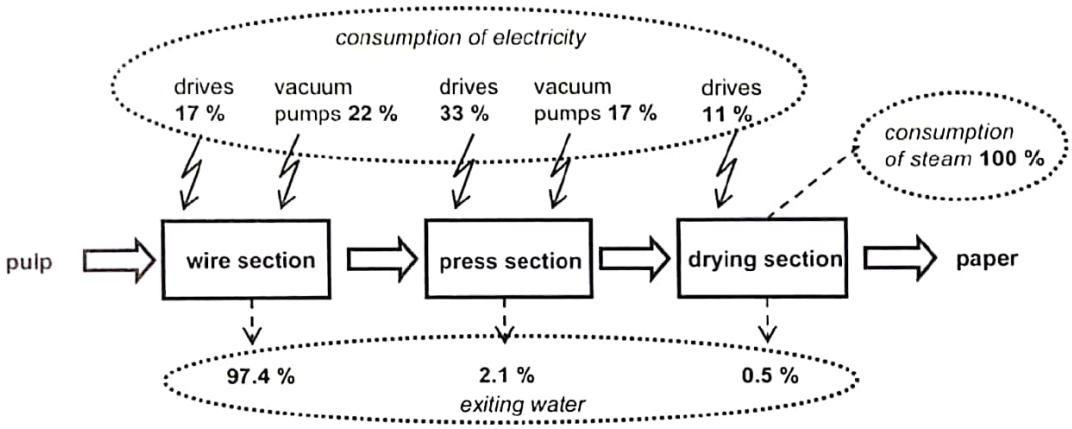

Figure 2 Energy, water and steam consumption at a paper machine (Karlsson & Paltakari, 2010)

The wire section is followed by the press section, where according to Figure 2, approximately only 2.1% of the total water amount is removed. However, the increase in dry solids is significant, from 12 - 25% to 33 - 55%, depending on the paper grade (Häggblom-Ahnger & Komulainen, 2005). Water removal is mainly done by mechanical compression. One limiting factor in the press section is the production speed. With increased production speeds, the dwell time through the nips is shortened and will consequently reduce the amount of water removed from the web. This will further complicate the transfer from the press section to the drying section and expose the drying section to runnability issues. Compensation can fortunately be done by enlarging the nips in the press section and by increasing the viscosity of the water by applying heat on the web, which can be done using, for instance steam (Häggblom-Ahnger & Komulainen, 2005, p. 159). The introduction of steam will increase the energy consumption in the press section, but on the other hand, low pressure steam from the drying section could be utilised and the added production capacity might compensate for the losses in energy.

2.2. Drying section

High drying efficiency in the press section is desirable, because the cost of removing moisture is highest in the drying section. According to McGregor et.al. (1996), the cost increase follows approximately a 1:5:220 ratio, taking the investment, energy and operation costs into account. Thus, the costs are five times bigger in the press section and 220 times bigger in the drying section compared to the wire section (McGregor & Knight, 1996). Additionally, as mentioned earlier, the increase in dry content will improve the runnability of the web due to added web strength.

The drying section functionality bases on the evaporation of water and the moisture content after the drying section is 5 - 10%. The drying section is covered by a hood to improve the energy economy of the section and to keep working conditions in the machine hall appropriate. In the traditional drying method, large diameter cylinders are internally heated by steam and the web travels over the cylinder, which enables evaporation. When the web is transferred from the press section to the drying section,

the strength of the paper is low, approximately 10 - 15% of the strength of dry paper, and the web must be supported by a fabric (Miulus, 2010, p. 4). The fabric construction can either be single-felted or double-felted, which will be discussed in Section 2.3.

As mentioned earlier, the cylinders are heated by steam and the water from the web will be evaporated from the surface, where heat is mainly transferred through conduction. At the beginning of the drying section, the steam pressures, or more practically cylinder surface temperatures, must be kept lower compared to the dry end. The steam pressures in the last dryer groups can be approximately three times higher compared to the first groups (Heikkilä, et al., 2010, p. 115). High temperatures at the wet end could cause delamination of the paper or sticking of paper on the cylinder surface due to adhesion forces or even burning of paper on the cylinder surface (Häggblom-Ahnger & Komulainen, 2005, p. 163).

Cylinder drying technology remained largely unchanged since the beginning of the 19th century, due to the advantages of the process. The controllability of the process is good and energy consumption is rather moderate. Also quality aspects, as for instance smoothness of the product, are satisfying. However, the disadvantages of the technology have been the poor energy recovery and reuse, which have become bigger problems in recent decades. Furthermore, the shrinkage and the space requirements are undesired side effects (Häggblom-Ahnger & Komulainen, 2005, p. 170).

The first studies on impingement drying were made in 1920s and became commercialised in the 1990s (Karlsson & Paltakari, 2010, p. 128). In impingement drying, hot air is blown either directly on the paper surface or indirectly through a fabric. The hot air is heated by gas burners up to 350 °C and is blown at a velocity of 90 – 120 m/s (Häggblom-Ahnger & Komulainen, 2005, p. 170). Compared with conventional cylinder drying, in impingement drying the water is removed not through conduction, but by convection and additionally by mass transfer, which increases the efficiency of the water removal. By increasing the temperature of the hot air, the tensile strength and bulk can be increased, but this will affect the optical properties and smoothness of the paper and subsequently an increase in air flow will increase web porosity (Häggblom-Ahnger & Komulainen, 2005, p. 170). Comparing energy efficiency of the impingement drying method with that of cylinder drying is complicated issue. Impingement drying uses a primary heat source, whereas the

cylinder drying uses low value steam, especially in the beginning of the drying section. The question whether to prefer the cylinder or impingement drying should thus include an analysis of the whole plant, since cylinder drying may use waste heat from other processes (Heikkilä, et al., 2010, p. 87).

Energy efficiency has increasingly become one of the key variables and the current trend is moving from efficiency increase of local processes to a mill-wide optimisation and integration. As drying is the most demanding process, with respect to steam usage, and the process affects the entire mill energy economy, there is a potential for optimisation and development in this section.

2.3. Double and single run

In single run or slalom concept, the paper web follows one dryer fabric, whereas in the double felted the web is guided by two fabrics with open draws in between the cylinders. The single- and double-felted construction is depicted in Figure 3.

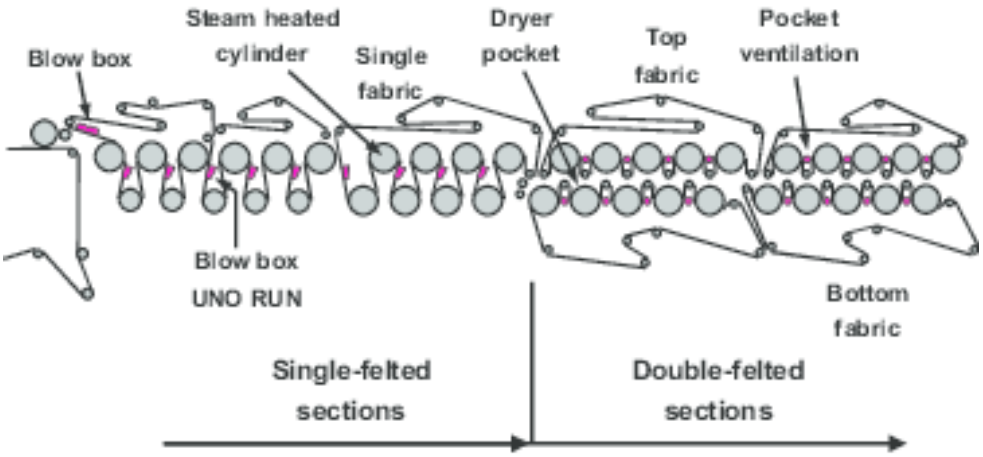

Figure 3 Single- and Double-felted construction (Pikulik & Poirier, 2003).

Because of the long unsupported draws in the double-felted construction, production speeds are hard to increase, especially at the open draws at the wet end of the drying section, where the web is still relatively weak (Sikanen, 1998, p. 8). Therefore, paper and board machines rarely use the double-felted construction in the first groups and

many double-felted constructions are transformed either completely or partly to single-felted constructions. In Figure 3, the drying section is partly single-felted in the wet end of the drying section and partly double-felted in the dry end of the drying section, where less support on the open draws is needed.

The added support provided by the drying fabric in the single-felted construction decreased web breaks and restricted shrinkage, but the evaporation was a matter of concern, especially in the loss of direct contact with the bottom steam cylinders (Kurki, et al., 2010). On the other hand, the absence of the lower fabric enabled ventilation from the basement as seen in the left-hand side of Figure 3.

Considering evaporation rate and runnability, the permeability and properties of the drying fabric are determining factors for the single run construction. From a runnability point-of-view the fabric should have low permeability, whereas higher permeability is beneficial for the evaporation rate (Karlsson, 1989, p. 4). Additionally, the air carry of the fabric should be minimised, which means the surface roughness should be kept low. However, this will followingly affect the friction factor of the fabric, which further influences the friction force between the web and the fabric (Karlsson, 1989, p. 28).

3. Forces affecting web handling in single run concepts

The moving paper web is subject to many kinds of forces in the drying section. The forces are most commonly divided into internal and external forces. The internal forces are created by the changes in the material, whereas the external forces are created by the surroundings. The main task of the web handling equipment is to disperse or reduce the forces on the web in order to prevent web fluttering, displacement and other undesired movement of the web that could eventually cause web breaks. For the studies conducted in this thesis the aerodynamic pressure forces were particularly of interest, so a special focus on these forces is made.

3.1. Internal forces and properties of various paper grades

One internal force, which occurs during drying of the paper, is the internal tension force within the paper structure, which is created by the shrinkage of the paper. Shrinkage is mostly undesired, since it will lower the strength properties of the paper, but for some grades, e.g. sack paper, high shrinkage is desired in order to increase the stretch strength (Heikkilä, et al., 2010, p. 86).

A single fibre shrinks mainly in the radial direction and only 1-2 % in the longitudinal direction (Pakarinen, et al., 2009, p. 238). Paper fibres consist of organic polymers, which interact and build hydrogen bonds between the fibres. Other important chemical bonds are the van der Waals forces in the fibres, which are an important factor in the adherence, as well as ionic and covalent bonds, which are formed by the influence of mediators (Pakarinen, et al., 2009, p. 240). In other words, the shrinkage originates from the surface tension forces between the fibres. Factors affecting the extent of shrinkage is, among others, the furnish. For instance, beaten fibres tend to swell more, leading to higher shrinkage in drying. Also, the use of virgin fibres or recycled fibres affect the shrinkage, since virgin fibres tend to swell more than recycled ones, because the ability to absorb water is higher for virgin fibres. Additionally, hemicellulose causes more swelling and is a factor in the creation of bonds between the fibres increasing the tension forces (Pakarinen, et al., 2009, pp. 251-255).

Shrinkage of the web occurs both in thickness and along its plane. The relative shrinkage is higher in thickness and can cause lumpiness of the paper if the formation of the paper is incomplete. The in-plane shrinkage of the web is moderate in machine direction due to stretchers and the cross-direction shrinkage is only somewhat restricted. The machine-direction shrinkage causes tension, which is desirable from a web handling point of view, since the tension to some extent decreases undesired fluttering (Pakarinen, et al., 2009, p. 257)

The cross-section shrinkage is commonly higher in the edges of the paper than in the middle of the web, because of frictional forces between the web and the support surfaces. These forces are usually higher in the middle of the web. Consequently, this leads to differences in the properties of the paper in the cross direction. Shrinkage can be controlled by restraining the paper web and introducing forces opposing the internal tension force. Commonly, shrinkage is controlled by implementing a single-felted construction, especially in the wet end of the drying section. The added support surface from the single-felted construction creates friction forces in the machine direction, which restrain the web. If added support is desired in single-felted drying, vacuum rolls and stabilisers can be installed to reduce shrinkage. In studies, where the paper web is moderately restrained during drying, the restrained paper has shown up to 20% higher tensile strength compared to paper subjected to unrestrained drying (Pakarinen, et al., 2009, p. 258).

Other internal forces affecting the runnability are adhesion forces, which occur between the paper web and the surrounding surfaces. Adhesion forces become harmful when they occur between the drying cylinders and the paper, since these forces tend to make the paper web stick to the dryer cylinder surface, instead of continuing in the tangential direction with the fabric.

To avoid harmful adherence of the web, the first groups in the drying section usually operate with lower steam pressures. The adhesion is stronger on wet webs (dry solids 37 – 42%) and may be explained by the formation of hydrogen bonds, since the bonds are yet to be formed in wet webs. The internal cohesion forces of the wet web are lower than the counteracting adhesion force of the cylinder surface. The imbalance of forces will make the wet web to stick on the cylinder surface even at moderate temperatures, such as 80 °C (Pakarinen, et al., 2009, p. 247). The situation becomes more

complicated when the chemical potential of the cylinder surface is changed by contaminants, which stick on the cylinder surface. This may change an initially hydrophobic surface to become hydrophilic. Furthermore, local differences in the chemical potential may occur, which complicates the situation further (Pakarinen, et al., 2009, p. 248).

Additionally, the external forces can support the undesired effects of the adhesion forces. For instance, the centrifugal forces and pressure forces contribute to the sticking of paper and the paper grade and its chemical properties contribute to the adherence. Therefore, as concluded in Leimus work (Leimu, 2008), the phenomena caused by adhesion are clearly a function of many variables and models of the force are mainly based on experiments. The repeatability of the experiments is challenging and it is difficult to find explanations of the behaviour (Leimu, 2008, p. 10). The adhesion forces occur not only between the cylinders and the paper web, but also between the paper web and the supporting fabric. This adhesion between the fabric and paper can be profitable from a web handling point-of-view, because the adhesion supports the paper to the fabric, which will work against harmful external forces, such as pressure forces.

3.2. External forces

The presence of moving surfaces and support media creates a variety of external forces. These forces are, e.g., forces due to the pressure differences over the web, frictional, gravitational and centrifugal forces. With increased velocities, these forces grow and can cause undesired fluttering, displacement or in the worst-case web breaks.

The external forces can, however, also be supportive forces, as for instance friction forces. The friction forces act between supporting media and the paper as well as between the air and paper web. Especially, the friction force between the fabric and paper web is central for the single run concepts, since it will hinder displacement and will decrease shrinkage.

The friction force is largely dependent on the friction factors. The friction factor of the supporting media and the paper will affect the web tension, which further restricts the paper web and hinders the displacement of the web. The force is, however seemingly hard to forecast, since many variables contribute to the force. Such factors are moisture content, temperature, supporting length and force as well as roughness of the surface and chemical composition of the paper web. The supporting forces are the forces intended to safeguard the web and hinder displacement.

3.2.1. Forces over the bottom roll

When the web is moving over the bottom roll it is subjected to external forces, such as gravitational and centrifugal forces. In single run concepts, the centrifugal force can cause elongation of the web, which accumulates throughout the positions. To avoid this effect, the web tension should be high enough or the web should be supported, so that the forces are neutralised (Hauser, 1991).

In the ideal case, when forces causing web fluttering and the pressure forces are neglected, the forces displacing the web are gravitational and centrifugal (Ukkola, 1997, p. 31). To ensure proper runnability, the displacing forces must be dispersed by a supporting force, F_s. Making a force balance over the infinitesimal surface, we obtain (Ukkola, 1997):

$$dF_s = dF_g + dF_c \qquad (1)$$

The supporting force is the sum of the forces ensuring the web placement. Depending on the concept used, the supporting force will be different. In the tested concepts, the supporting forces are either contact induced by web tension, pressure difference over the web or a combination of both. The supporting forces can be further described as

$$dF_s = dF_{con} + dF_p \qquad (2)$$

where the support of the friction force is neglected, since it varies largely between the fabrics used and is usually hard to determine. If Eq. (2) and expressions for centrifugal and gravitational forces are inserted into the Eq. (1), we have:

$$dF_{con} + dF_p = dm\cos\theta\, g + dm\frac{v^2}{r} \qquad (3)$$

The gravitational force affecting the displacement has to be the component parallel to the other forces, so the angle between the centrifugal vector and gravitational vector is included (Ukkola, 1997). The displacing force is the strongest at the bottom of the roll, when the angle is zero between the centrifugal force and gravitation. In Eq. (3), the mass is an infinitesimal mass over an infinitesimal area, which is why the expression is divided by area, giving:

$$\frac{F_{con}}{A} + \Delta p = \frac{m}{A}\cos\theta\, g + \frac{m \cdot v^2}{A \cdot r} \qquad (4)$$

The pressure force, F_p, is substituted with the pressure difference over the fabric and web and the equation can be further simplified, when the contact pressure caused by the web tension is included. According to Lang (2004), the contact pressure between the fabric and cylinder can be described as $p_c = \frac{T_f}{r}$, where T_f is the fabric tension and r is the cylinder radius (Lang, 2004). The same equation is assumed valid for describing the contact pressure caused by web tension. Therefore, the expression from Lang (2004) is inserted and additionally the mass per area is described as grammage.

$$\frac{T_w}{r} + \Delta p = m_g(\cos\theta\, g + \frac{v^2}{r}) \qquad (5)$$

As the gravitational constant is low compared to the centrifugal factor, the effect of the angular component can be questioned. To demonstrate the relation between the gravity and centrifugal force, the angle is varied in Eq. (5) between 0° and 360° and represented in Figure 4. Changing the angle between the forces does not substantially change the total sum of the forces. Therefore, the angular component is assumed in the later chapters to be one.

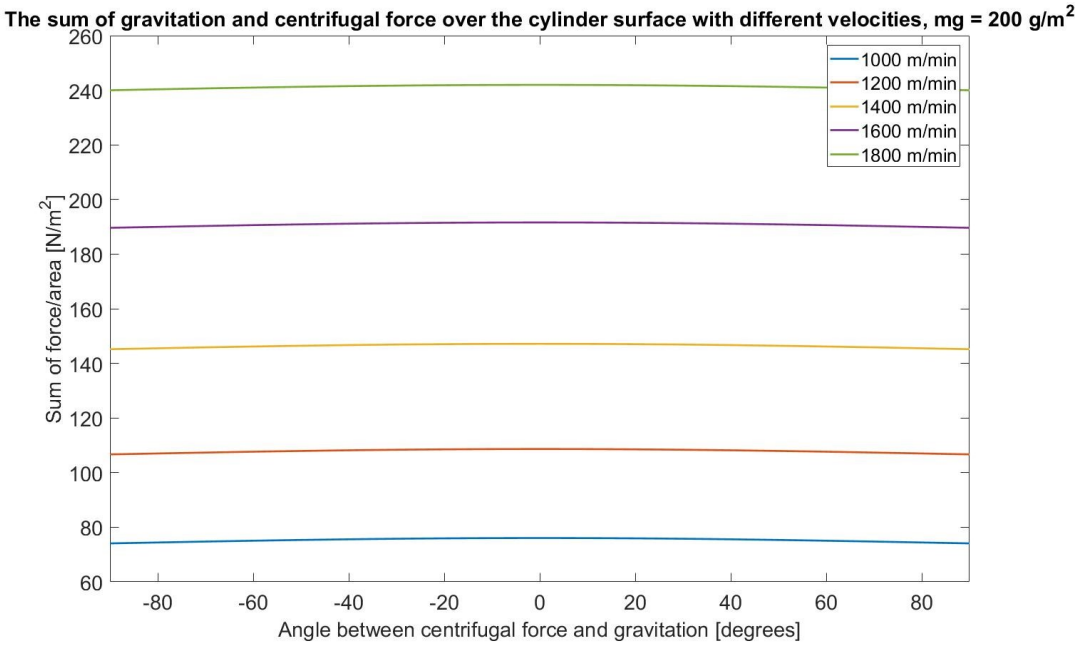

Figure 4 Summed effect of centrifugal force and gravitation against the wrap angle.

The centrifugal factor is central for the magnitude of the detaching force, which elongates the web. Since the velocity in the Eq. (5) is squared, a velocity increase will substantially increase the detaching force. The effects of velocity and grammage have been illustrated in Figure 5.

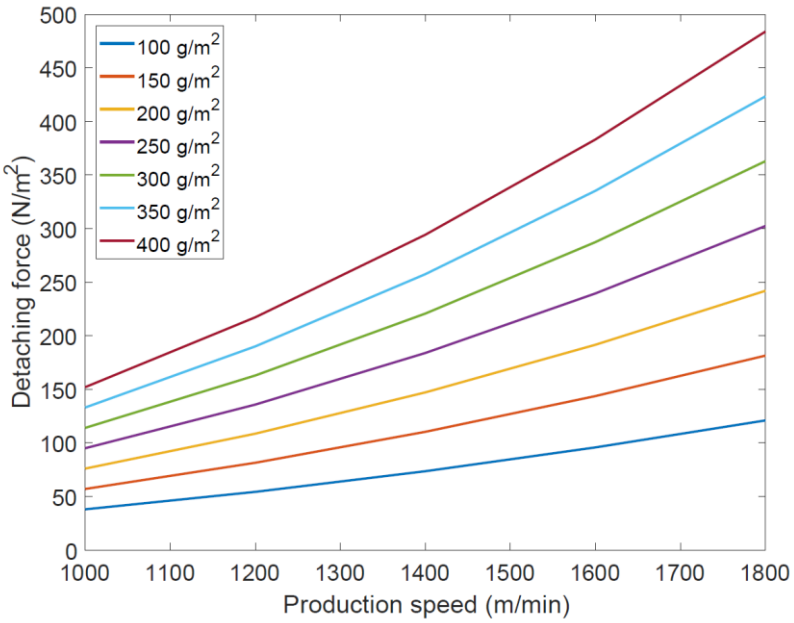

Figure 5 The detaching force at the lowest point in the rotation.

The detaching forces increase both with running speed and grammage. As seen in the figure, the slope becomes steeper with higher grammage; hence the weight is a determining factor. To stabilise these detaching forces, the support forces (tension and pressure difference) need to be adapted to the specific production state. However, it should be noted that the model merely represents the ideal case and it does not take additional detaching forces into consideration: Likewise, the internal fibre strengths are not considered in the model nor are the frictional forces between the paper and the surrounding medium (Ukkola, 1997).

Normally, however, runnability is commonly first limited by the nip regions, which also contribute to the problems in the perimeter of the cylinder. The forces in the nip regions will be discussed in the following section.

3.2.2. Detaching forces in the nip regions

The geometries of the single run drying section together with the fast-moving surfaces create local over- and under-pressures, which can cause displacement of the web and in worst case web breaks. The occurrence of local over-pressures and under-pressures for the single run concept are depicted in Figure 6.

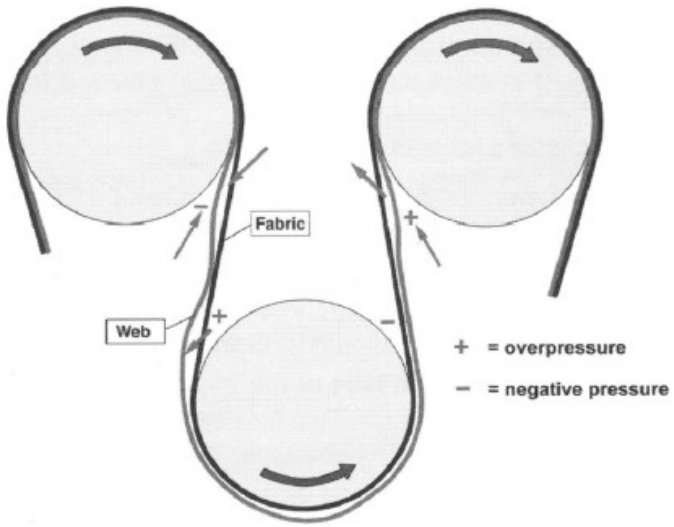

Figure 6 The pressure peaks in one cylinder position (Nurmi, 2009).

The moving surfaces will transport air, creating a boundary layer. The air transported by the boundary layer will cause a pressure force in the wedge areas. The overpressure areas are in the closing nip, where the web and fabric meet with the cylinder surface. Conversely, the under-pressure areas are where the web and fabric diverge from the cylinder.

The overpressure peak at the bottom roll, can force air to flow through the fabric and separate the web from the fabric, which will cause bagging in the nip regions, as seen in Figure 6. This may elongate the web and strain the fibres, which can affect the quality of the paper. Another side effect of elongation is the possible wrinkling of the paper, as the web approaches the following closing nip at the drying cylinder (Karlsson, 1989, p. 45). The opening nip under-pressures are harmful at the top cylinder, because the pressure can promote the formerly discussed adhesion force, which forces the paper to follow the cylinder surface. In other words the forces are directed in the same direction towards the drying cylinder.

The magnitude of the pressure is dependent on the boundary layer at the moving surface. The creation of boundary layer is, on the other hand, dependent on a variety of factors. Central factors are aerodynamic properties of the web and fabric, properties of the surrounding air and velocities of the boundary layers.

When the speed of the production line increases, the boundary layer and the caused pressure forces will increase remarkably. The production speed will affect the velocity profile at the boundary layer, which is dependent on the flow characteristics of the boundary layer. When the air is directed by the surfaces towards the nip areas, the air either gains velocity or is decelerated; this change in velocity is seen as a change in flow characteristics. The flow character of the closing and opening nip presented in Figure 7.

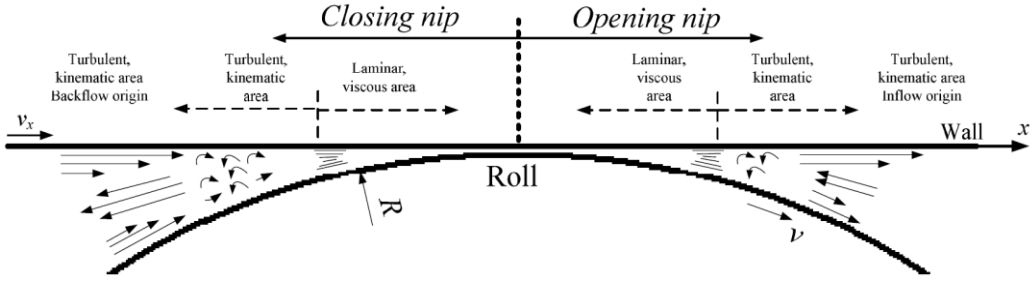

Figure 7 Closing and opening nip boundary layer development on smooth roll (Nurmi, 2009).

In the closing nip, the air is transported with high velocity by the boundary layer towards the nip. As the nip becomes narrower, the air is faced by a backflow, which will reduce the velocity of the air. The dynamic pressure will decrease, as the velocity decreases and the pressure energy is increased, which will be seen as an increase in static pressure. This intense pressure increase can cause movement of the web and fabric and the pressure force can move air through the permeable fabric, which could detach the paper web from the fabric and increase the risk of web breaks (Karlsson, 1989).

In the opening nip the phenomenon is opposite, as the roll and wall diverge, they create a boundary layer, which will transport air away from the nip area. The air will gain velocity, which will increase the dynamic pressure, which will further decrease the static pressure in the nip, creating a under-pressure. The under-pressure will induce flow towards the opening nip, as seen in Figure 7.

For the opening nip at the bottom roll, the under-pressure is considered desired, since it will act as supporting, fastening the paper tight on the fabric surface. The under-pressure becomes harmful at the opening nip of the drying cylinder, due to the enhancement of the adhesion force, which will make the web follow the cylinder instead of the fabric.

In the late 20th century the demand of production speed increase escalated, which made the phenomenon in the nip regions a factor restricting the capacity increase. Therefore, it has become increasingly important to understand of the nip effects. The difficulties in the studies of the nip effects were to determine the main variables affecting nip behaviours and the magnitude of their effects.

Karlsson (1989), he described the closing nip by combining the friction factors of the web and a bearing analogy. His work resulted in a widely used analytical equation for closing nip pressures (Karlsson, 1989, p. 25). In his reasoning, he focused on the properties of the drying fabric, raising the friction factor as one of the central components in describing the pressure in the closing nip.

$$p(\alpha_{in}) = 0.8 p_{dyn}[0.5\, ln\left(10\, \zeta \frac{L}{r}\right) - ln(\alpha_{in})] \quad (6)$$

In the equation, the dynamic pressure is $p_{dyn}=0.5\rho_{air}v^2$, α_{in} is the tangent point angle from the nip, ζ is the friction factor, L is the boundary layer development length and r

is the radius of the roll. The equation does not take viscous effects into consideration and the boundary layer flow is assumed to be decelerated when approaching the nip, which creates and impulse force resulting in the overpressure. The equation does not consider the induced backflow from the closing wedge.

The proceedings of Karlsson have been used to describe the closing nip pressure behaviour in studies and publications by Juppi (2001), Kurki (2010) and Nurmi (2009). In their studies, Juppi and Nurmi mentioned the effect of the roll radius, which is also found in the equation derived by Karlsson. The roll radius will change the angle of the closing and the opening nip and with larger roll radius the closing nip will become narrower and subsequently the air is compressed causing an increase in the pressure (Juppi, 2001) (Nurmi, 2009).

In the studies made by Nurmi the closing nip was modelled with both smooth and grooved roll with CFD (Computational Fluid Dynamics) simulations. The simulations use Navier-Stokes equations in three dimensions, to explain the flow phenomena. The equations are based on mass-, energy- and momentum balances explaining the behaviour of the boundary layer. The results from the simulations showed that the boundary layer build-up length L will not substantially affect the velocity profile, which was a factor in Karlssons results. Nurmi explained this by the effects of the backflow, which is seen in Figure 8. The backflow will disturb the boundary layer development and will also contribute to the development of static pressure in the nip (Nurmi, 2009, p. 32).

The backflow and the magnitude of the pressures in the nip are also dependent on the geometries, as in Karlssons equation the pressure is a function of the tangent point angle, meaning how narrow the nip is. In Figure 8, the different angles can be seen, as the angle becomes smaller the pressure rises.

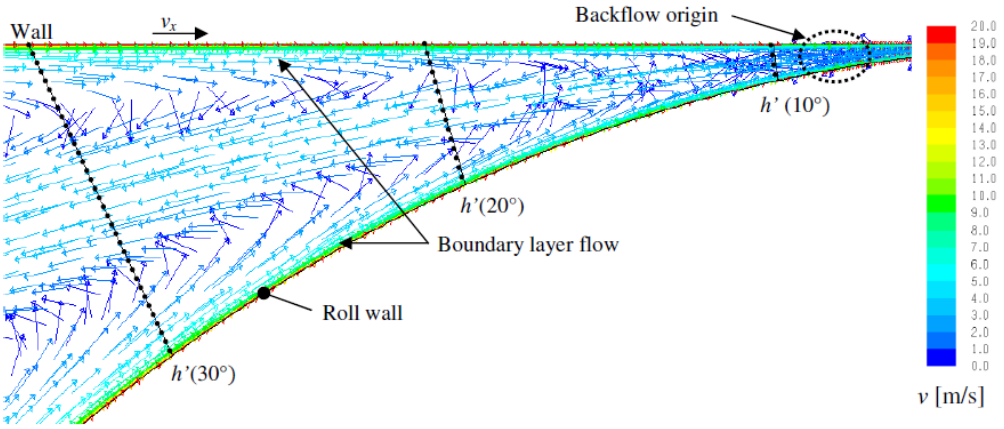

Figure 8 Closing nip velocity profile (Nurmi, 2009).

The angle is affected by the geometries of the closing nip, which is further influenced by the radius of the bottom roll. If the roll radius is increased, the incoming angle will become smaller and consequently the pressures will be higher. Of course, this requires that the rest of the geometry stays the same.

Other factors affecting the boundary layer development are the properties of the air and the fabrics aerodynamic properties. Most central air property is the viscosity, which is largely dependent on temperature. Additionally, one should remember that the viscosity of humid air is affected by the viscosities of the dry air and water vapor.

The aerodynamic properties of the fabric are, for instance, roughness of the surface and the permeability. The roughness of the surface will affect the friction factor of the fabric and further the amount of air carried from and to the nip regions. The friction factor is usually between 0.2 mm to 0.5 mm, whereas the cylinder surface can be assumed to be hydraulically smooth (Kurki, et al., 2010, p. 504).

The permeability of the fabric will also contribute in the closing nip. If air is allowed to travel through the fabric, the airflow might cause undesired detachment of the web from the fabric. When the fabric is permeable, the air will escape through the fabric when approaching the closing nip. This will lower the static pressure of the closing nip, but the escaping air might create a lift, causing the web to detach (Karlsson, 1989).

Karlssons (1989) mentions two ways to reduce the closing nip pressure effects: Changing the machine construction, so that the narrow nip regions are eliminated or

changing the aerodynamic properties of the surroundings (Karlsson, 1989, p. 49). He suggests that the friction factor could be made smaller by making the fabric smoother or alternatively by changing the characteristics of the fabric so that the pattern is in the machine direction instead of the cross direction. This will reduce the drag force on the fabric surface (Karlsson, 1989, p. 48).

The same principles apply to the opening nip at the top drying cylinder, but the aerodynamic effects are opposite. An under-pressure is created, when the fabric and the web diverge from the cylinder and the air velocity increases in the boundary layer. Considering the fabric permeability, air can flow into the under-pressurised nip through the fabric, which could detach the paper web from the fabric at the opening nip of the drying cylinder (Widlund, et al., 1997). Further as described in Section 3.1, the adhesion forces also contribute to the difficulties in the opening nip. Figure 9 illustrates the opening nip; the paper web tends to follow the cylinder for a small distance until it diverges from the cylinder. The opening nip is comprehensively studied in Leimu (2008) and by Widlund et.al. (1997).

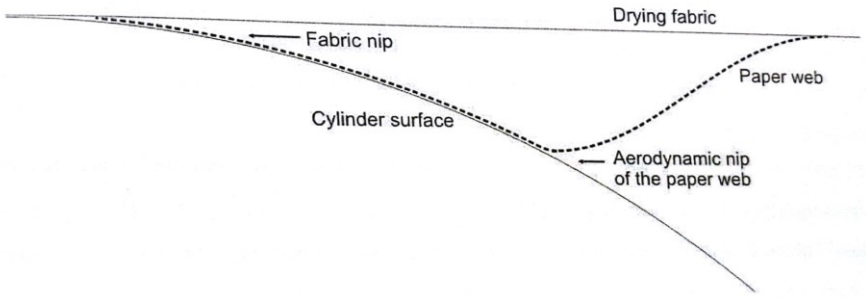

Figure 9 Fabric and paper web opening nip at the top drying cylinder (Leimu, 2008).

The point, where the web detaches from the cylinder can be controlled with web tension. By increasing the web tension, the detachment point of the web can be shifted towards the fabric nip. However, in the wet end, where the paper strength properties has not developed to the full extent, the tension cannot be allowed to be high, which is why other means have to be taken to neutralise the nip (Leimu, 2008, p. 22). Usually, a stabilising nozzle is installed at the opening nip, creating a pressure difference over the web and fabric, which will drive the paper nip toward the fabric nip.

The edge is usually the most critical area considering runnability. In addition to the issues caused by tension, paper quality or frictional forces, the aerodynamics might differ slightly in the machine cross direction. At the edges, the over- and under-pressures in the nip areas might cause flow, not only in the machine-direction, but also in the cross-direction. This flow may be considerable in narrow machines, for instance in small pilot scale machines. The cross flow can be restricted by blocking the flow, for instance with plates. However, if the paper web is not wide enough, air can flow pass the plate towards the middle of the machine cross section, which could cause undesired displacement of the web.

4. Basics in fluid mechanics

4.1. Internal flows

Internal flows are defined as flows restricted by solid boundaries, e.g. tubes, duct, pipes etc. To make a fluid move, a driving force must overcome the internal friction of the fluid and the wall friction. The wall friction is dependent on the surface properties of the boundary and the internal friction is caused by viscosity. Total viscosity is a sum of the molecular viscosity, which is a fluid property, and the "eddy" viscosity, which is dependent on the flow conditions (Zevenhoven, 2013, p. 6-18). The viscosity and wall friction will cause the driving energy (potential, kinetic, mechanic etc.) to dissipate into internal energy of the fluid, causing losses in the system. Due to the viscosity and further the no-slip condition, also the velocity profile within the system will be non-uniform. However, in practical calculations, the flow in ducts is commonly calculated as a plug flow and the velocity profile is averaged. The average velocity of the fluid flow can be calculated from the volumetric flow by dividing it with the cross-sectional area of the pipe (Zevenhoven, 2018).

$$w = \frac{\dot{V}}{A_{cs}} = < v > \tag{7}$$

Using the law of energy conversation, the general energy balance for internal fluid flows can be described as

$$\dot{m}gz_1 + \frac{1}{2}\xi_1\dot{m}w_1^2 + p_1\dot{V}_1 + P_{fan} = \dot{m}gz_2 + \frac{1}{2}\xi_2\dot{m}w_2^2 + p_2\dot{V}_2 + P_{loss} \tag{8}$$

The P_{loss} term represents the internal energy increase caused by the viscous losses and P_{fan} the mechanical power input from a fan, pump or compressor. From this equation, specific cases can be derived for e.g. ideal fluid flows, meaning isothermal and inviscid flows.

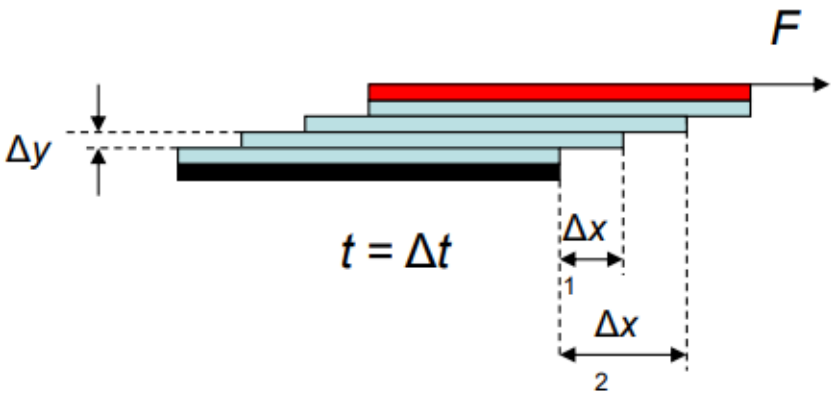

Figure 10 Principle of shear force (Zevenhoven, 2018).

The pressure loss in an internal flow can be predicted, if the shear stress can be approximated. If, as schematically depicted in Figure 10, the red plate is moving causing a force, the fluid will oppose to the change with the shear force, τ, which will work against the direction of the moving plate force vector, F. The magnitude of the shear force is dependent on the viscosity of the fluid and can be described for laminar and turbulent flow as:

$$\tau = -\eta \frac{dw_x}{dy} \qquad (9a)$$

$$\tau = -(\eta + \varepsilon) \frac{dw_x}{dy} \qquad (9b)$$

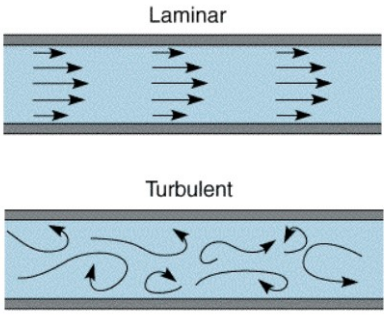

Figure 11 Laminar and turbulent flow in a pipe (Zevenhoven, 2018).

The differential term, $\frac{dw_x}{dy}$, can be seen in Figure 10 and describes the change in the velocity in the x-direction, when moving away from the moving plate. Equation (9a) for laminar flow, where the viscosity is merely the molecular viscosity, and the Eq. (9b) for turbulent flow, where the flow condition contributes to the viscosity increasing the shear force. The total viscosity for the turbulent case is approximately ten times larger than only the molecular viscosity, which will consequently cause larger pressure

losses, since part of the driving force will be dissipated to the eddy formation in the turbulent flow (Zevenhoven, 2018, p. 1-27).

Laminar and turbulent flows are characterised with the Reynolds number. The Reynolds number is the ratio between inertial and viscous forces and is dependent on the dynamic viscosity, the velocity and the dimensions of the channel (Zevenhoven, 2013, p. 6-12):

$$Re = \frac{\rho w D_h}{\mu} \tag{10}$$

For pipe flow, the flow is laminar, if the Reynolds number is below 2100 and turbulent, if the number is over 4000. The gap between the two represents a transition behaviour, which is complicated and hard to model (Zevenhoven, 2013, p. 6-25). The limits between turbulent and laminar change with the surroundings, for instance for a flow on a flat surface the transition from laminar to turbulent occurs when Re ≈ 500 000 (Zevenhoven, 2013, p. 6-12).

Because it is difficult to express the total shear force for the turbulent flow, a practical approach to the problem is to relate the shear force at the wall, τ_w, to the kinetic energy of the fluid, by including an empirical friction coefficient, ζ (Zevenhoven, 2013, pp. 6-21).

$$\tau_w = \zeta \frac{\rho w^2}{2} \tag{11}$$

Here the velocity *w* is the average velocity over the pipe cross-section and as earlier mentioned. The shear force can describe the pressure loss over a section in an internal flow, which, as pipe dimensions are included, can be expressed (Zevenhoven, 2013 p.6-21).

$$(p_1 - p_2) = \Delta p = \tau_w L \frac{S}{A_{cs}} = \zeta \frac{\rho w^2}{2} L \frac{S}{A_{cs}} \tag{12}$$

The dimensional analysis in Zevenhoven, 2013, p. 6-21 shows that the friction coefficient is clearly a function of the Reynolds number. The friction coefficient is also dependent on the pipe dimensions and the surface roughness and especially the ratio between the diameter and the roughness (Zevenhoven, 2013, p. 6-21).

To determine the friction coefficient, the Moody chart can be used, the chart relates the friction coefficient, Reynolds number and the relative surface roughness. The

Moody chart can be approximated for turbulent flows using the approximation (Zevenhoven, 2013, p. 6-25):

$$\zeta = \frac{0{,}25}{\left(log_{10}(\frac{\bar{x}}{3.7D_h}+\frac{5{,}74}{Re^{0{,}9}})\right)^2} \quad (13)$$

where, $5000 \leq Re \leq 10^8$ and $10^{-6} \leq \frac{\bar{x}}{D_h} \leq 10^{-2}$

The hydraulic diameter, D_h, of the channel will change with the channel geometries. For circular cross-section, the hydraulic diameter is the same as the real diameter, but for other channel shapes the hydraulic diameter.

$$D_h = \frac{4A_{cs}}{S} \quad (14)$$

where A_{cs} is the cross- section area and S is the circumference These equations base on the energy balance and one issue with the equation is that it does not include the important no-slip condition. The no-slip condition states that the velocity of the fluid at the boundary surface is the same as the velocity of the boundary surface. To model the motion of the fluid, Navier-Stokes equations are used and form the foundation for Computational Fluid Dynamics (CFD).

Since water is evaporated in the drying section, the air in the drying hood will be a mixture of dry air and water vapor. This will influence the fluid properties, e.g. viscosity. The viscosity of a humid air is calculated as a mixture of gases as (Tsilingiris, 2008):

$$\mu_m = \frac{(1-x_v)\cdot\mu_a}{(1-x_v)+x_v\cdot\Phi_{av}} + \frac{x_v\cdot\mu_v}{x_v+(1-x_v)\cdot\Phi_{va}} \quad (15)$$

where the viscosity of the mixture is dependent on the molar fraction of water vapor in the mixture x_v , the viscosity of the components and their interaction parameters.

$$\Phi_{av} = \frac{\sqrt{2}}{4}\cdot\left(1+\frac{M_a}{M_v}\right)^{-\frac{1}{2}}\cdot\left[1+\left(\frac{\mu_a}{\mu_v}\right)^{\frac{1}{2}}\cdot\left(\frac{M_v}{M_a}\right)^{\frac{1}{4}}\right]^2 \quad (16)$$

$$\Phi_{va} = \frac{\sqrt{2}}{4}\cdot\left(1+\frac{M_v}{M_a}\right)^{-\frac{1}{2}}\cdot\left[1+\left(\frac{\mu_v}{\mu_a}\right)^{\frac{1}{2}}\cdot\left(\frac{M_a}{M_v}\right)^{\frac{1}{4}}\right]^2 \quad (17)$$

Which are dependent on the molecular mass of the components in the mixture (Tsilingiris, 2008).

5. Web handling for single run constructions

Development on web handling has mainly been based on empirical knowledge and practical experience. The first studies in the field were made in 1980s by Thomas and Wahren (Hauser, 1991).

A rule of thumb in web handling is that the forces straining the material should equal the supporting forces working against the straining forces (Kurki, et al., 2010, p. 488). As most of the harmful forces increase with a machine speed increase, also the support force must be increased to disperse the harmful side effects of the forces. Usually, this requires some actions to stabilise the web, among these actions are investment on runnability equipment, which provide the needed support force.

5.1. Bottom cylinders for runnability purposes

As the single-run concept became more productive compared to the double-run concept, the evaporation efficiency from the bottom roll decreased, since the fabric acts as a heat resistance between the cylinder and paper web. This led to the development that the steam supply to the bottom roll was throttled, which against expectation did not lower substantially the evaporation capacity (Hauser, 1991).

Since the bottom cylinder was not used for evaporation, the bottom roll could be modified to optimise the runnability. The modifications can be surface structures, e.g. grooves, to neutralise the nip regions, or the cylinder can be perforated and air evacuated from the cylinder to stabilise the web. Figure 12 shows, the grooved roll is shown on the left and the smooth bottom roll on the right. As described in Section 3.2.2 the nip areas build up pressure peaks in the smooth roll and with increased speed the pressure forces might become so high that the web detaches from the fabric and the risk for web break increase.

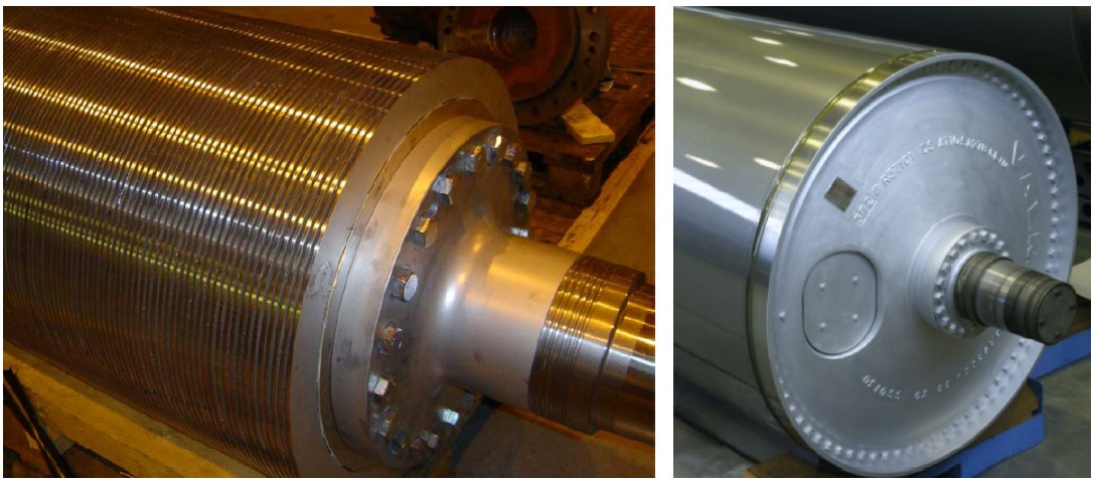

Figure 12 Left: Grooved roll. Right: Smooth bottom roll (Nurmi, 2009)

5.1.1. The grooved roll

As the passive cylinders are not needed for evaporation they can be modified and different surface structures can be made on the cylinder surface, which facilitate pressure equalisation between the opening and the closing nips. The pressure is equalised by allowing air to flow from the closing nip to the opening nip through the grooves.

Studies and academic papers on the grooved roll concepts are fairly limited. However, the doctoral thesis by Nurmi (2009), simulated closing nip of smooth and grooved rolls. Factors affecting the functionality of the grooved roll are, for instance, the diameter of the roll or wrap angle, the depth of the groove and the groove fraction. The radius of the roll or of wrap angle will affect the closing nip pressures, but in addition, the roll wrap angle will affect the frictional losses in the groove and at the fabric wall causing a pressure gradient along the length of the groove. Consequently, increasing the wrap angle will increase the pressure loss between the closing and opening nip. Pipe analogy can be used to describe the behaviour in the groove. Therefore, the frictional losses in the groove can be analytically expressed by:

$$\frac{dp}{ds} = \frac{\zeta}{D_h}\frac{\rho_a v_{rel}^2}{2} \qquad (18)$$

Here $\frac{dp}{ds}$ represents the difference in pressure in the groove tangential coordinate, s. The pressure difference is described by the density of the air, ρ_a, relative velocity, v_{rel}, which is the velocity difference between the air and the velocity of the wall and groove and D_h, is the hydraulic diameter of the groove. The hydraulic diameter varies with the shape of the groove. For the equation, assumptions of infinitively long and straight pipes are made and the surfaces are assumed hydraulically smooth (Nurmi, 2009, p. 43).

However, the pipe analogy is challenged, not only by the roughness of real dryer fabrics, but also by the permeability of the web. When the permeability of the web is increased, the air flows through the fabric disturbing the flow of the air to the groove. The air velocities for the nip regions are compared for an impermeable wall and a permeable fabric in Figure 13a) and b). The figure illustrates that the velocities in the closing nip tangent point are higher for the impermeable wall condition compared to the fabric condition. In the fabric condition, the air will flow through the fabric due to the large pressure difference over the fabric when approaching the closing nip. This will lower the pressures in the closing nip. However, in the groove, the pressure is lower compared to the ambient pressure, due to the influence of the under-pressure of the opening nip. For the permeable fabric condition, air will flow into the groove due to the pressure difference, transporting more air with the groove compared with the wall condition (Nurmi, 2009, p. 69).

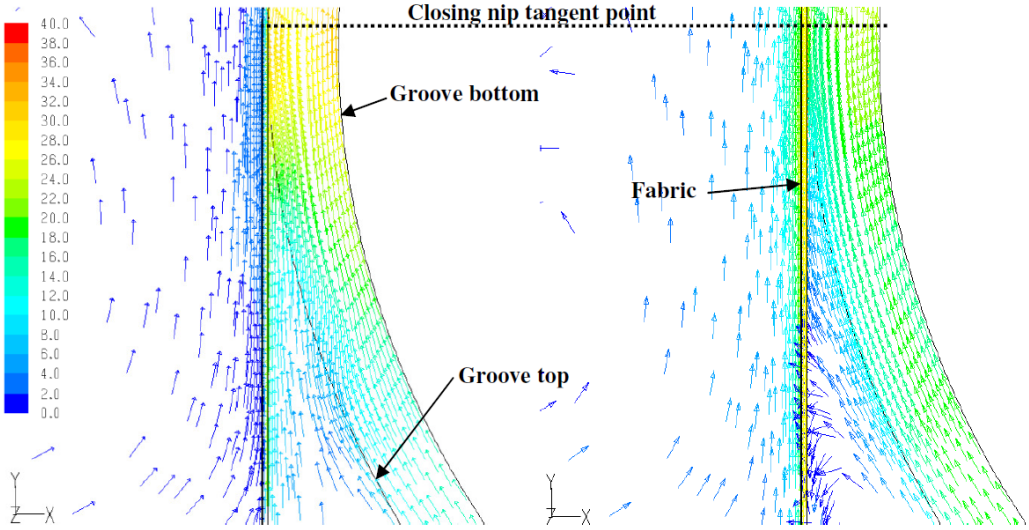

Figure 13 a) Closing nip with impermeable fabric or wall Figure 13 b) closing nip with permeable fabric (Nurmi, 2009)

To understand the effects of a permeable web and the groove behaviour in general, a simple simulation model was developed. The model is illustrated in Figure 14 and the model is presented in Appendix A. In the model the pipe analogy is made and for the pressure loss in the groove, so Eq. (18) is used. The model utilises the equations in Section 4, to express the pressure, velocity and mass flow profiles along the groove. The model solves a set of nonlinear equations, using a nonlinear equations system solver. The model can however only be used as a qualitative tool, since it does not utilise the Navier-Stokes equations and therefore, does not describe momentum balances or take viscous losses into account.

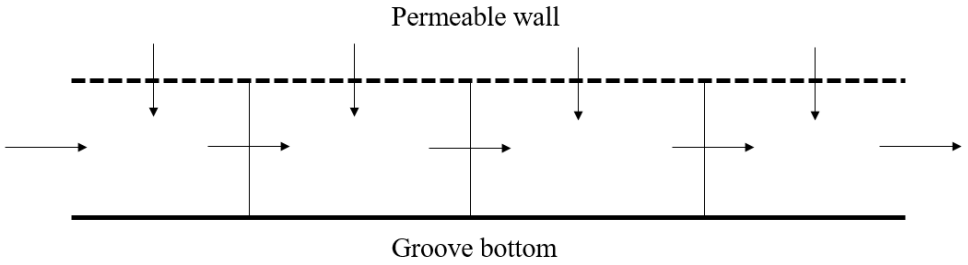

Figure 14 Illustration of the simple groove model.

The input variables in the model are:

- Inlet pressure (Pa)
- Outlet pressure (Pa)
- Ambient pressure (Pa)
- Air properties
    - Kinematic viscosity (m^2/s)
    - Density (kg/m^3)
- Groove geometries; width, depth and length of the groove
- Permeability of the wall (m^3/m^2h)

The inlet and outlet pressures are pinned, because the outlet pressure tends to be the same in the experiments, even though the inlet pressure varied.

The permeability of the web was modelled using an empiric formula based on the pressure difference and the permeability, K, of the fabric as follows:

$$\frac{\dot{V}}{A} = K\left(\frac{\Delta p}{100\ Pa}\right)^{n} \tag{19}$$

The empirical factor in the exponent is dependent on the ambient temperature and for 20 °C we have n = 0,7 (Muhonen, 2018). Figure 17 presents the result of one simulation with the model. The inlet pressure set is above the ambient pressure to simulate the over-pressure created by the closing nip. In the simulation the velocity of the groove and wall was 1200 m/min.

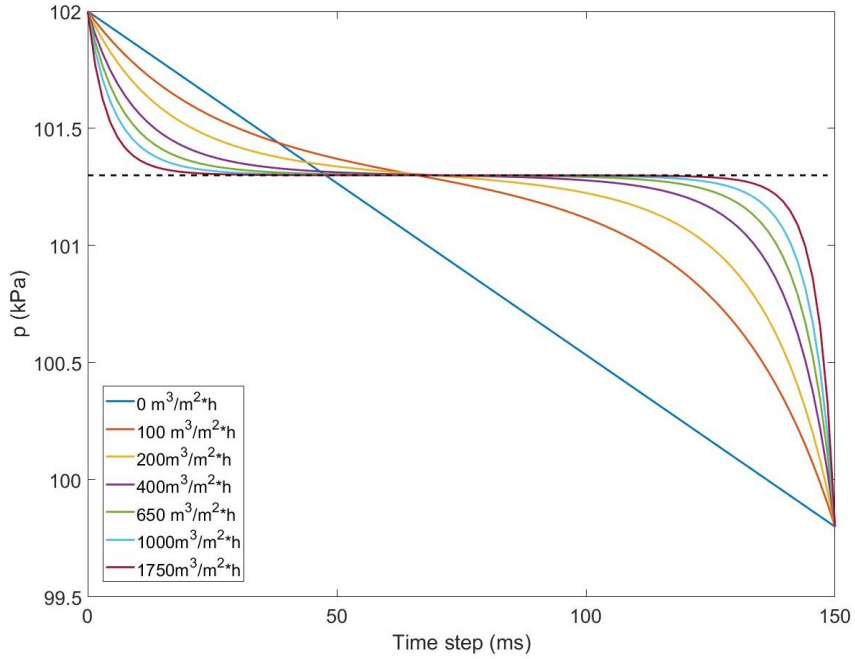

Figure 15 Pressure profile over the pipe for inlet pressure 102 kPa.

When the permeability is low or zero, the model follows perfectly the pipe analogy and gives a linearly varying pressure between the inlet and outlet. As the permeability is increased, the air flow is affected by the leaking air and the pressure profile becomes curved. Interesting enough, for higher permeability the pressure reaches the ambient pressure faster compared to the case with an impermeable wall. This effect could be explained by the mass flow profile reported in Figure 16. The solid lines represent the mass flow along the groove as the dashed red lines represent the leakage either in or out from the permeable wall.

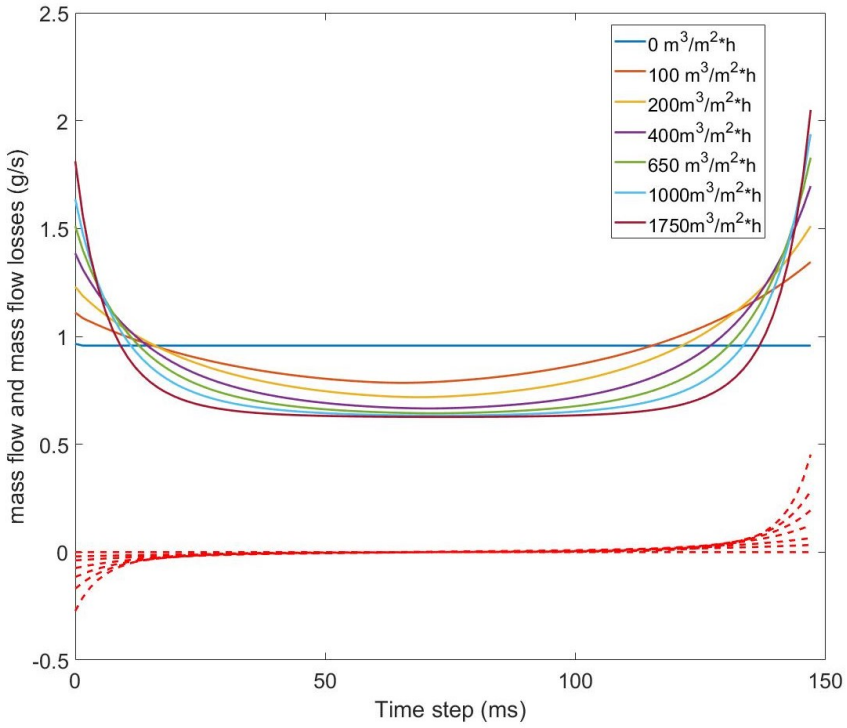

Figure 16 Mass flow profile with inlet pressure 102 kPa.

When the permeability is low or zero the mass flow stays constant, but when the permeability is increased the air will flow from the surroundings into the groove transporting more air, required that the groove is below ambient pressure. When the ambient pressure is reached the airflow stays constant and starts to increase again when the outlet is approached. Additionally, due to the lower pressure at the outlet, air flows through permeable wall increasing the volumetric flow.

The over-pressure in the inlet is undesired, so in the following simulation it is assumed that the closing nip over-pressure is neutralised by stabilising equipment and the inlet pressure is lower than the ambient pressure and the outlet pressure is lower than the inlet. The pressure profile illustrated in Figure 17 and the groove velocity is 1200 m/min.

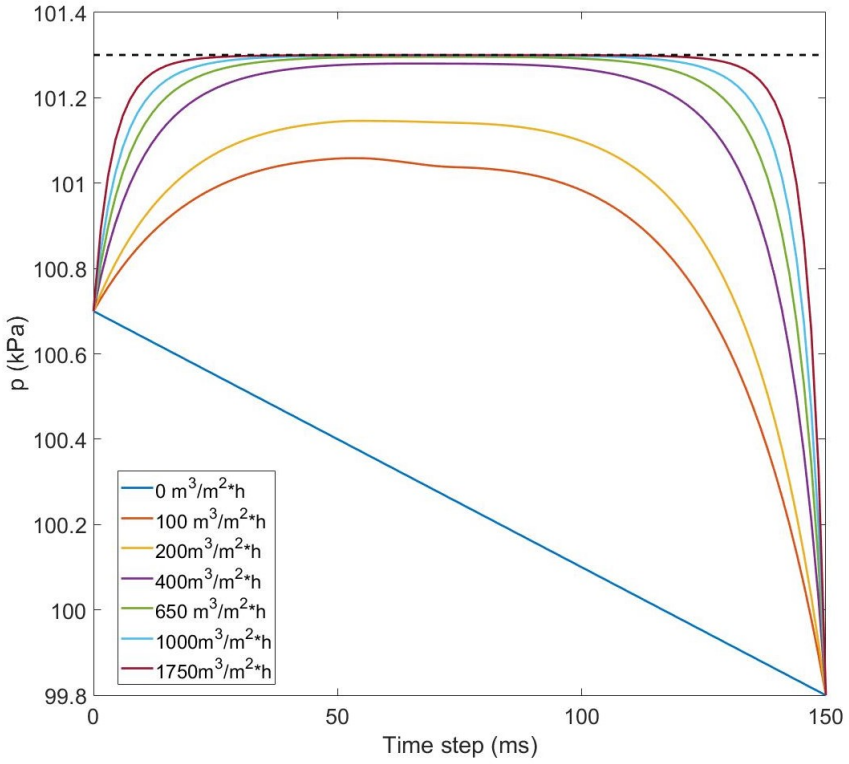

Figure 17 Pressure profile over the groove with the groove velocity of 1200 m/min.

With increased permeability, the pressure approaches the ambient pressure, due to communication with the surroundings. The mass flow profile for the same situation can be seen in Figure 18. When the permeability is zero, the mass flow is constant and does not vary over the groove, so air can neither leak in nor out of the groove. However, when the permeability is higher the mass flow is different compared to the impermeable case.

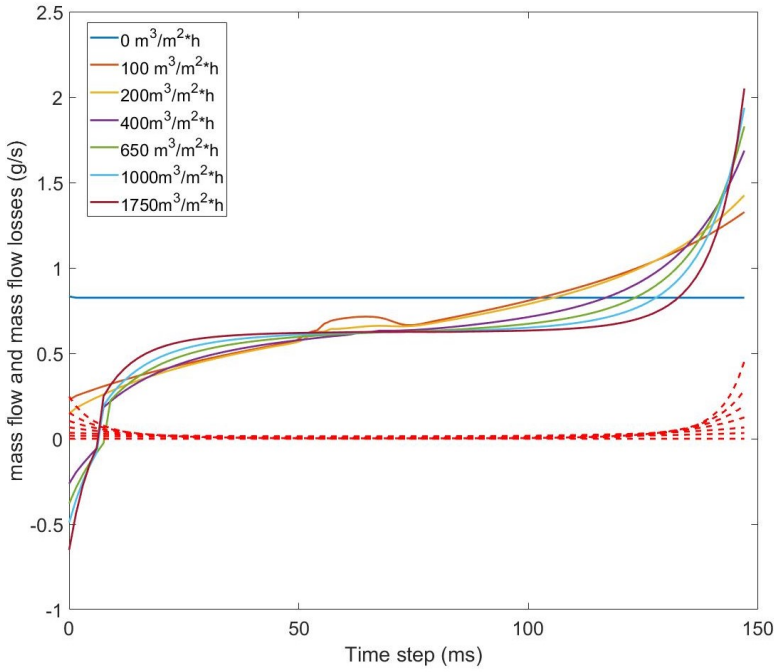

Figure 18 Mass flow profile for one simulation, groove velocity 1200 m/min.

With higher permeability, the profile becomes more curved. The mass flow is negative at the inlet, which indicates that the air is flowing out of the pipe at the inlet and when the pressure in the pipe approaches the ambient pressure, the mass flow over the tube will stabilise. Reaching the outlet, the mass flow out of the tube becomes higher, due to the difference between the ambient pressure and the outlet pressure. The red dashed lines in Figure 18 denote the mass flow rate directed into the groove from the fabric, due to the permeability. At the inlet, air flows into the groove, due to the pressure difference and the flow into the groove ceases when the pressure increases to then again increase when approaching the outlet.

From a modelling point-of-view, the flow conditions within the system are interesting. Whether the flow is laminar or turbulent is important, since it will indicate how to model the system. The Reynolds number is drawn in Figure 19. Looking at the magnitude, the flow seems to vary between laminar and turbulent, which would suggest that the flow is in the transitions zone, which is computationally hard to define.

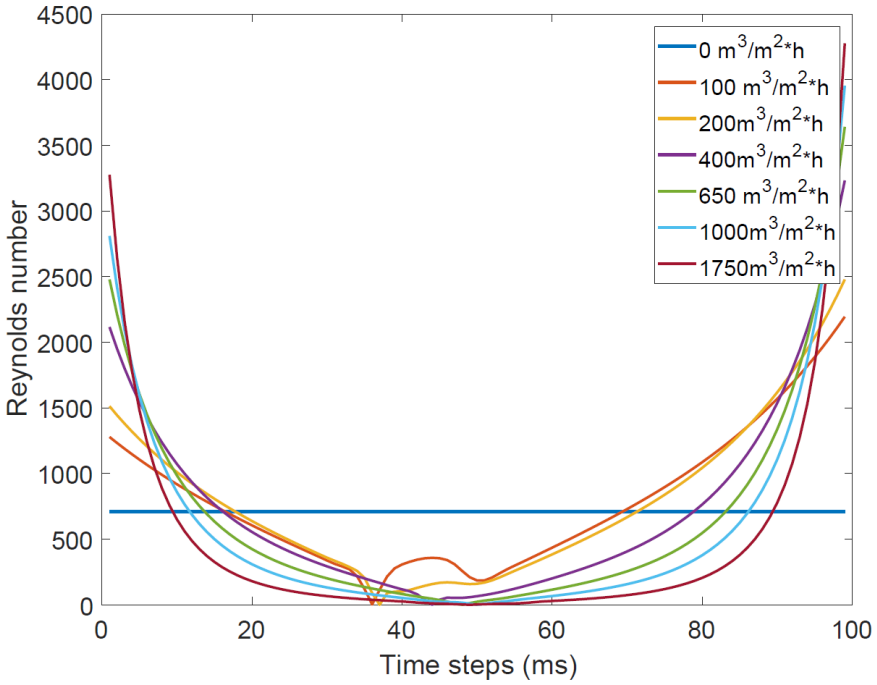

Figure 19 Reynolds number over the simulation time with the groove velocity of 1200 m/min.

In Figure 18 and in Figure 19 some instabilities in the curves can be seen, due to inaccuracies in the model and the algorithm is unable to solve the equations for two of the permeabilities.

By increasing the velocity of the wall, the results will not significantly change, since the pressures are fixed. However, in the real case, higher velocities will lead to increased over- and under-pressures. When the speed is increased only the air velocity in the pipe will increase and consequently the mass flow will increase. In the simulation results shown in Figure 20, the machine speed was increased to 2000 m/min and compared with the results of Figure 18 the mass flow has increased by approximately 50 %.

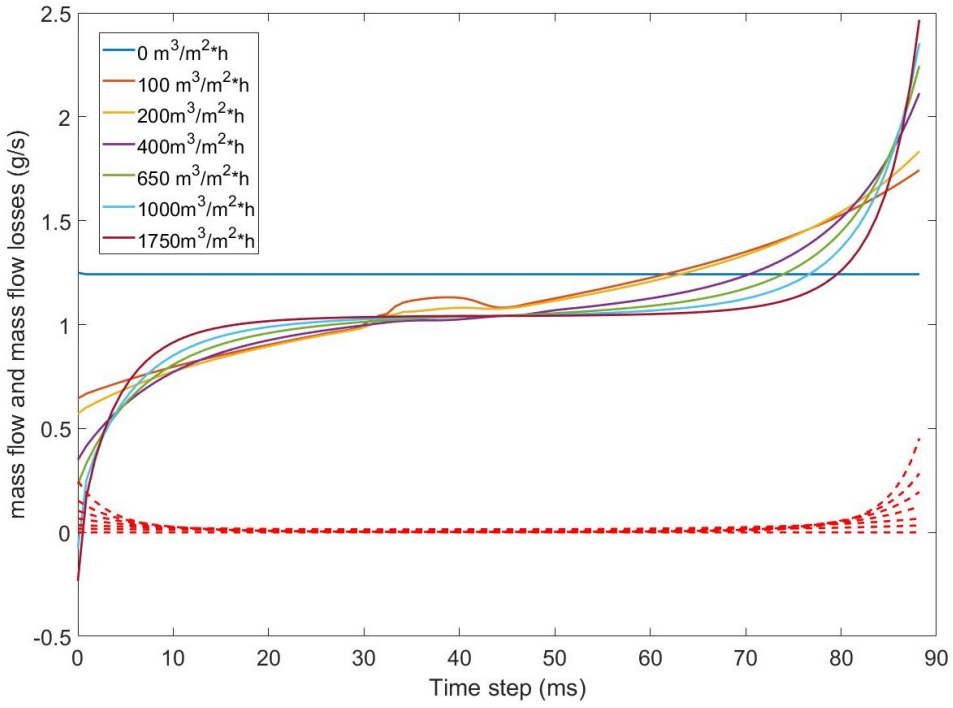

Figure 20 Mass flow of simulation with 2000 m/min machine speed.

If the leakage mass flows are inspected, the mass flow in the groove is seen not to increase as the velocity is increased, so the leakage stays constant. This is explained by the pressures; since the pressure difference, which is the driving force for the leakage mass flow, stays the same.

Permeability of the web is not the only determining factor for the pressures in the nip areas and the pressures over the cylinder surface. Also, groove geometry and wrap angle will affect the pressures. The wrap angle affects the pressure losses in the groove; the shorter the groove is, the smaller the losses. Since the outgoing pressures are fixed in the model, this cannot be seen in Figure 21a and b. However, the effect of the permeability and other losses can be seen the figure. In Figure 21a, the simulation length is 500 milliseconds compared to the earlier simulation of 150 milliseconds and in Figure 21b the simulation length is only 25 milliseconds.

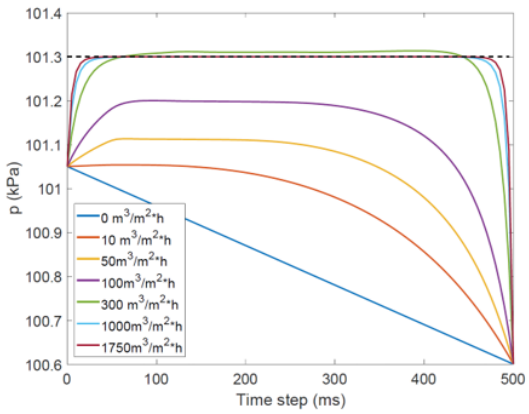

Figure 21a Longer groove.

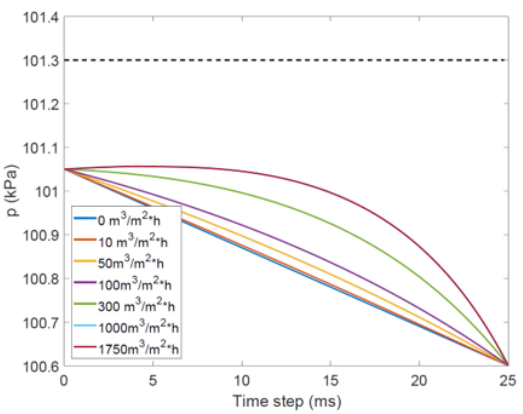

Figure 21b Shorter groove.

From the figure, one can see that the permeability is less significant when the groove is shorter. The pressure in the groove does not reach ambient pressure, because of the driving force from the opening nip. The radius of the roll will also affect the paper, since smaller ratio will cause length differences in the thickness, which strains the fibres. Hence, a larger diameter is beneficial from this point-of-view (Pitkäniemi, 2000, p. 61).

Larger grooves will allow a larger volume flow of air through the groove, which will further decrease the large overpressure peaks in the nip areas, since the velocity of the air must not decrease as much at the converging nip. In the groove simulation model in Nurmi (2009), the cylinder area was described as fraction between the grooves and the area between the grooves, defined in his work as roll land area. Nurmi (2009) defines the ratio between groove and roll land as groove fraction (Nurmi, 2009, p. 45):

$$G_f = \frac{A_{GR}}{A_{GR}+A_{RL}} \qquad (20)$$

The groove fraction is the ratio between the groove area and the total projected area. The effect of the groove fraction and the width of the groove bottom and roll land can be seen in Figure 22 (Nurmi, 2009, p. 43). In the simulation to the left, the groove width is three times larger than the roll land width, whereas on the right the roll land is three times larger than the groove bottom.

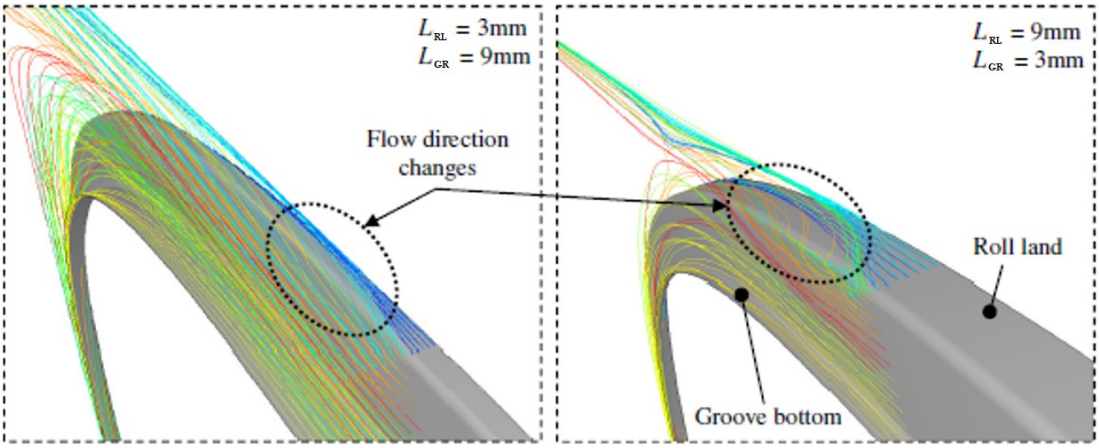

Figure 22 The flow direction change compared with different groove and roll land widths (Nurmi, 2009).

When the roll land is substantially larger than the groove floor, the air on the roll land has to alter its flow direction a lot more compared to the case with a narrower roll land. This leads to a decrease in the kinetic energy and, according the law of energy conversion, the kinetic energy will be transformed to internal energy cause minor losses in pressure. In addition to the energy balance, the momentum balance is affected by the change of flow direction (Nurmi, 2009, p. 43).

5.1.2. Suction roll

As the machine speed increases, the boundary layer flow increases, so that the web cannot be stabilised only by the grooved roll. The company Beloit introduced in 1985 suction rolls as bottom rolls to enhance web handling (Juppi, 2001, p. 13). The concept is based on axial suction of the roll creating a under-pressure at the perimeter of cylinder. The diameter in the rolls varies from small diameter rolls of 800 mm to large diameter rolls of 1500 mm and 1850 mm. According to Juppi, with increased cylinder diameter, it becomes more difficult to create an under-pressure in the closing wedge. It is partly because the geometries are changed, which cause the angle of the wedge to decrease, leading to a narrower wedge, and partly because the suction area is increased, which requires larger evacuation out from the cylinder (Juppi, 2001). The suction roll is still the most commonly used runnability concept, especially in the wet end of the

machine, where the paper web is wet and low web tension is desired. The suction ensures good runnability, as it creates a pressure difference over the web and fabric, which secures that the web attaches to the cylinder over the whole rotation. The suction rolls can be grooved with holes on the bottom of the groove and on the roll land, or only perforated rolls. Application of suction rolls is proven to decrease shrinkage, enable tail threading without ropes and the suction will be beneficial for the edge area of the paper, where runnability problems more regularly occur, by securing it to the cylinder surface (Juppi, 2001).

As the edge area is the most sensitive one with respect to the runnability, the suction roll could be optimised to support only the critical areas of the paper. Juppi studied a vacuum roll that was divided into separate chambers and he concluded that the efficiency of the suction roll is largely dependent on the vacuum level in the chambers. It appears that at running speeds of 1800 m/min an under-pressure of 2000 Pa in the chambers is sufficient to enable smooth runnability (Juppi, 2001, p. 112).

The model used to describe the air behaviour for the grooved cylinder was altered for the suction roll case, according to the illustration in Figure 23. Additional variables were introduced, expressing the pressure inside the cylinder and the geometries and pressure losses over the holes. The values for the pressure inside the mantle were taken from the work of Kauppinen and Juppi (Juppi, 2001) (Kauppinen, 2018).

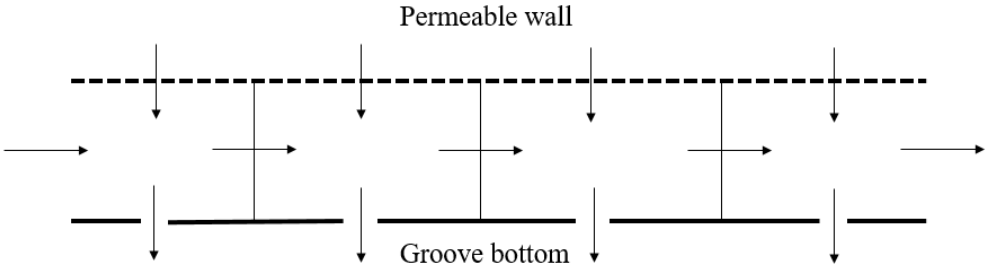

Figure 23 Illustration of the simple suction roll model.

In Figure 24, the pressure profile for a simulation with the suction roll model is presented. The inlet pressure is higher than the ambient pressure, whereas the outlet pressure is lower. This would also be the situation at the closing and opening nip. The permeabilities are the same as for the grooved roll.

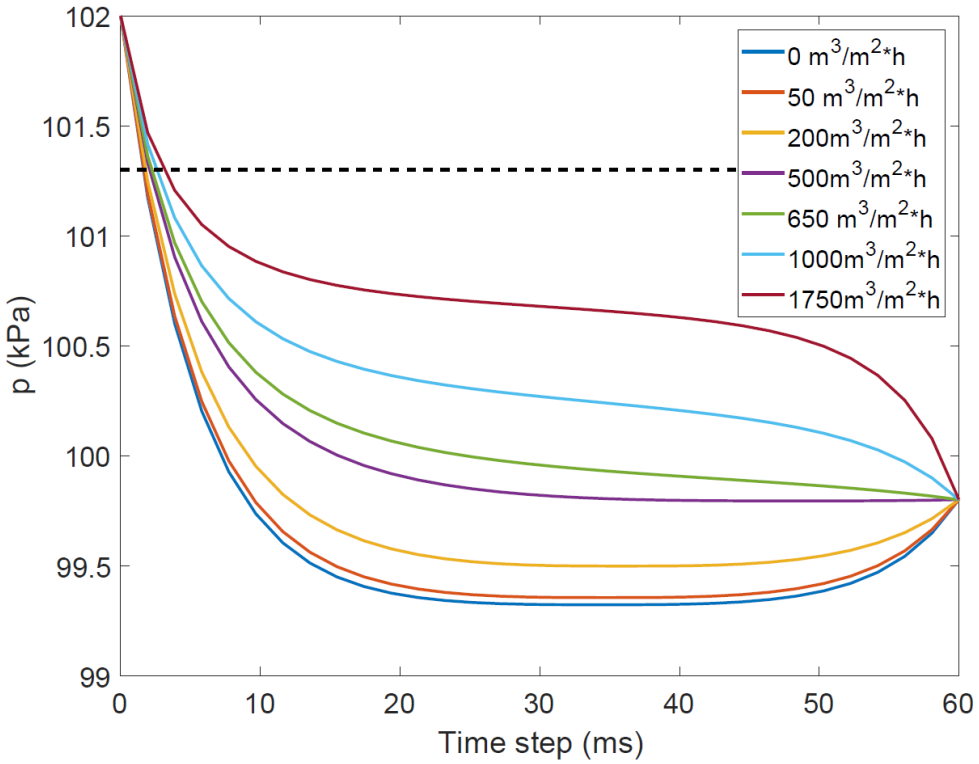

Figure 24 The pressure profile over the simulation time with 1200 m/min as the running speed.

After the inlet, the pressure is brought seemingly fast to the ambient pressure, because of both the permeable wall and the holes in the bottom of the groove. However, for a more permeable wall, the effects of the pressure difference over the holes are less pronounced than for the case with an impermeable wall. This is due to the ambient pressure affecting the under-pressure built inside the groove. The situation is better understood by inspecting the mass flow profile in Figure 25.

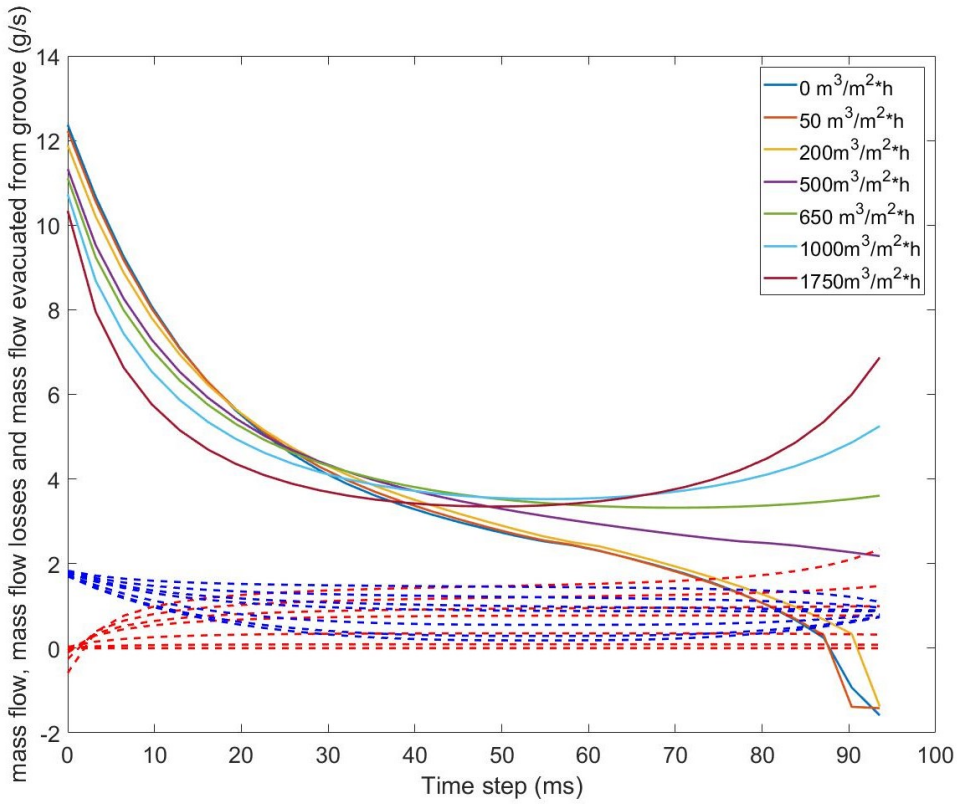

Figure 25 The mass flow profile for the suction roll simulation

At the inlet, the mass flow in the groove is at its highest, the mass flow starts decreasing slowly due to the mass flow into the cylinder through the holes, drawn in the figure as the blue dashed lines. The mass flow into the cylinder stabilises, as the pressure difference decreases and when the outlet is approached, the mass flow continues decreasing, due to the suction, for the case of an impermeable wall. However, the mass flow will increase for the case with the permeable wall, due to the communication with the ambient atmosphere (drawn as the red dashed line). Air will be sucked through the permeable wall and further through the holes and into the cylinder, so the mass flows through the wall and the holes are highest for the permeable wall.

On the other hand, if the inlet pressure is below the ambient pressure, the pressure profile will get the appearance depicted, in Figure 26.

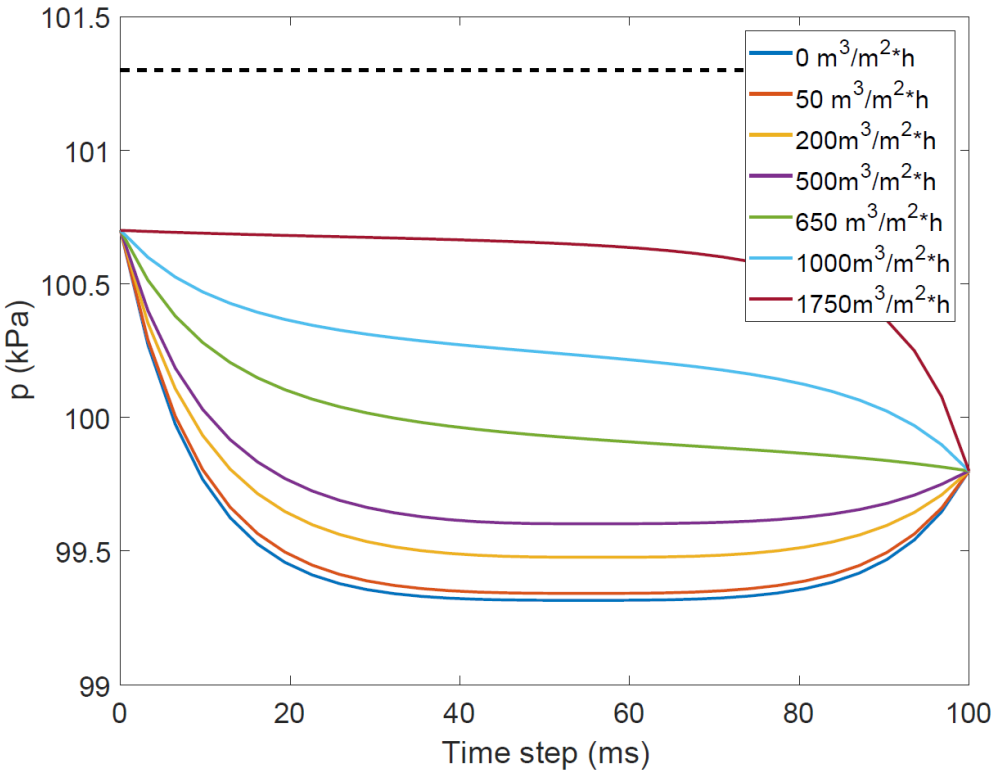

Figure 26 Pressure profile for suction roll simulation with lower pressure

In the simulation, the inlet pressure is lower than the ambient pressure and the other pressures remain the same as earlier. As seen from the figure for an impermeable wall, the pressure reaches the pressure in the cylinder, whereas for the permeable web, the air will be sucked from the ambient air through the groove and into the cylinder, which leads to higher pressures compared with the impermeable case. The mass flow in the groove and out of the groove can be seen in Figure 27.

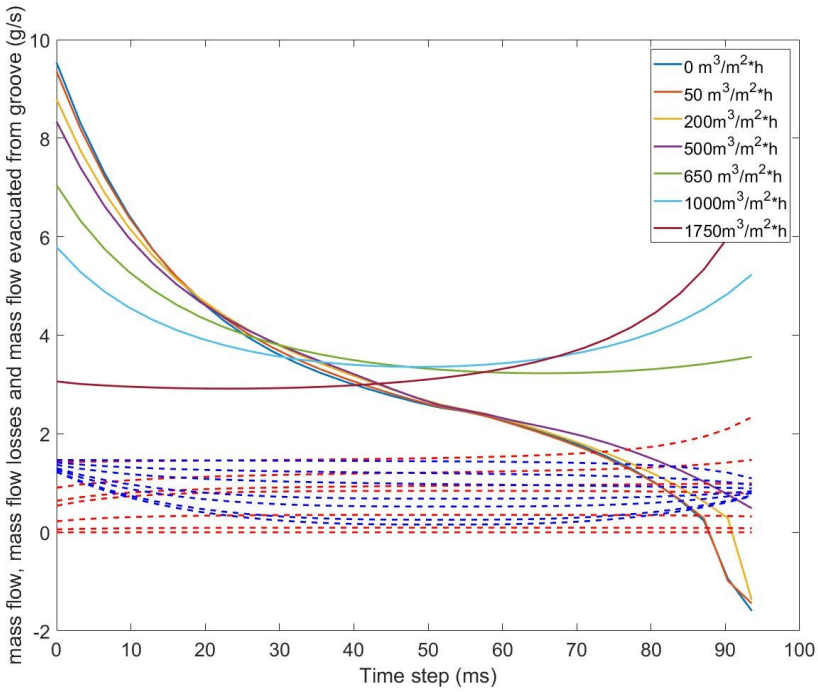

Figure 27 The mass flow in the groove and out from the groove for the suction roll simulation.

Compared to the earlier simulation the mass flow rate is lower for the lower inlet pressure, which is due to the two driving forces, in other words the ambient and suction pressure differences. For zero permeability, the mass flow has only slightly decreased, due to the decrease in the driving force. However, for the highest permeability, the mass flow stays rather constant for a longer time, due to the communication between the cylinder middle and the ambient surroundings.

For the suction roll model, the velocity effects are the same as for the grooved roll case. The pressure will not change only by increasing the velocity, since in the real systems the inlet and outlet pressures will change as the nip effects become more dominating. Only by increasing the velocity, the mass flow rate and air velocity will increase, implying that more air is transported in the groove. However, the leakage and evacuated air will stay the same, since the driving forces stay the same.

The pressure in the groove is also dependent on the size and distribution of the holes. In the model, when the diameter of the hole is increased, the pressures will be lower and the mass flow through the holes increase. Also, the pressure resistance of the hole will affect the mass flow through the hole. The pressure resistance is dependent on the

shape of the hole, whether the edges are smooth or sharp etc. In his Master's Thesis, Kauppinen (2018) studied the effect of different drilling patterns and hole shapes on the functionality of the suction roll (Kauppinen, 2018). The motivation to study this was a clogging of the suction rolls; when the suction rolls are run for a long period, the holes on the cylinder surface tend to clog by dirt and fibres. Clogging occurs when dust is sucked into the cylinder. However, when the suction force does not overcome the centrifugal force, the dust particles stay in the cylinder and accumulate in the inner wall of the cylinder, clogging the holes (Kauppinen, 2018, p. 34).

This tendency is stronger for paper grades using recycled fibres, since the dust formation is higher for these grades. Additionally, according to Kauppinen, the clogging occurs more frequently in the beginning of the drying section, since more fibres and dust come off the paper in this section (Kauppinen, 2018, p. 34). This is a significant issue, since the paper specifically needs most support in the beginning of the drying section. The support in the beginning of the drying section is especially important when using recycled fibres, as the fibres have lost some of their strength, due to the processing. Therefore, the support will restrict the amount of recycled fibres used, compared to virgin fibres, which might lead to additional costs. The decrease in support due to clogging, may increase the number of web breaks and complicate the tail threading. Furthermore, the holes must be cleaned, which requires service breaks. The increase in web breaks and service breaks will consequently affect the production rate.

5.2. Stabilisers

Originally the suction roll was designed to operate without any additional stabilising, but by introducing stabilisers, the systems could be run at higher speeds (Kurki, et al., 2010, p. 512). The stabilisers can be active or passive. Active stabilisers operate by suction or by blowing to create an under-pressure in the desired area. Passive stabilisers isolate the pocket to create a restricted area, where the suction roll can create a lower pressure. The stabiliser is usually equipped with mechanical seals, which are directed against the fabric or the cylinders. The objective of the mechanical seals is to

break the boundary layers created by the moving surfaces and to restrict the high-pressure areas.

The active stabilisers or blow and suction boxes utilise mechanical seals to restrict the area of influence. Normally the need for mechanical seals is higher with suction boxes compared to blow boxes. The use of mechanical seals will lower the fan power consumption, since the blowing or the suction is directed to the specific area to be stabilised.

The drawback of mechanical seals is the attrition of the seals, due to contact with the fabric, which is induced by fabric bending. Fabric bending is caused by inconsistent fabric tension and the bending phenomenon increases with the age of the fabric. The extent of bending depends on the running speed, fabric tension and the pressure difference over the web. The fabric tension is rarely uniform through the machine cross section and the non-uniformity causes the fabric to bend more at the edges compared to the middle area, which makes the seals wear off more at the edges than at the middle area. Solving this problem by moving the seals away from the fabric surface might not be the appropriate solution, since the increased flow area will cause unnecessary increases in the fan power consumption and the seals partly lose their functionality (Leimu, 2017).

The stabilisers, based on blowing, create a low-pressure zone by an ejector and air jet blown along a rounded surface, which causes the air to follow the rounded surface. The function principle of blow boxes is shown in Figure 28. The air is ejected through the nozzles (red arrows), where the ejected air spontaneously follows the curved area. This is called the Coanda phenomenon (Leimu, 2008, p. 52).

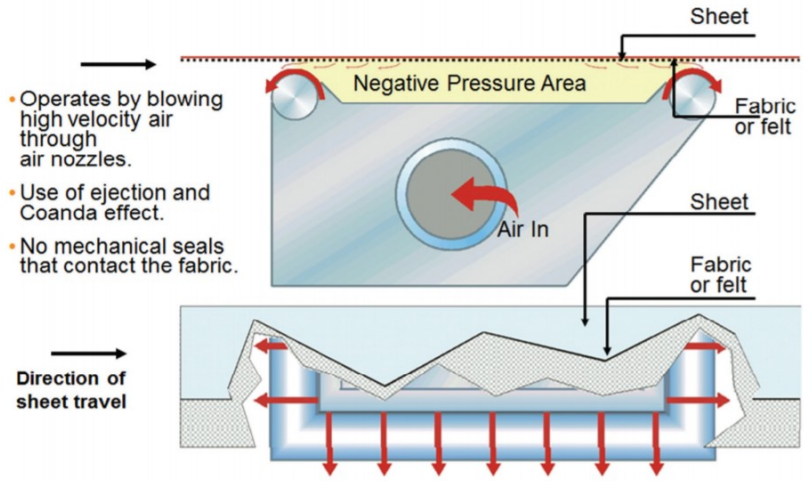

Figure 28 Function principle of stabilisers based on blowing (Valmet Technologies Inc., 2012)

According to the studies made by Neuendorf and Wygnanski (1999), the air jet can follow the rounded surface up to 180-270 degrees (Neuendorf & Wygnanski, 1999). In runnability systems this angle is commonly less than 100 degrees (Leimu, 2008, p. 52). The advantage of blow boxes utilising air jets and ejectors is the low maintenance requirements and high reliability; the nozzles are rounded and rarely have to be in contact with the moving medium. However, the energy consumption of the jet based systems are somewhat higher and the operating costs may become too high at higher production speeds, when the need for under-pressure increases.

The air of both suction and blow boxes should be calculated into the total hood ventilation and they can slightly contribute to the humidity level. However, due to the single-run geometries, the stabilisers are not in direct contact with the paper, but with the fabric. Therefore, the air fed into the stabilisers can be recirculated air, so that the heated supply air can be directed into the areas that need more ventilation. When recirculated air is used, some fresh supply air could be added so the humidity level of the stabiliser airflow does not become too high and to prevent the formation of condensate (Sundqvist, 2010, p. 452).

The runnablility systems are usually a combination of either active or passive stabilisers with different types of passive or active rolls. Since the passive stabilisers cannot create the under-pressures, they are paired with suction rolls which create the required under-pressures. Active stabilisers on the other hand can be used

independently to maintain the desired under-pressure, in particular in cases where the web tensions are allowed to be higher, as for instance in the drying groups closer to the dry end. The company Voith Paper GmbH, for instance, has a concept called ProRelease +, where the suction box forms the under-pressure and the box is combined with a perforated passive bottom roll. The box evacuates air, not only from the opening nip and the pocket area, but also through the holes of the perforated roll, formed an under-pressure over the perimeter of the passive bottom roll, securing a good runnability over the roll surface. (Voith Paper GmbH & Co. KG, 2017).

5.3. Fans in runnability systems

The theory behind transportation of gases is very similar to that of liquids, but the density is substantially lower for gaseous fluids, which sets some constraints on the transportation systems. The density is also very dependent on the temperature of medium. The density, ρ, of a gas can be calculated by:

$$\rho = \frac{\bar{M} \cdot p}{Z \cdot R \cdot T} \tag{21}$$

where $\bar{M}$ is molecular mass of the gas, p pressure of the gas, R is the ideal gas constant and T is the temperature of the gas. The compressibility factor is, Z, and for an ideal gas the compressibility factor can be approximated to Z=1, which gives the ideal gas law. Additionally, opposite to liquid fluids, the dynamic viscosity of a gas increases as the temperature rises. In transportation systems, the pressure and temperature variations are usually small and the gas can be considered incompressible (Westerlund, 2013, p. 136).

The objective of a fan is to increase the pressure of the transported gas. Fans rarely increase the pressure more than 10 kPa and for higher pressure increase, compressors and vacuum pumps can be used. The equations needed for fan calculations are derived from the energy balance of the transport system. When the volumetric flow can be assumed constant, the balance is:

$$\frac{\eta_i P_i}{\dot{V}} = p_p - p_s + \rho g\left(z_p - z_s\right) + \xi_p \rho \frac{w_p^2}{2} - \xi_s \rho \frac{w_s^2}{2} \tag{22}$$

where the index *p* indicates the pressure side of the fan and *s* indicates the suction side. When the inlet and the outlet of the fan are at the same level, the third term on the right-hand side is zero. The static pressure increase can be represented as $\Delta p = p_p - p_s$, and the dynamic pressure increase can be described as $\Delta p_{dyn} = \xi_p \rho \frac{w_p^2}{2} - \xi_s \rho \frac{w_s^2}{2}$. Thus, the total pressure increase produced by the fan is the sum of the static pressure increase and the dynamic pressure increase.

$$\Delta p_{tot} = \Delta p + \Delta p_{dyn} \tag{23}$$

Using Eq. 22 the internal power demand of the fan can be obtained:

$$P_i = \frac{\dot{V} \cdot \Delta p_{tot}}{\eta_i} \tag{24}$$

The shaft power can be obtained when the mechanical efficiency factor, η_m, is included (Westerlund, 2013, p. 138)

$$P = \frac{\dot{V} \cdot \Delta p_{tot}}{\eta_i \cdot \eta_m} = \frac{\dot{V} \cdot \Delta p_{tot}}{\eta} \quad (25)$$

5.3.1. Dimensioning and energy consumption of fans in runnability systems

The recirculation and supply fans of stabilisers are usually medium pressure centrifugal fans. The number of fans vary from 2-4 depending on the number of blow boxes and the machine width. When the total pressure difference and volumetric flow is known, the fan type and appropriate rotation speed is obtained by comparing the fan characteristics. The pressure losses in the pipelines are hard to determine and therefore the operating point of the fans are chosen so that the maximum efficiency line is always above the operating point. This ensures that the fan operates at a reasonable efficiency even if the pressure loss increases with time, due to, e.g., fouling of the pipeline. The air density is normally approximated to 1.2 kg/m^3 (Sikanen, 1998, p. 54).

In his thesis work of Sikanen 1998, he optimised the dimensioning of a runnability system and its fans based on the energy consumption and the web handling properties, proposing two ways for calculating the energy consumption of the systems. Either the energy consumption can be calculated by directly taking the power consumption of the fans for the runnability systems or by including the power consumption of the fans in the total evacuation and supply. The former procedure can be an overestimation, since the blow boxes are often also used for the supply air distribution. The total evacuation and supply is calculated through the total mass of water evaporated at the drying section and with the obtained value, the evacuated air can be calculated. The supply air flow is obtained, when assuming the leakage from the hood (which is approximately 20% of the total mass flow of dry air (Sikanen, 1998, p. 48)).

The dimensioning values in Sikanen (1998) are more suited for dimensioning of a new production line. However, when runnability upgrades are made of existing production lines, the supply air amount is maintained at the same level as before the upgrade. In the calculations performed in this thesis, the first calculation model is used, with only

the direct power consumption of the fans, because the pilot machine consists only of one drying position. However, in real paper machine environments the total air flow balance should be calculated.

6. Experiments – set-up and tested concepts

As noted in the previous chapters, web handling and runnability is a sum of many variables and comparing solutions just based on empirical knowledge and analytical inspection may not lead to accurate descriptions of the functionality of the concepts. Therefore, this thesis includes an experimental part, where selected concepts are compared with the same setup, so that some variables can be accepted as constant for all concepts. These variables are, for instance, ambient pressures, temperature and fabric and web properties. The experiments were conducted at a pilot machine in Valmet Technology Centre premises in Raisio.

In this chapter, the pilot plant geometries, tested concepts and the conducted measurements will be discussed. The technical aspects and validity of the trials are discussed in Appendix B and for deeper understanding on the measurements and technical details, the reader is referred to two Bachelor theses (Miulus, 2010) (Kulmala, 2012).

Figure 29 The pilot machine "Airi" at the Technology Centre in Raisio.

The pilot machine “Airi” in the Technology Centre in Valmet Raisio is built for research and development of runnability equipment. The pilot machine is seen in Figure 29. The machine width is 1000 mm and the fabric is driven as a closed loop over two upper and one bottom cylinder. The pilot machine is able to run at a maximum

speed of 2400 m/min and in the experiments of this thesis the speed interval 1000-1800 m/min was chosen.

Different runnability concepts were tested; a description of the concepts can be found in Section 6.1. At the pilot machine, only one position is run, the diameter of the two upper drying cylinders is 1850 mm and for the bottom cylinder the diameter is 1500 mm. The open draw between the upper and the lower cylinder is approximately 850 mm, a value taken from a technical drawing. The pilot machine is a single-run construction with one dryer fabric, where the chosen dryer fabric is a woven dryer fabric, which is widely used in paper and board machines. The permeability of the fabric is 110 cfm or 1750 m^3/m^2h, which represents a relatively impermeable fabric. The surface roughness of the fabric will affect the amount of air transported to the closing nip and consequently the pressures in the nip region (Carlsson, 1990). According to the marketing material of Valmet Technologies, the used fabric has lower air carry compared to other available fabrics (Paavolainen, 2015). Instead of running a paper web in the closed loop, the fabric surface was covered with masking tape and the permeability through the fabric is assumed to be very low or zero.

Measurements describing the runnability behaviour of different systems are mostly based on pressure measurements. The most valuable data was the pressure profile over the perimeter of the bottom cylinder, since similar data has rarely been obtained in large-scale pilot plants. The pressure profile was obtained by installing two types of pressure sensors at the cylinder surface. More details about the technical aspects of the measurements are found in Appendix B, where also the different sensors' compatibility to the measuring environment is checked. The sensors were installed in the casing of cylinder either on the bottom of the surface structure or on the roll land, depending on the concept. The sensors were positioned as indicated in Figure 30.

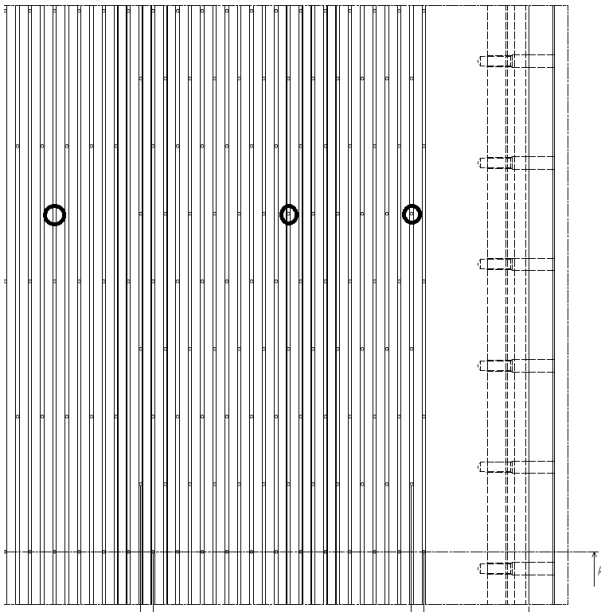

Figure 30 Positioning of the sensors on the cylinder.

One sensor was installed in the middle of the cylinder and it was more accurate and reliable compared to the other two sensors. The two less reliable sensors were installed at the edge of the cylinder; one just at the edge and the other in the tail threading area. The sensors were installed in two ways, either on the bottom of the surface structure or on the roll land by using a bolt. The two installation ways are seen in Figure 31, where the left-hand photo is on the roll land and the right-hand photo is on the bottom.

Figure 31 Installation of the pressure sensor on the cylinder surface

Other measurements made were pressure as point measurements. Three points were measured; the first point was from the opening nip of the dryer cylinder, the second from the pocket area and the third from the closing nip. The measuring points are seen in Figure 32, where the first point is just at the upper cylinders opening nip and the second is in the pocket area and the third is in the closing nip area of the bottom cylinder 250 mm from actual nip. The measuring pipes reach to the middle of machine cross-section.

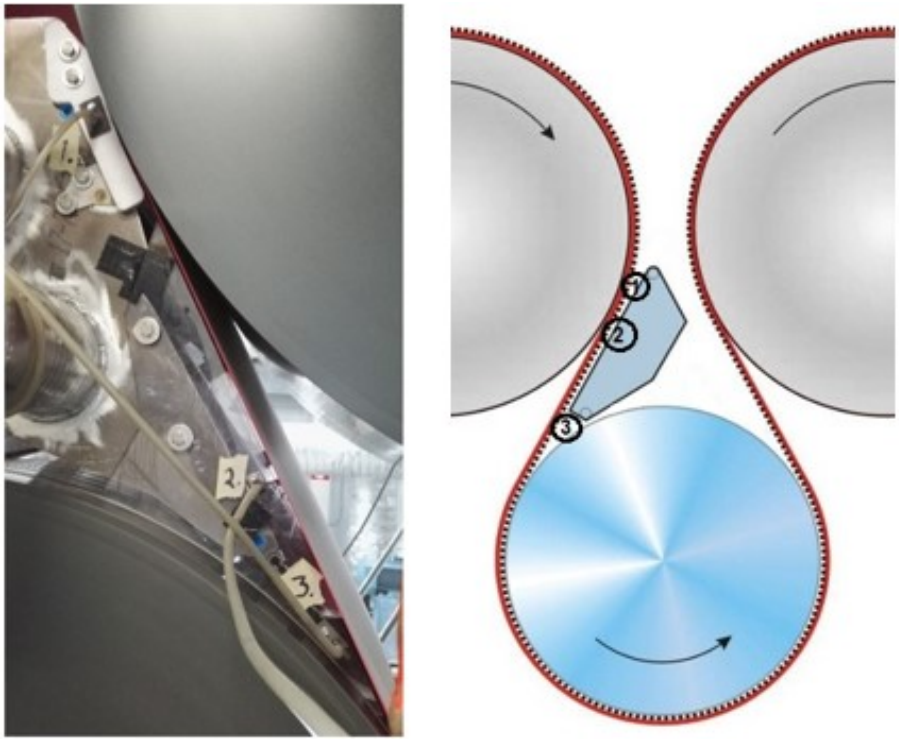

Figure 32 Point measurement places drawn.

The comparison made in this thesis focuses on the area of the bottom roll, more accurately on the closing nip area and the rotation over the cylinder, which is why merely measurement point 3 is of interest. The decision was made as there were several earlier studies of the opening nip of the drying cylinder, among them Leimu, 2008.

Several variables can be controlled by pilot machine auxiliary equipment. For the trials executed in this thesis, the running speed and fabric tension were important control variables. The web tension in the experiments was zero, since instead of a paper web, masking tape was taped on the fabric surface, which means that only the fabric tension can be modified.

6.1. Definition of the tested runnability concepts

The concepts chosen for the comparison in Chapter 8 will be referred to as Concept A, Concept B, Concept C, Concept D and Concept E. Concepts A, B and C consist of active bottom rolls with both active and passive stabilisers, whereas Concepts D and E are passive rolls with active stabilisers. The cylinders have four different surface structures and the cylinder is modified by taping masking tape on the surface. This might lead to some microstructures on smooth surfaces which could perhaps transport air and the surface roughness of the masking tape differ from the cylinder surface, which will affect the boundary layer.

In this section, a short description of the various concepts will be provided. The geometry of the drying group is preserved identical for all the concepts, as are the fabric and masking tape and the concepts are all tested in the same running speeds. The running speeds were chosen from 1000 m/min to 1800 m/min with intervals of 200 m/min. The ambient temperature and pressure were held constant throughout the testing and the average temperature was 20°C and pressure was atmospheric (101.3 kPa). The only exception is Concept C, which was tested as a part of another study and therefore the running speed as well as the sensor positioning differ.

Concept A in Figure 33:

- Cylinder: Active cylinder, where air is evacuated from the cylinder and the cylinder has an open area of 0.4% of the total cylinder area. The cylinder surface has carved surface.
- Stabiliser: Active stabiliser with upper and lower nozzles without seals. The nozzles create an under-pressure to disperse harmful effects at the upper drying cylinder and bottom cylinder. The upper nozzle targets the opening nip of the drying cylinder and the lower nozzle targets the closing nip of the bottom cylinder

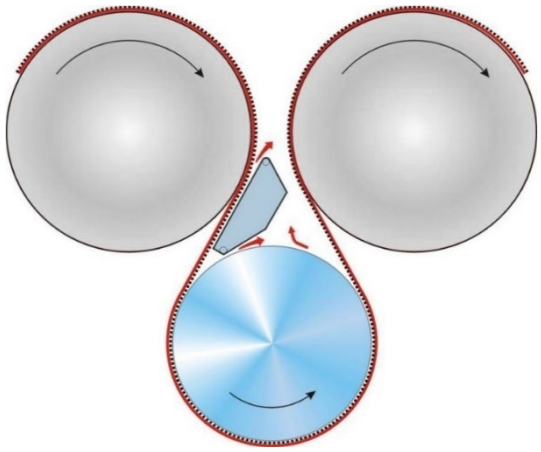

Figure 33 Concept A, active roll with surface structure and active stabiliser.

Concept B in Figure 34:

- Cylinder: Active cylinder, where air is evacuated from the cylinder and the cylinder has an open area of 0.4% of the total cylinder area. The cylinder surface has carved surface
- Stabiliser: Active stabiliser with upper nozzle and a doctoring plate to isolate the suction area. The upper nozzle targets the opening nip of the drying cylinder and the active roll stabilises the closing nip.

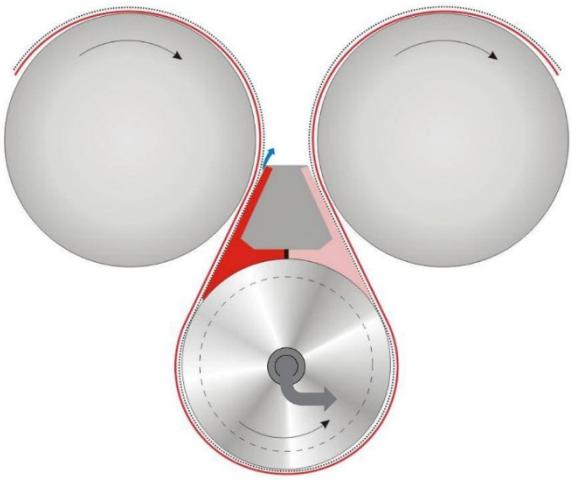

Figure 34 Concept B, carved active roll and active stabiliser

Concept C in Figure 35:

- Cylinder: Active cylinder, where air is evacuated from the cylinder and the cylinder has an open area of 0.4% of the total cylinder area. This cylinder does not have any surface structure and the surface is smooth.
- Stabiliser: Passive stabiliser, which isolates the pocket and the active roll can create the under-pressure in the pocket.
- The pressure sensors were installed in the middle of the cylinder and no sensors on the edge. The running speeds differ compared to the other concepts.

Figure 35 Concept C, suction roll and passive stabiliser.

Concept D in Figure 36:

- Cylinder: Passive surface and the surface of the cylinder is smooth.
- Stabiliser: Active stabiliser with upper and lower nozzle equipped with seals to break the boundary layer and restrict suction area. The nozzles target the same areas as the stabiliser in Concept A.

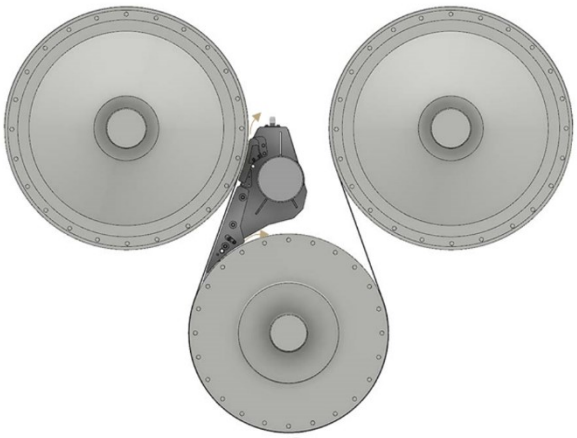

Figure 36 Concept D, smooth bottom roll and active stabiliser.

Concept E in Figure 37:

- Cylinder: Passive surface with a surface structure similar to the Surface A.
- Stabiliser: Active stabiliser with upper and lower nozzle equipped with seals to break the boundary layer and restrict suction area. The nozzles target the same areas as the stabiliser in Concept A.

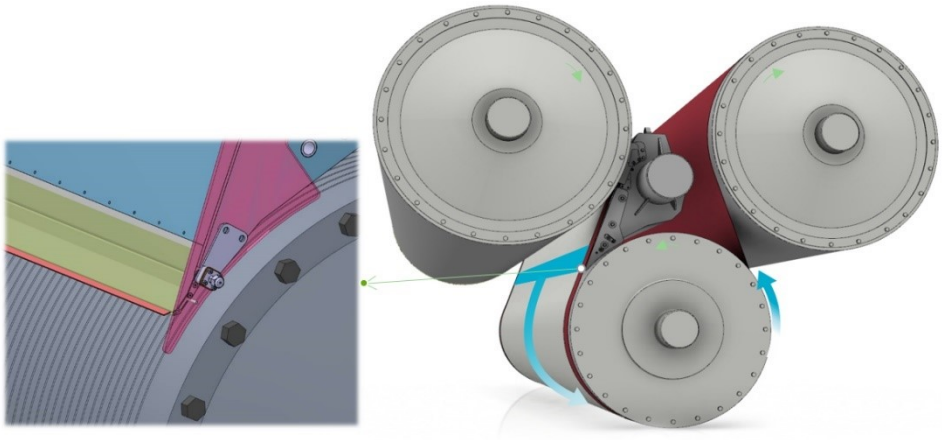

Figure 37 Left: Close-up of the closing nip. Right: Concept D, grooved roll and active stabiliser.

7. Results of the experiments

In this chapter, the results from the trials and the observations made based on the results will be analysed, putting special focus on the pressure profile over the rotation and measurement point 3, in the closing nip area. The aim is to identify the harmful effects and compare how the different concepts resolve them. This is done by first comparing the behaviour of the different bottom cylinder without any additional stabilisation and then the bottom rolls are combined with the stabilisers to see how the concepts really work.

7.1. Bottom cylinders

The concepts studied use three different bottom rolls, both active and passive and both with and without a surface structure. The diameter of the rolls is the same (1500 mm) and the geometries are identical, i.e., the wrap angle, incoming and outgoing angles are identical. The fabric is the same for each concept, as is the masking tape used to substitute the paper web, which makes the air carry of the fabric equal. The fabric tension is preserved at 4.5 kN/m. Additionally, it is worth mentioning that the active stabilisers are in place, but no airflow is blown out of the nozzles, so they work as passive stabilisers blocking the pocket area. The comparison of the cylinders will proceed from the passive cylinders to active.

7.1.1. Passive cylinder with a smooth surface

Figure 38 illustrates the pressure profile over one rotation of the cylinder of the smooth roll trials. The different solid lines represent different running speeds and the dashed line represents the closing nip. The rotation starts and ends at the opening nip. Due to creeping of the sensor during trials, the zero point is set at the cylinder top, where the pressure is assumed to be atmospheric.

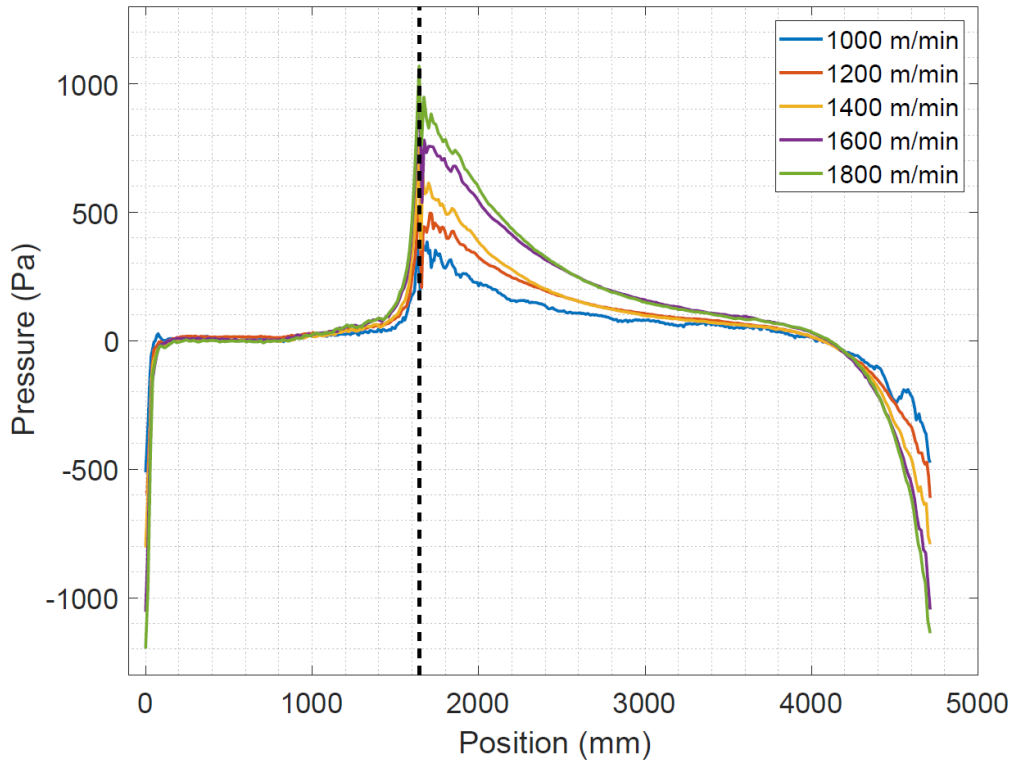

Figure 38 Results from passive smooth cylinder trials without active stabilisers.

From the figure, one can clearly see how the closing nip over-pressures depend on the velocity. As the machine speed increases, the boundary layer gets a higher velocity, and the air must then decelerate as the nip becomes narrower. The kinetic energy from the airflow is converted to pressure energy, seen as an increase in the static pressure (cf. Figure 38). As the machine speed is increased, the point where the over-pressure starts to rise occurs earlier, as seen on the left-hand side of the closing nip. The pressure measured in Figure 38 is at the cylinder surface, so it merely describes the static pressure directly at the surface. The point measurements were made from the pocket area, as described in Figure 32, which might better describe the pressure development before the closing nip at the fabric surface. Measurement point 3 was from the closing nip area, 250 mm from the actual closing nip. The results are given in Table 1.

Table 1 Point measurements for the smooth roll without active stabiliser

Machine speed (m/min)	1000	1200	1400	1600	1800
Point 3 (Pa)	37	48	65	80	90

The pressure development is similar to what was observed in Figure 38; as the web velocity increases the static pressure will increase. This development in static pressure might further cause displacement of the web, as the air presses the fabric and the web.

If Figure 38 is analysed by inspecting the pressures over the rotation, one can see that a static over-pressure remains even when the sensor passes the closing nip. This is likely due to the minor airflows between the fabric and cylinder and air also flows within the fabric structure (Karlsson, 1989, p. 44). If this is the case, the air within the structure will accelerate as the static pressure decreases. The driving force here is the high under-pressures of the opening nip. The over-pressure may also be a side effect from the forces acting over the rotation, the impulse from the closing nip together with the detaching centrifugal and gravitational forces. These impulses together may detach the web allowing airflow between the web and fabric.

The over-pressure over the rotation is undesired, since it adds to the detaching effects of the centrifugal force and the gravitational force. The negative effects can be compensated by added web tension, as demonstrated in Eq. (5). However, adding tension is not appropriate in the beginning of the drying section, where the paper is weak and the a low tension is desired. Another option is to find a way to eliminate the over-pressure peak and minimise the formed overpressure over the rotation, e.g. by applying active stabilisers.

The static pressure will decrease as the opening nip is approached and the air in the microstructures gains velocity. It is interesting to note that the under-pressure forms approximately at the same position for all the velocities, which would suggest that the influence of the closing nip is independent of machine speeds. Naturally, the magnitude of the under-pressure peak depends on the machine speed, which influences the boundary layer flow velocity.

7.1.2. Passive cylinder and with a carved surface

Surface structures on the cylinders are known to enable air to flow in through the structures instead of redirecting the flow away from the nip, which causes the over-pressure peak. Figure 39 illustrates the pressure profile results for the trials with a carved roll without active stabilising.

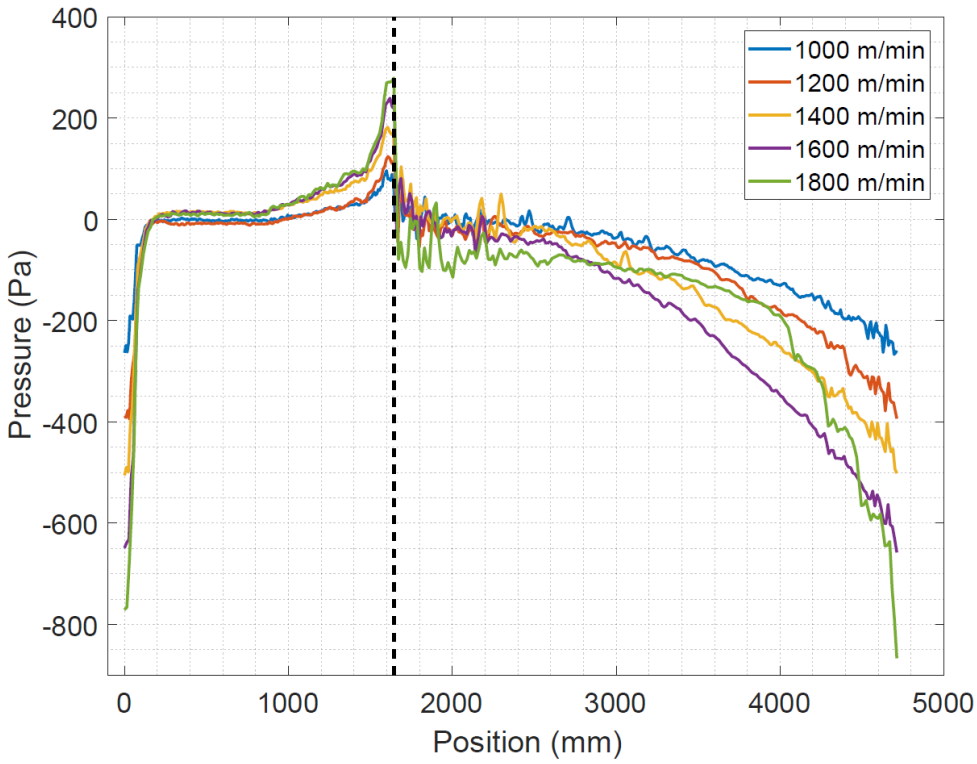

Figure 39 Results from the trials of the carved passive cylinder without active stabilisers.

The same tendencies as for the smooth cylinder are seen in the carved cylinder, the closing nip pressures increase as the machine speed is increased and, conversely, the opening nip pressures become lower when the machine speed is increased. The biggest difference, however, is in the magnitude of the pressures in the nips as well as the pressures over the rotation. Here it is worth pointing out that the pressure sensor is placed on the bottom of the surface structure, instead of placing it on the roll land, which of course affects the pressures since the flow conditions are different at the bottom of the surface structure and the roll land. However, the pressure peak in the

closing nip is significantly lower for the carved cylinder, so even at the roll land, the pressures must be lower compared to those of the smooth roll. Based on the results obtained from the pressure sensors, a regression model was developed for the passive cylinders and can be found in Appendix C. The result show that the nip pressure increases for the surface structured roll only by a forth for a unit of velocity compared to the smooth roll.

The closing nip pressures start to develop already at the cylinder top much earlier compared to the smooth roll, which may be due to the geometries of the carved roll. Because the cylinder has a surface structure, the area that can create the boundary layer is larger than for a smooth roll, which further suggest that more air is transported on the surface. As the sensor approaches the closing nip and the surface structures traps the surrounding air, the pressure increases already in a relatively early stage. The pressure peak, however, stays relatively low, since the air is allowed to escape into the surface structure and the deceleration of air is smaller compared to the smooth roll, which can be seen when the point measurements for the two cases are compared. Table 2 presents the point measurements of the surface structured cylinder.

Table 2 Point measurement for the passive carved roll

Machine speed (m/min)	1000	1200	1400	1600	1800
Point 3 (Pa)	31	42	55	73	82

As expected the pressures in the static points are somewhat lower than the corresponding points for the smooth roll. The pressures grow as the machine speed is increased and the boundary layer velocity increases.

As the air passes the closing nip, the static pressure instantly drops below the ambient pressure, i.e. the velocity of the air inside the structure grows rapidly. The same results were found by Nurmi, cf. Figure 13 in (Nurmi, 2009, p. 69). This is due to the driving force caused by the pressure difference between the opening and closing nip. Air flows spontaneously from the closing to the opening nip, so the decrease in pressure is due to the pressure losses over the structured surface. The under-pressure through the

rotation is beneficial, since it will act in the opposite direction of the centrifugal and the gravitational forces, due to the pressure difference over the web. This will support the web and fabric on the cylinder surface.

The shape of the pressure loss curve is interesting; the pressure loss over a pipe should be linear, if there are no leakages. In the model presented in Subsection 5.1.1, the pipe was modelled with minor leakages, which would be due to the permeability of the fabric. The same kind of curvature can be seen in the real results. Simulation with boundary conditions from the real results gave the pressure profiles in Figure 40.

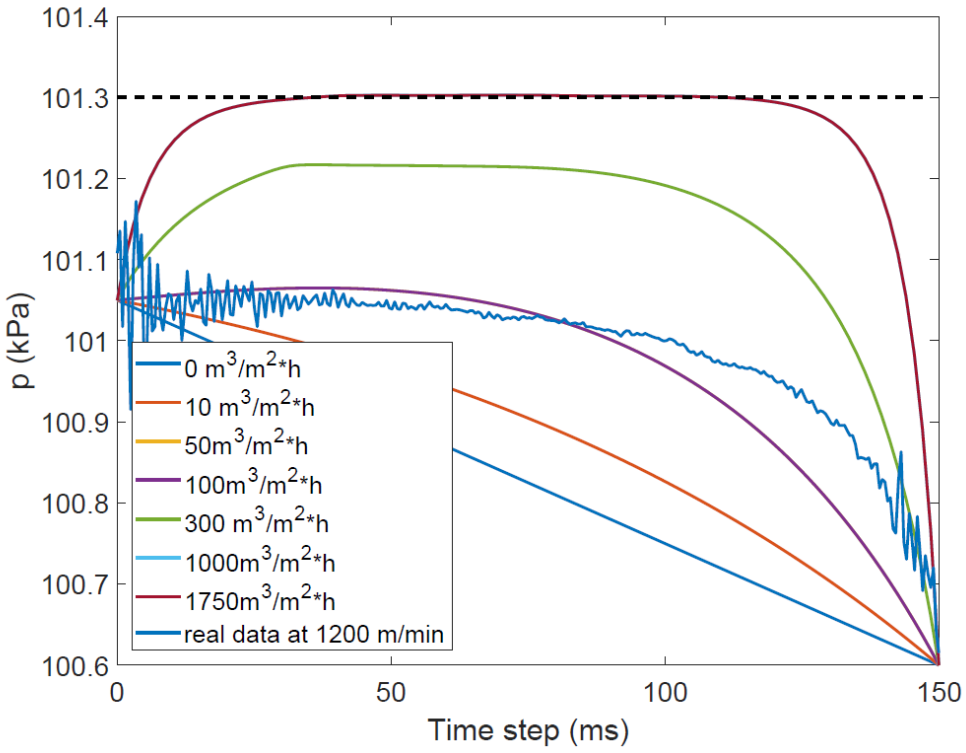

Figure 40 Simulation results and real results.

The results suggest that some leakages occur in the structure, even though leakage seems to be improbable, because the fabric together with the masking tape should be almost impermeable. The profile can possibly be explained by the communication between the different structures on the cylinder. If there is a small gap between the fabric and the roll land surface, the air can move between the cylinder structures or move within the structures of the fabric, which could explain the curvature of the pressure profile.

7.1.3. Active cylinder with a surface structure

The carved suction roll differs from the former cylinders because it is an active cylinder and the functionality of the suction roll is based on the evacuation of air. Therefore, the system will be studied at one machine speed with varying degree of evacuation from the roll. The five different cases studied lead to the pressure profile presented in Figure 41 and the airflows creating the suction are given as relative values. The pressure sensor was on the bottom of the structure, which has to be taken into consideration when analysing the results.

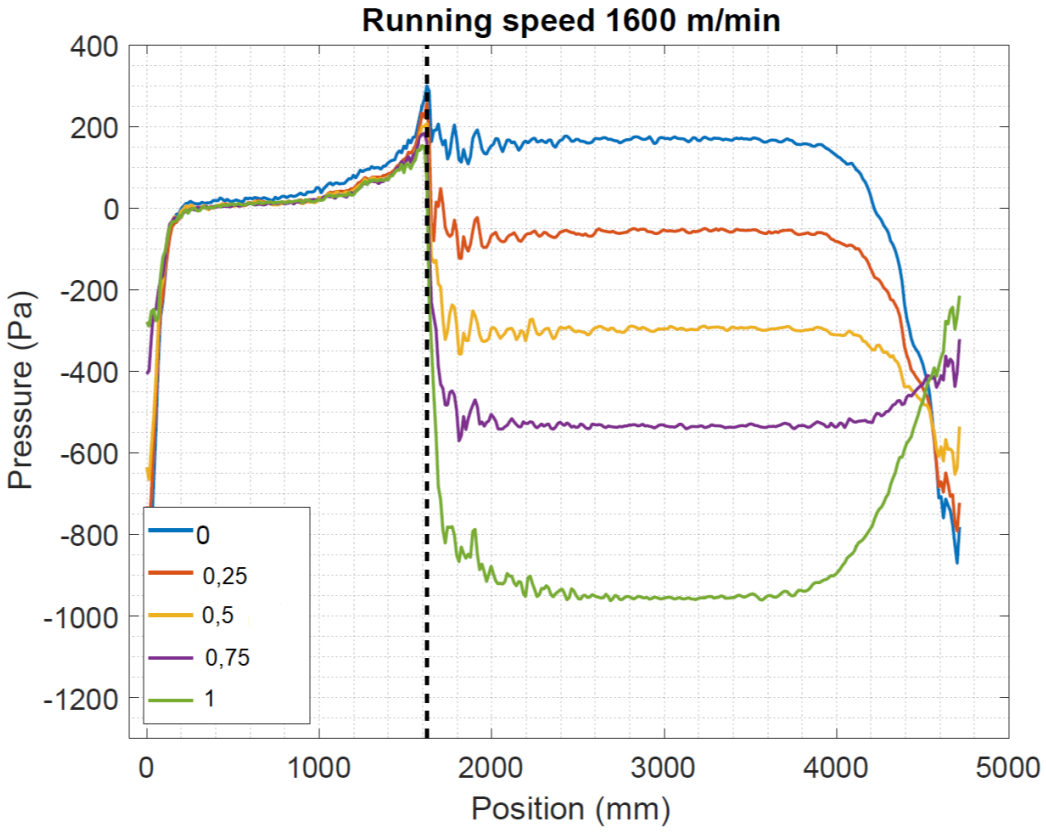

Figure 41 Suction roll without stabilisers, at a running speed of 1600 m/min and different evacuations

When the sensor approaches the closing nip, the same phenomena as for the carved roll can be seen; the pressure increase begins on the cylinder top and the reason is likely to be the same as for the carved roll. The closing nip behaviour is similar to that of the carved roll, but the over-pressure is slightly lower since air is evacuated from the closing nip, causing a smaller pressure peak. Still, the pressure peak is not significantly lower, which would suggest that the surface structures are a more decisive

factor for the closing-nip pressures. The results for the point measurements in Table 3 describe the influence of the suction on the peak development:

Table 3 Point measurement for the suction roll without active stabilisers.

Airflow	0	0.25	0.5	0.75	1
Point 3 (Pa)	124	107	96	90	87

As expected, when air is evacuated through the holes, the pressure in point 3 is lowered. However, the pressure is not lower than the corresponding value for the passive carved roll. This may be due to the lack of lower sealing in the stabiliser, because the boundary layer development on the fabric is disturbed by the mechanical seal.

The pressure profile over the rotation is dependent on the air flow evacuated from the cylinder, so different under-pressures are obtained. If there is no airflow through the holes, there is an over-pressure, most likely due to rotational movement, which forces air out of the cylinder. When the fan is turned on and air is removed from the cylinder, an under-pressure is established already at relatively low evacuation.

As seen from Figure 41, the under-pressure over the rotation is quite high, especially for the dimensioning value (curve marked by “1”). With reference to Subsection 3.2.1 and specifically to Eq. (5) and the results in Figure 5, one may note that the recommended value gives rise to a relatively high pressure difference compared to the other terms acting on the web. Within the grammage range of 100-300 g/m^2 the other terms correspond to pressures around 50-250 Pa. Clearly, the pressure is high enough to secure the web on the surface and probably the large pressure difference is used mostly to equalise the negative effects of the closing nip (Kauppinen, 2018, p. 59).

When the opening nip is studied, for certain volumetric flows, a strong under-pressure peak appears, but for the larger suction the peak disappears. This could be explained by the joint effect of the groove and the evacuation. At the opening nip the air will cause an inflow of air into the nip. The inflow velocity is, however, slower compared to the outgoing flow, which causes a large decrease in static pressure. When suction of the cylinder is applied, the incoming flow will have a larger velocity, which means

that the large under-pressure does not occur, as the suction roll sucks air into the groove.

7.1.4. Active cylinders with a smooth surface

In this section, the active cylinder with a smooth surface is studied in the same manner as in the previous section. Different suction airflows are compared as relative values, where one corresponds to the current dimensioning value. The difference to the previous case is that the whole pocket area is blocked by the passive stabiliser. Since Concept C was a combination of the passive stabiliser and active cylinder, the results in Figure 42 are the complete results.

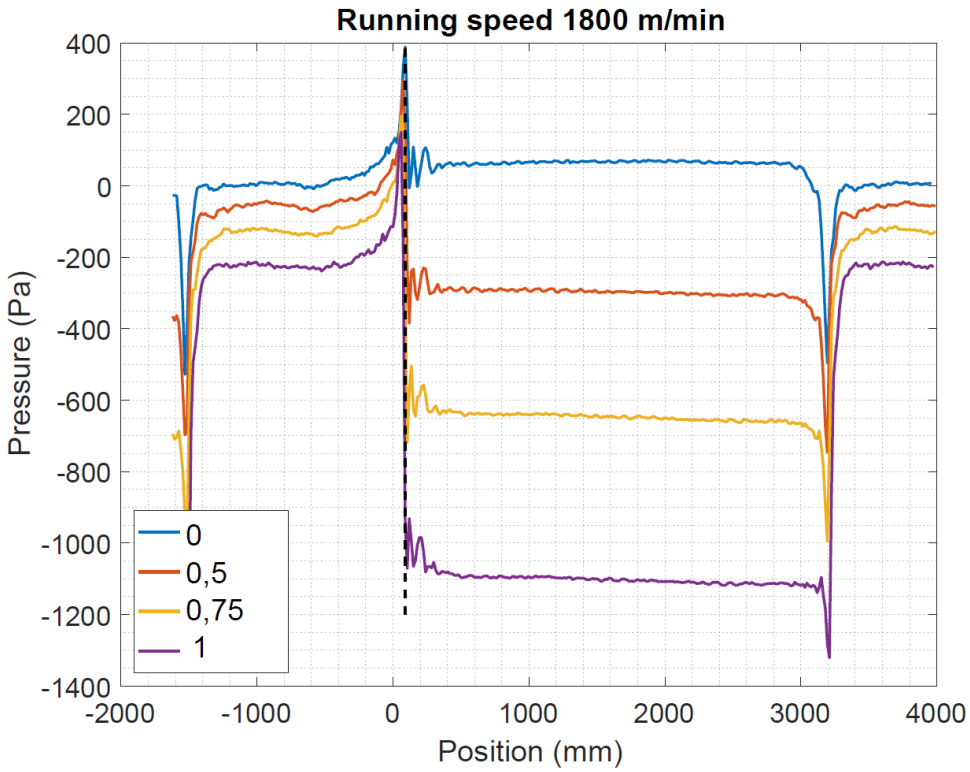

Figure 42 Perforated suction roll with different suction from cylinder.

The pressure profile for the perforated suction roll reminds quite much of the other active cylinders pressure profile. The biggest difference is seen on the top of the cylinder, where passive stabiliser isolates the suction area of the pocket, which creates

a under-pressure area in the pocket. The closing nip pressure starts rising and here the absence of the grooves can be seen. The peak pressures become larger for this bottom cylinder compared with the grooved one, i.e., the boundary layer behaves similarly to a smooth bottom cylinder. Of course, the closing nip pressures are lower for the active cylinder, since air is constantly removed from the boundary layer at the cylinder.

Over the rotation, the pressure profile is also similar to that of the active carved cylinder; quickly after the closing nip the static pressure decreases. The shape of the curve is somewhat sharper compared with that of the structured roll, which is probably also due to the grooves, since with the grooves air can travel longer into the structure compared with the smoother active roll. When the opening nip is approached, the same kind of deep pressure peak can be found for the smooth active roll, as for the carved active roll in Figure 41 and in the results of Kauppinen (Kauppinen, 2018). The reason is likely to be the difference of the velocity of the outgoing and incoming air flows. For the active smooth roll, the peak occurs even at high suction levels due to the absence of grooves. When the cylinder is grooved the suction can operate in a larger area compared to a cylinder without grooves and a larger inflow is induced neutralising the pressures.

7.2. Complete concepts paired with stabilisers

The objective of the stabilising equipment is to reduce the forces that create undesired movement of the web. Most of the stabilising equipment are based on the concept of creating a pressure difference over the web and fabric, which opposes the detaching force. As will be seen in this section, the strategy for removing the negative effects differ in the concepts, which makes a comparison somewhat complicated. For example, it is known that the suction roll is able to balance out the negative effects of the closing nip, even though an over-pressure peak appears at the closing nip. This is because of the high under-pressure right after the closing nip, which quickly acts in the opposite direction of the closing nip peak pressure. The support is produced by large under-pressures that hinder the detachment of the web.

Therefore, it is difficult to decide the conditions where the web is secured and where it detaches, especially when only the static pressure is considered. Immonen et al. 2009 defined the limit by simulating web deflections using a 2D FSI model. The model took in consideration the tension of the web and the net effect of acting forces. The forces considered were pressure forces due to pressure difference, adhesion forces between the web and fabric, centrifugal forces and gravity (Immonen, et al., 2009). As it is difficult to determine the net effect of the forces, especially in the nip areas, the present author made the simplification of defining good runnability as the solution where the peak pressures in the closing nip is low and the pressure over the rotation of the cylinder is low enough to overcome centrifugal and gravitational forces together with web tension.

The airflows from the stabilisers and the suction rolls are compared by normalising the values to the dimensioning values of the equipment.

$$y = \frac{\dot{V}}{\dot{V}_{dim}} \qquad (26)$$

This will simplify the comparison and clarify whether the systems studied are over-dimensioned or not.

7.2.1. Concept A

Concept A is a combination of the suction roll and an active stabiliser. The stabiliser is a blow box equipped with two nozzles, upper and lower nozzle without any mechanical seals. In the trial of this concept, the airflows through the nozzles were kept constant and different airflows were evacuated from the suction roll. This concept is known to work at even top velocities, which is why the machine speed of 1800 m/min was chosen for comparing the airflows in Figure 43.

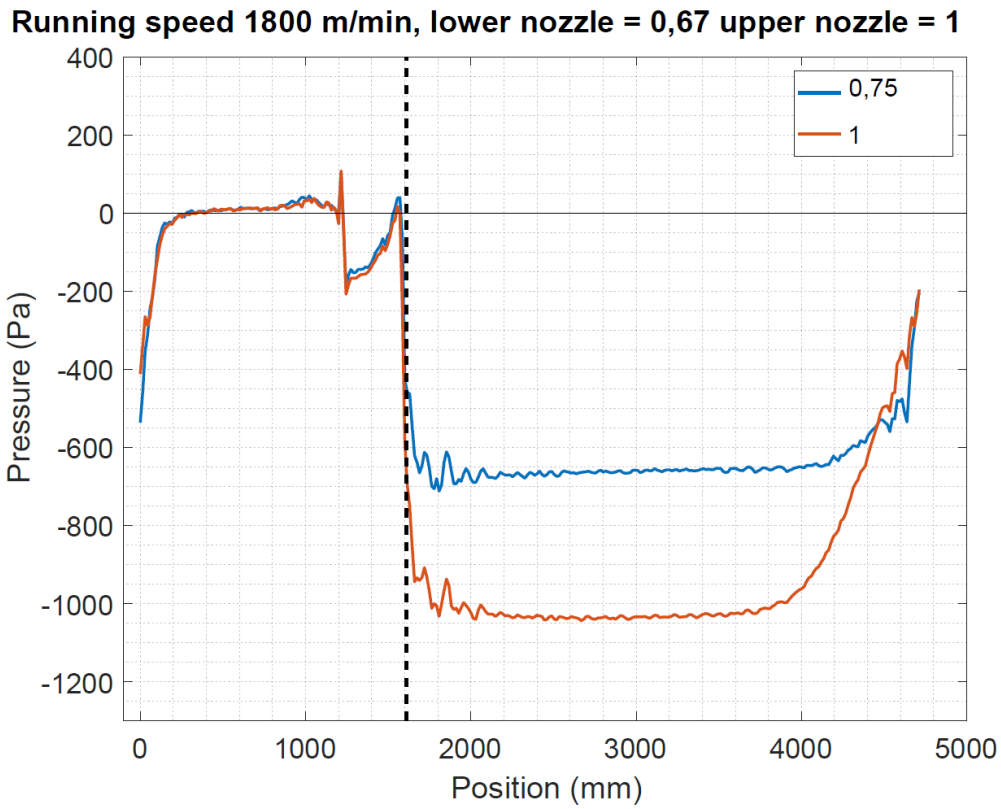

Figure 43 Concept A at 1800 m/min running speed with varying suction.

Compared to Figure 41 the effect of the stabiliser is clearly seen. The lower nozzle creates an air-flow in the direction of the cylinder top, which is why a small over-pressure can be seen on the top of the cylinder. This is likely due to airflows colliding with each other, which slightly decelerate them, causing the minor static pressure increase. The slight pressure increase is followed by a over-pressure peak by the air knife of the blowing nozzle. The positive peaks before the nozzle will not affect the paper web, because they occur on the top of the cylinder, relatively far away from the web.

As the pressure sensor passes the nozzle, the static pressure is below atmospheric due to the ejector effect of the nozzle causing flow away from the nip area. Regardless of the efforts of the nozzle, the pressure rises due to the nip effect, but the pressure must still be considered sufficiently low. The extent of the positive peak differs only slightly between the two airflows, which would suggest that the effect of the suction from the roll is minor on the closing nip compared with the stabiliser.

The small positive peak is not likely to affect the paper web, since the following under-pressure is much higher, which will secure the web on the cylinder surface. The amount of air sucked through the holes will naturally affect the magnitude of the under-pressure in the groove. When more air is evacuated, the pressure decreases.

The pressure difference over the web will create a supporting force as expressed in Eq. (5). The larger the support force is, the smaller the tension on the web have to be. Smaller web tension is desired, because it allows the usage of shorter and recycled fibres, which have lower strength especially in the beginning of the drying section and are than virgin fibres.

The detaching forces, however, are constant for the running speed and grammage weight, when the ideal case is considered. For the running speed in Figure 43 and grammages varying from 100-300 g/m^2, the sum of the gravitational and centrifugal forces corresponds to a pressure of 90-270 Pa, which is clearly less than the support pressure provided by the pressure difference over the web. Of course, one should keep in mind that the reasoning is for the ideal case and that neither aerodynamic and other forces nor the fibre bonds are considered.

In Figure 43 the closing nip pressure peak cannot be clearly seen and, interestingly, the pressure starts rising earlier when the airflow is higher. This may be because the suction will induce flow into the cylinder structure from the opening nip, due to the pressure difference between the groove and the opening nip.

Because the under-pressure is almost double the magnitude of the detaching pressure in the ideal case, the smaller airflow is chosen for a comparison of velocity changes. Results for various velocities and constant airflows are presented in Figure 44, which is just like Figure 43, shows that only the magnitude of the effects differ. For instance, the minor pressure rise before the air knife becomes larger as the machine speed is increased, as does the pressure peak of the air knife. The pressure rise is likely to reflect the velocity and the magnitude of the boundary layer on the surface of the cylinder. For the same reason the downward pressure peak, caused by the nozzle, is lower for higher velocity and the closing nip pressure is higher.

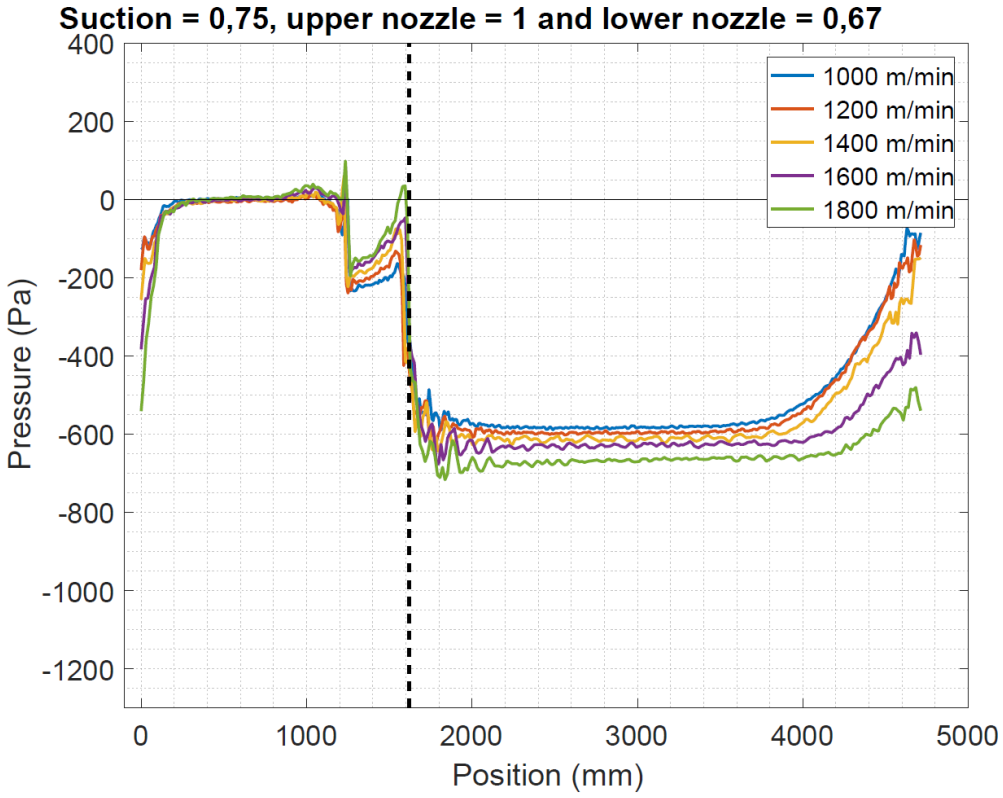

Figure 44 Concept A with various running speeds.

When the sensor passes the closing nip the pressure decreases below ambient pressure as expected. However, even though the evacuation from the closing nip is equal at all velocities, the static pressure seems to decrease as the machine speed is increased. When the velocity of the groove and fabric increases, so will the velocity air, which will increase the dynamic pressure in the groove and consequently the static pressure is lowered. The same effect has been observed in real production lines; as machine speed is increased a smaller evacuation air flow is needed.

As the sensor approaches the opening nip, the pressure starts rising at different points. The pressure rise begins earlier, when the velocity is lower. This may be dependent on the air flow velocity, which is higher at higher running speeds. The air in the structure will have hinder the ambient air from flowing into the lower pressure area. The principle is the same as for the blowing nozzle. With lower velocities, the kinetic energy is not high enough to hinder the inflow, which causes the pressure to rise in an earlier stage.

In web handling, the edge is commonly the limiting factor and normally the runnability issues are first detected at the edges. The edge area is usually of lower quality and the support forces, such as tension and friction forces, are lowest at the edges. Therefore, the edge areas should also be compared when the runnability concepts are studied. The pressure profile at the edge area for the same trials, as in Figure 44, is presented in Figure 45. The results in the figure should be taken merely as indicative since the measurement accuracy of the edge sensor was too low for the dynamics of the system (cf. Appendix B).

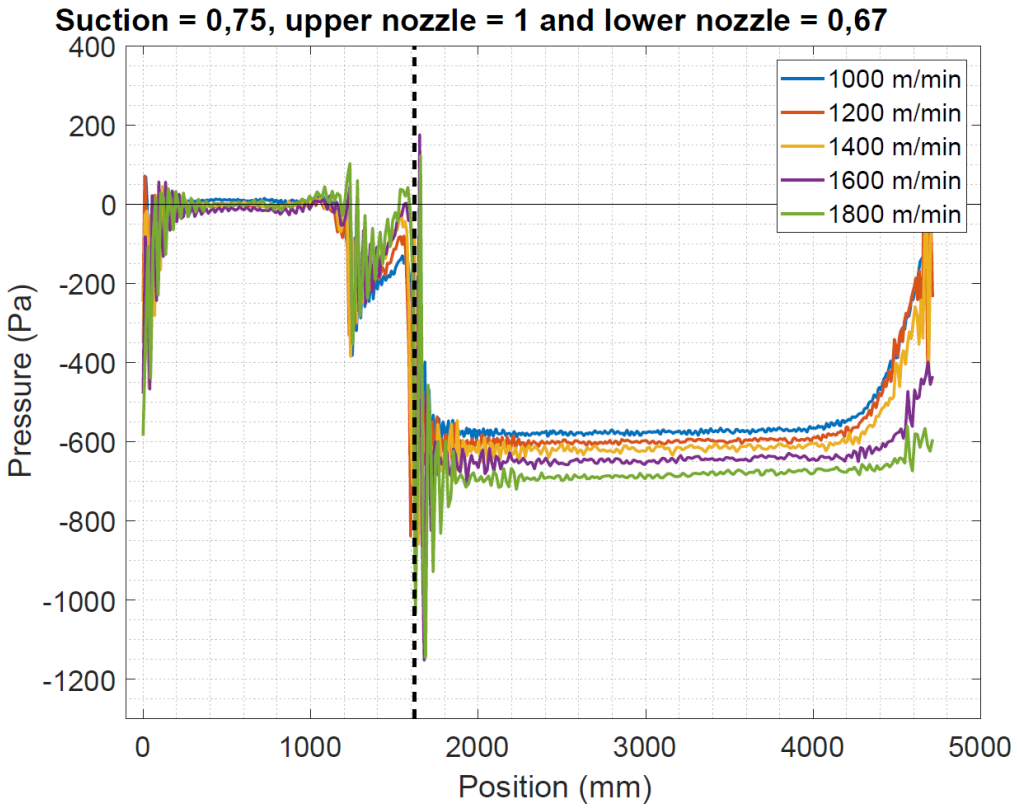

Figure 45 Edge area for Concept A at different running speeds.

The shape of the curves are seen to be the same as for the middle part and the magnitude of the pressures are also in the same range. The closing nip over-pressure may be slightly larger. However, the measurement accuracy does not allow for direct comparison. Over the perimeter of the roll, the edge is subjected to the same forces as in the middle, but turbulences and the pressure forces more easily result in undesired web fluttering. This can be seen as a higher pressure at the perimeter. However, the under-pressure seems to stay at the same level as in the middle, which suggests that

there is little leakage from the surrounding at the edge. Since the measurement was made at the roll land just by the edge of the masking tape and two grooves were between the sensor and the surrounding, the evacuation of the two grooves could hinder crossflow of air towards the middle area, which could explain the high under-pressures also at the edge.

7.2.2. Concept B

Concept B is also a grooved suction roll with an active stabiliser. The active stabiliser in this concept has only an upper nozzle to control the opening nip of the upper cylinder and a doctor blade, equipped with a mechanical seal, directed on the cylinder surface. The aim of the doctor blade is to restrict the under-pressure area, so that less work is needed. The concept was compared with Concept A. Firstly, the airflows are compared in Figure 46. The results are quite similar to those for Concept A, but the biggest difference occurs in the area around the closing nip. The doctor blade is farther away from the closing nip and there is no nozzle reducing the local over-pressure.

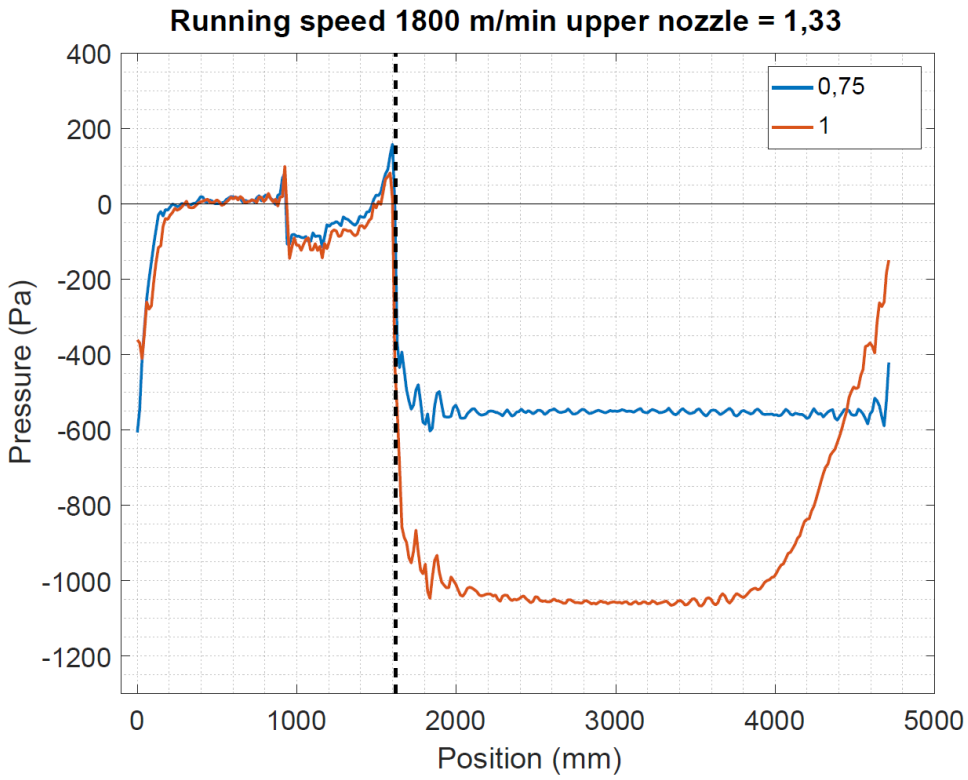

Figure 46 Concept B with different evacuation airflows.

The effects of the doctor blade are clearly seen in the results, as the sensor is just at the doctor blade as the pressure jolts. The air hits the plate with high velocity creating an over-pressure, which gives the small peak in static pressure and therefore the extent of the boundary layer is reduced. As the sensor passes the plate, the static pressure decreases, due to the removal of air partly through the holes in the grooves and partly through the upper nozzle. The boundary layer develops as the sensor moves towards the closing nip and the pressure peak is somewhat positive. The amount of suction air appears to be more decisive in this concept compared to the former. The pressure peak for the lower suction is around 50% larger than for the higher.

The same evacuation airflow is chosen and the velocities are compared in Figure 47. The peak pressures are much higher for Concept B compared to Concept A. As the velocities grow above 1400 m/min the peaks become positive and at the machine speed of 1800 m/min the pressure peak for Concept B is four times larger than for Concept A.

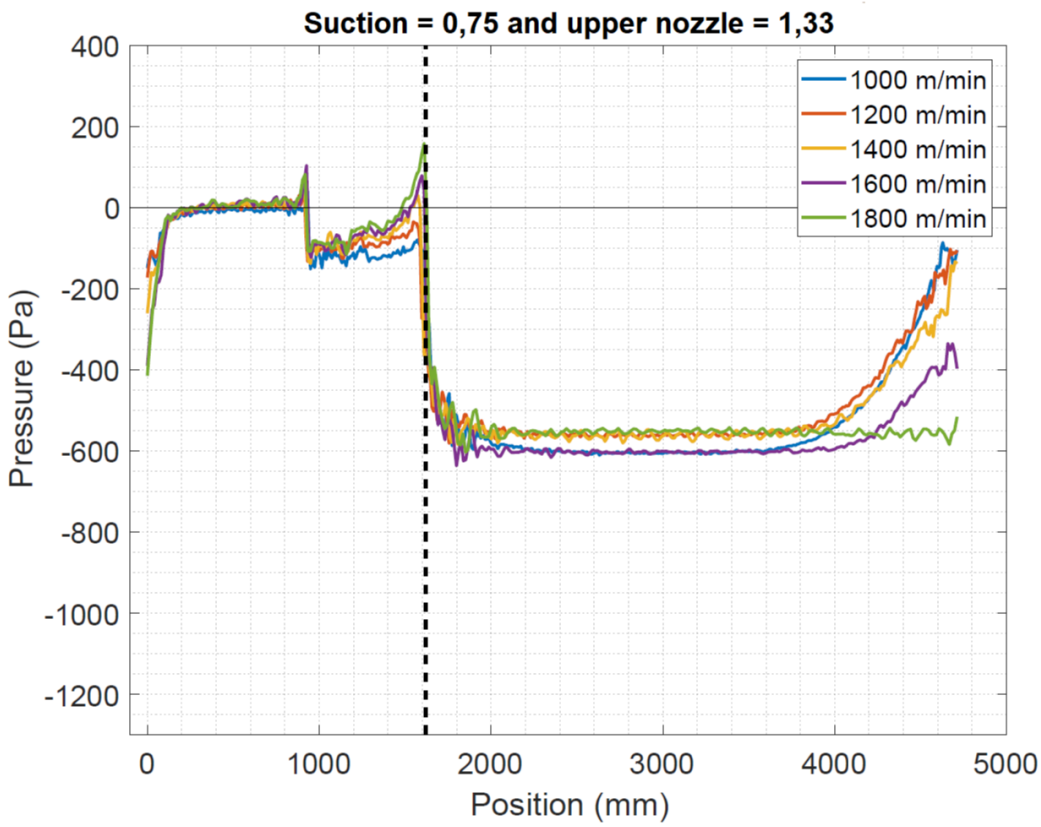

Figure 47 Concept B comparison with different velocities.

Because the web is tightly secured around the closing nip area, it is hard to determine, if this pressure peak would cause detachment, thus increasing the risk for web break. To be able to determine the detachment, experiments or simulations should be undertaken. For this reason, the recommendation is simply to avoid any over-pressure peaks.

The edge area for Concept B is very similar to that of Concept A. The under-pressure seems to stay at the same level at the edge as in the middle, which means that air is not leaking into the groove from the surroundings. The differences are mostly seen in the over-pressure nip, where the pressures are higher for Concept B. The pressure at the edge is completely below ambient pressure over the whole rotation, as seen in Figure 48.

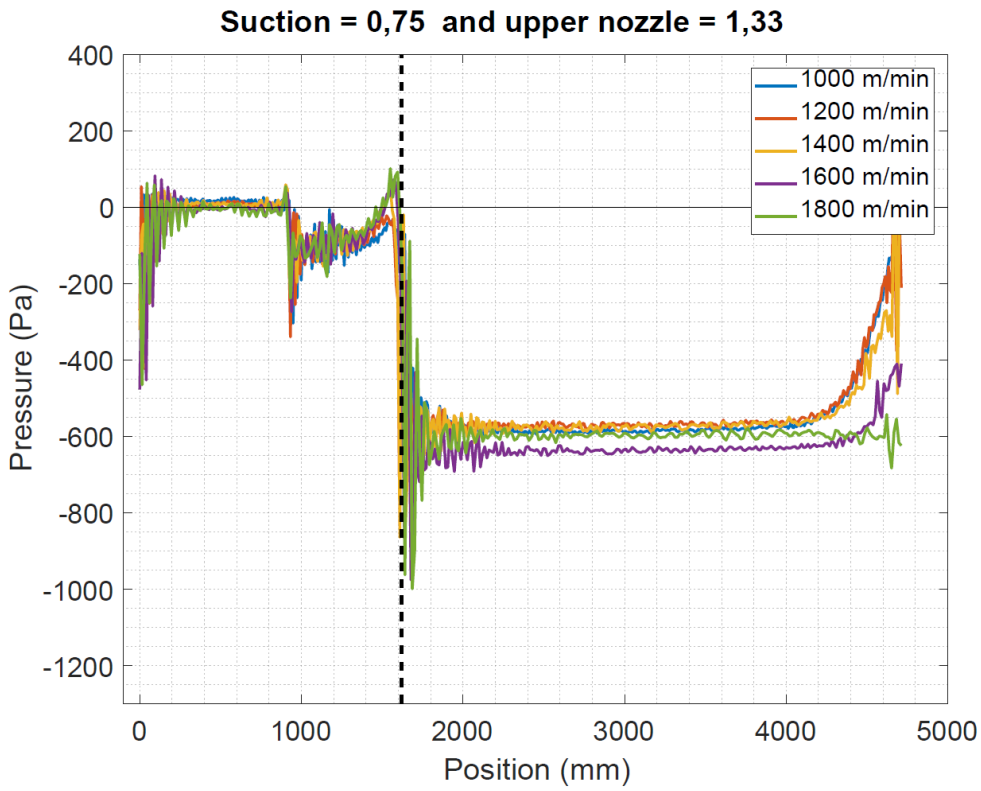

Figure 48 Edge area for concept B

7.2.3. Concept C

Concept C is a combination of the perforated suction roll with a passive stabiliser. The passive stabiliser isolates the whole pocket area, as seen in Figure 42, where the concept was already compared with different airflows at one machine speed. Based on the results in the figure, it was evident that the suction was not sufficient to completely eliminate the over-pressures of the closing nip.

For this reason, comparison of the velocities we made with the volumetric flow that was originally the dimensioned evacuation condition from the cylinder, which was the largest volumetric flow tested. The results are presented in Figure 49.

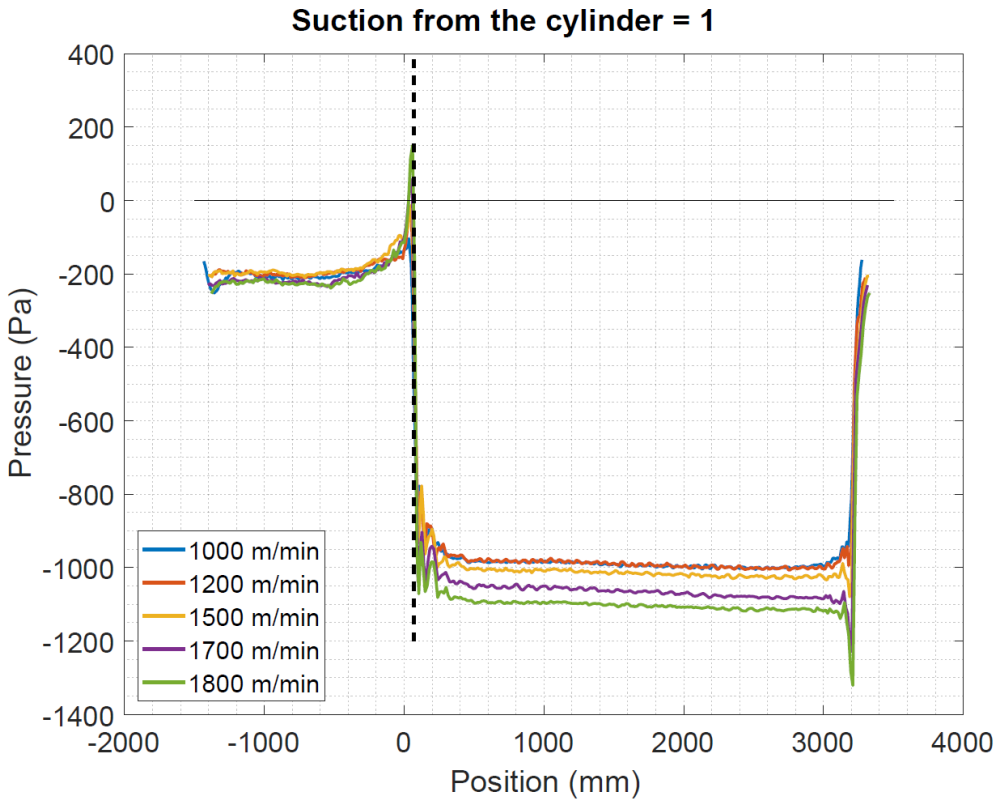

Figure 49 Concept C with varying velocities, currently dimensioned suction.

As expected, the pressure peak increases as the machine speed increases. When velocities over 1500 m/min are reached, the closing nip gets an over-pressure. Very likely, the actual web will not be affected by this over-pressure due to the large under-pressure caused by the suction, similar to Concepts A and B. However, to accurately determine whether the runnability over the closing nip is controlled or not, the system should be simulated, especially since there are, to the best of the author's knowledge, no reference machines using the concept. Therefore, one cannot determine whether the web is secured or not merely by inspecting the test results.

The dimensioned suction creates a relatively high under-pressure for velocities below 1500 m/min. Therefore, a lower air flow could be evacuated from the cylinder, which would save energy. The pressure profile for the lower airflow is presented in Figure 50.

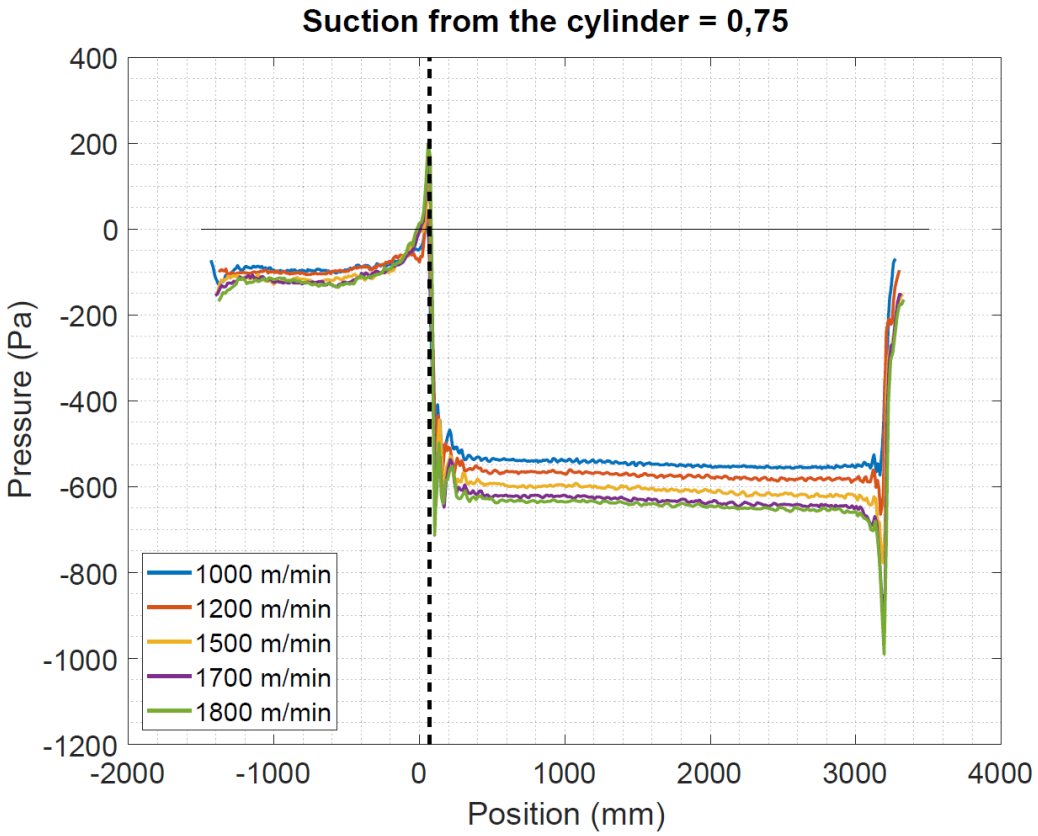

Figure 50 Lower evacuation from cylinder.

The pressure does rise in the closing nip over the ambient pressure for all the velocities. For the lowest machine speed the pressure is only slightly above atmospheric, which would suggest that the lower evacuation is plausible for the lowest machine speed.

Due to lack of data on the edge area of the perforated suction roll, a comparison cannot be made for the edge area.

7.2.4. Concept D

In Concept D, the role of the active stabiliser is increased as the cylinder is passive and does not have grooves to equalise the pressures. The smooth roll is paired with an active stabiliser with an upper and a lower nozzle, which are meant to reduce the effects of pressure peaks in the opening nip on the upper roll and the closing nip for

the bottom roll. Mechanical seals are in contact with the fabric to reduce the pressure areas.

Figure 51 compares the effects of the airflow for the case with a constant running speed. The letters in the legend represent the nozzle in use (lower nozzle, *L*, or upper nozzle, *U*).

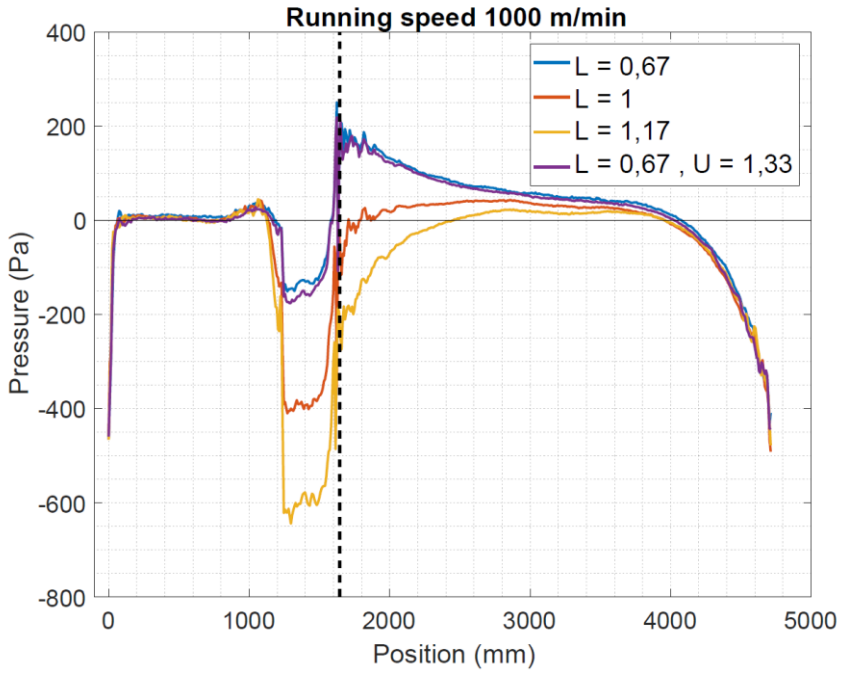

Figure 51 Concept D at the running speed 1000 m/min and various airflows.

The results can be compared with those of Figure 38 where one should note that the scale is different. The over-pressure peak is clearly reduced by the effect of the stabiliser. Without any stabiliser, the over-pressure is approximately 400 Pa and with only low volumetric flow, the pressure increase is reduced to about half.

The effect of the stabiliser is seen just before the closing nip, where the ejector creates an under-pressure area and creates a surge of air out of the wedge area. Regardless of the high under-pressure, the pressure increases in the nip to yield a slight over-pressure over the perimeter. Increasing the airflow of the nozzle is not possible, since larger pressure differences cause fabric bending, which might tear the seams of the fabric. The small over-pressure may not cause displacement of the web, but the risk increases as the pressure increases. If the web tension can be increased, the support can be enhanced (cf. Eq. 5) to oppose the centrifugal and gravitational effects.

At low velocities the volumetric flows above the dimensioned flow are plausible with respect to the boundary conditions of the comparison. Therefore, these set-ups will be studied. Figure 52 shows the pressure profile for a case where the lower nozzle blows at the dimensioned volumetric flow. Because there are no pressure differences over the fabric and web providing support forces, the pressure difference over the perimeter and in the closing nip should be as close to zero as possible.

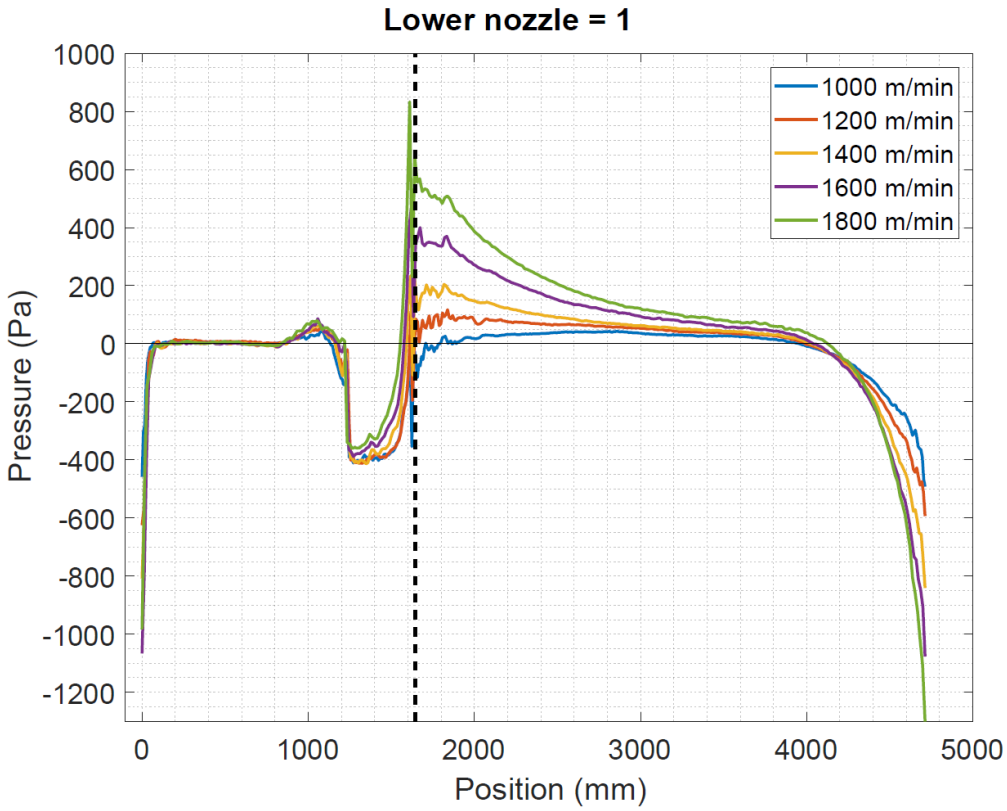

Figure 52 Concept D with various velocities and the currently dimensioned volumetric flow.

The case with the pressures closest to atmospheric is for the machine speed 1000 m/min, where the over-pressure is approximately 40 Pa. If the force balance of Eq. 5 is used for the values from the trial, the required tensions for grammages between 100-300 g/m^2 are 58-115 N/m. It might not be possible to reach such tensions in the beginning of the drying section, especially if the quality of the fibres is low.

By increasing the airflow, greater under-pressures can be reached. When the airflow of the lower nozzle is increased, the under-pressures increases, as is seen in Figure 53. With only a slight increase the volumetric flow, the pressure over the perimeter is lowered almost atmospheric.

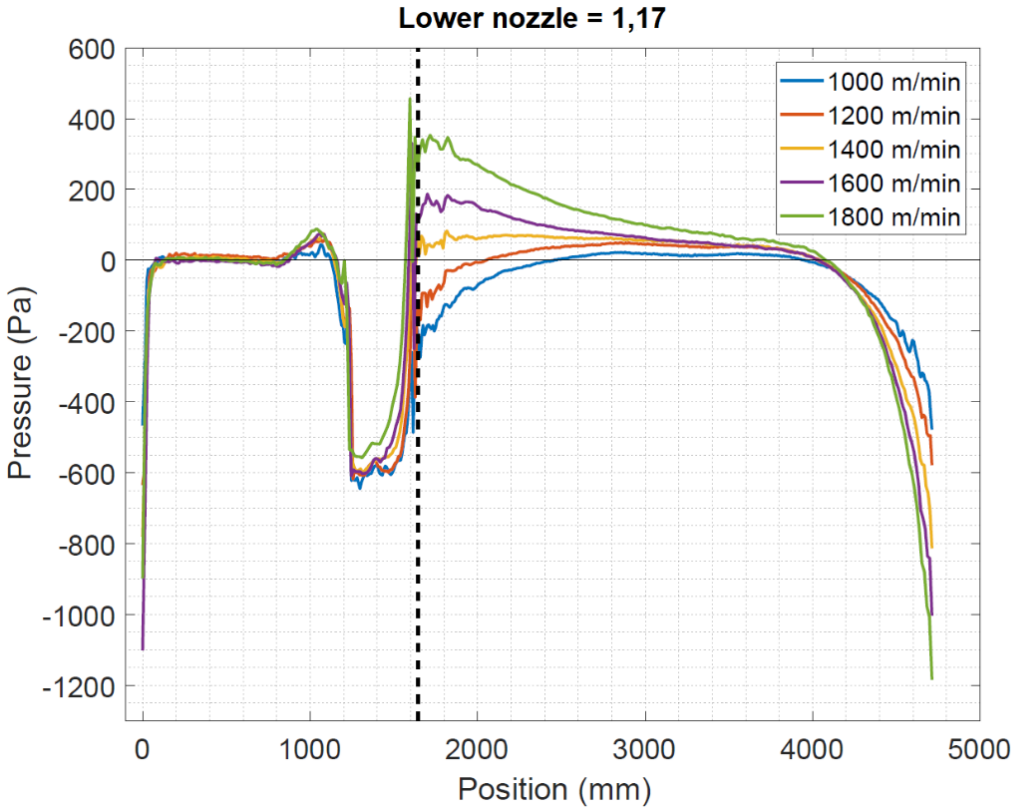

Figure 53 Concept D with various velocities and 17 % higher volumetric airflow through the lower nozzle.

Nonetheless, the runnability of Concept D cannot be guaranteed, if the pressure is significantly positive and the tension is not compensating for the over-pressure.

It is worth comparing the edge area of the web. Most likely, the edge pressure is closer to atmospheric and higher compared to the cases with the suction roll, since air can escape into the edges, increasing the pressure. The pressures measured by the edge sensor for the trial are presented in Figure 54.

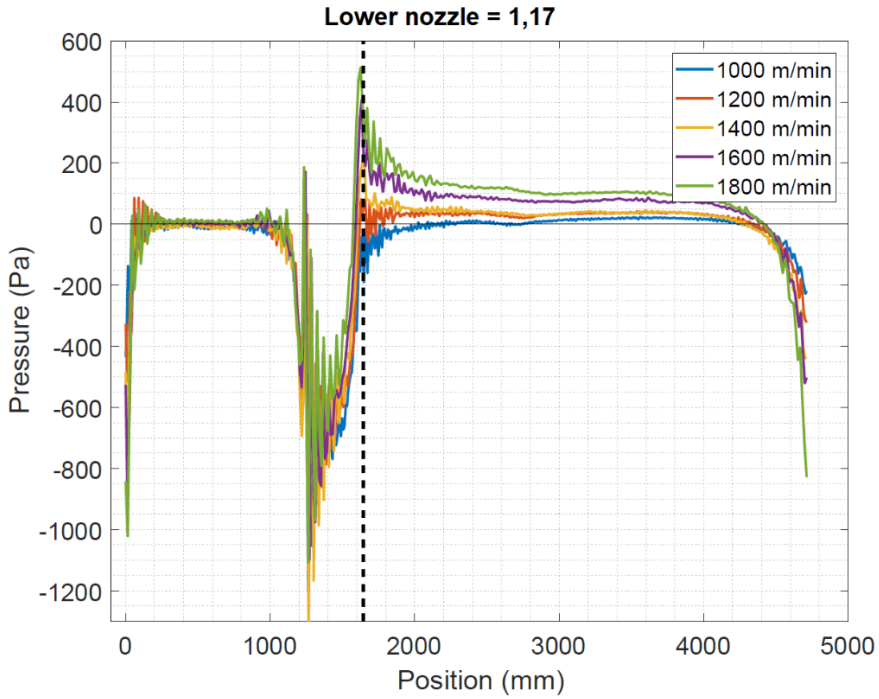

Figure 54 Edge area of the Concept D.

Compared to the results in Figure 53 the pressure, when the machine speed is 1000 m/min, rise to atmospheric pressure much earlier and the closing nip pressure is merely neutralised. This is because air will flow into the nip bringing the pressure to ambient pressure. For higher running speeds, the pressure peak is also larger at the edge, which might cause fluttering. Tension could be added to secure the web, but this is not possible at the beginning of the drying section, where the web is still weak. Additionally, the tension profile is not constant of over the cross-section, so the actual tension at the edge is much lower than with the average tension.

7.2.5. Concept E

The stabiliser in Concept E is the same as for Concept D, but the bottom roll has a surface structure which changes the behaviour of the concept. Firstly, the airflows from the nozzles are compared. Figure 55 present the results for a running speed of 1000 m/min. If the figure is compared to Figure 39, one can see that the groove behaviour is similar. The pressure along the perimeter is below ambient, which suggests airflow

between the nips. The effect of the stabiliser is key for the pressures developing in the closing nip. The pressure behaviour around the nozzle is similar to that of the former concepts; the pressure increases before the nozzle, due to airflows colliding into each other and as the sensor passes the nozzle, an under-pressure, develops as a result of the ejector effect. The static pressure rises due to the closing nip effect, but no over-pressure is formed, which is a desired feature of the concept.

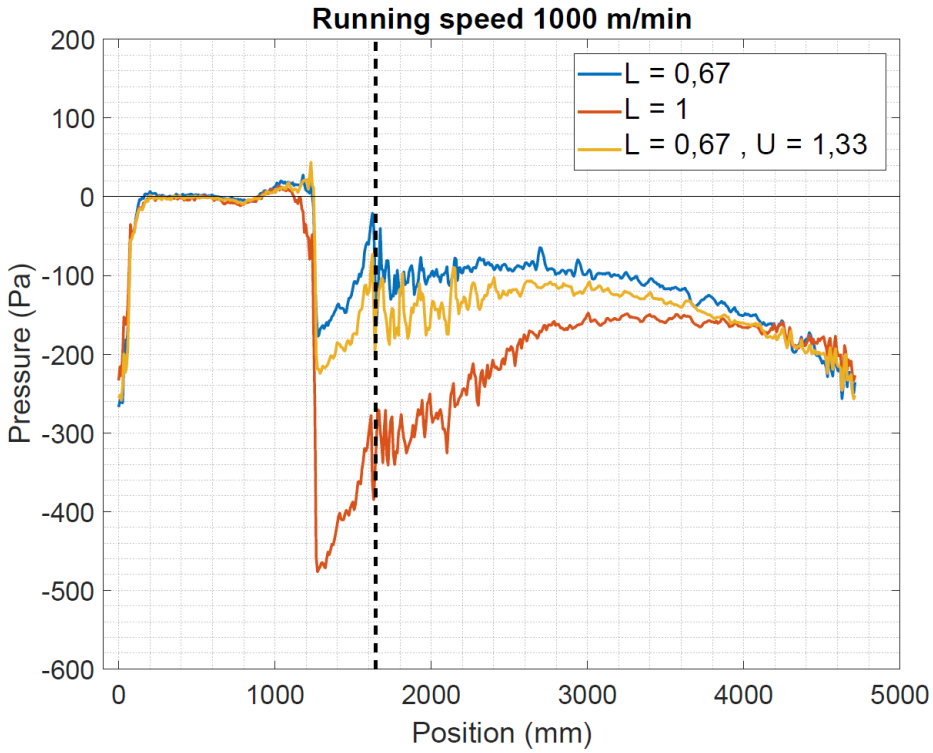

Figure 55 Concept E, at running speed 1000 m/min and various airflows.

Since there is an under-pressure over the perimeter, the difference between the ambient and the pressure in the groove will induce a force, which supports the web on the cylinder surface.

Naturally, as seen in the previous concepts, the harmful effects increase as the machine speed is increased, which is seen in Figure 56 for the lowest volumetric flow blown from the nozzle.

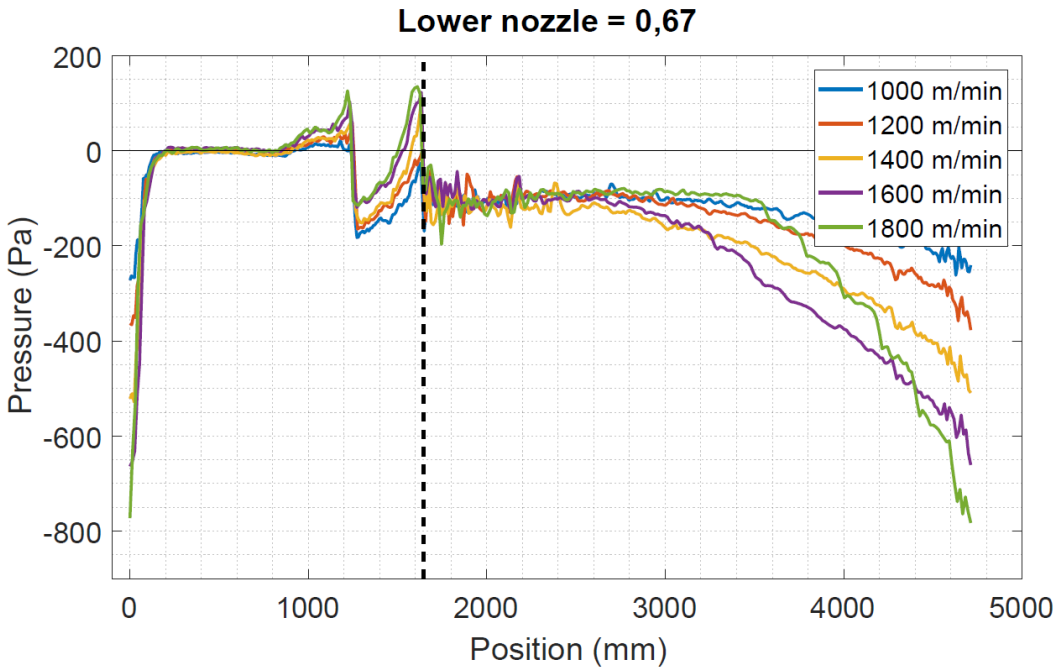

Figure 56 Concept E with lower volumetric flow from lower nozzle and varying velocities.

As machine speed increases, the over-pressures also rise. When the velocities rise over 1200 m/min, the airflow from the nozzle is no longer sufficient to compensate for the pressure in the wedge and an over-pressure is formed, which can cause undesired detachment and in worst case web break.

As in Figure 39, the pressure stays below ambient pressure, which is desired from a web stabilising point-of-view, since a support force is created by the pressure difference. If the forces in the ideal case are analysed, according to the force balance in Eq. 5, and the support pressure caused by the pressure difference is approximated to 90 Pa, the required tension for this geometry is shown in Figure 57.

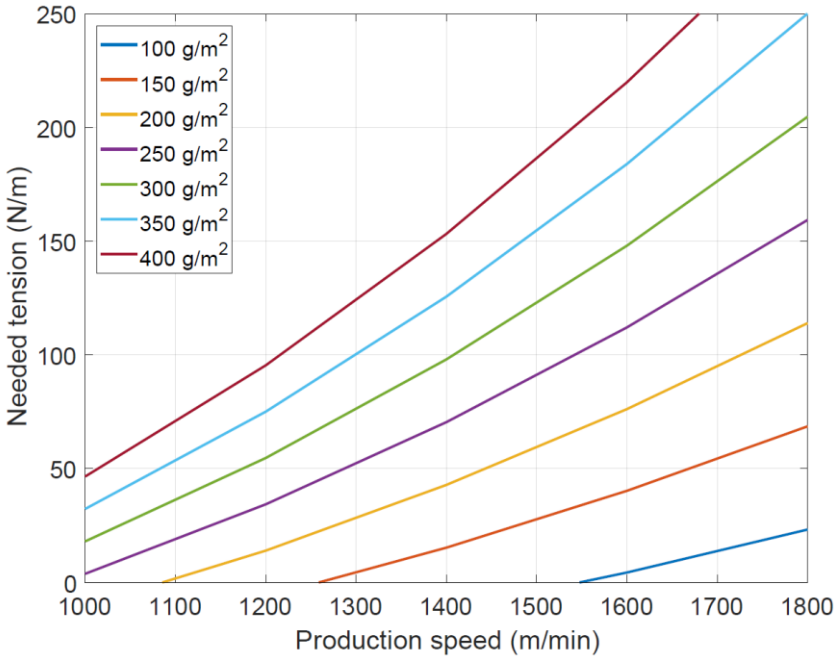

Figure 57 Tension required, at support pressure of 90 Pa at different machine speeds and grammages.

At velocities below 1200 m/min the closing nip pressure is below ambient pressure. Studying the same velocities in Figure 57, one can see that the needed tension is zero until the grammage increases over 160 g/m^2. This means that the pressure difference is able to support the web over the rotation without any added tension, which is particularly good for cylinder in the beginning of the drying section.

If the airflow from the nozzle is increased, even higher speeds can be allowed without risk of detachment. The static pressure profiles are compared for the velocities with the dimensioned volumetric airflow in Figure 58. The increase of 50 % in the volumetric flow decreases the peak pressure of the closing nip by almost 200 Pa, eliminating the over-pressure. Even the under-pressure after the closing nip is higher than for the previous case, and the decrease is caused by the accelerating air. However, the decrease of the static pressure appears to be fixed to the magnitude of the opening nip pressure and of course the running speed of the machine.

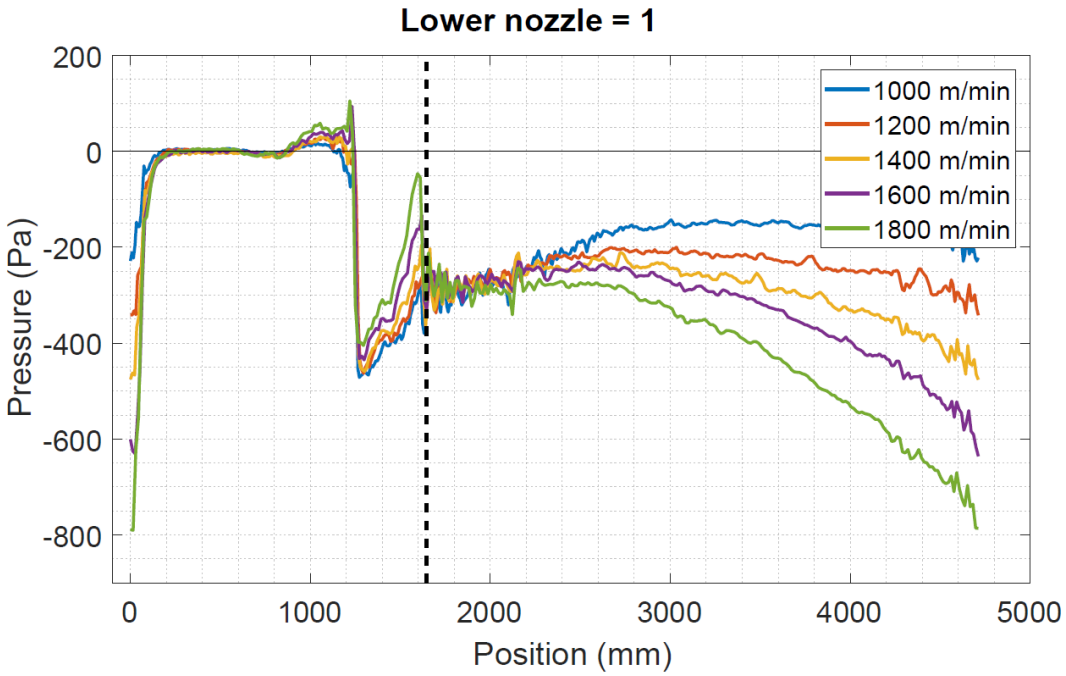

Figure 58 Concept E with the currently dimensioned volumetric airflow and various velocities.

The behaviour over the rotation differs compared with the earlier case of Figure 56; at the machine speed of 1000 m/min the opening nip pressure is higher than the closing nip pressure, which makes the shape the pressure profile parabola like. Interpreting these results by comparison with the findings of the simplified simulation model, one can conclude that there is flow towards the closing nip, which has a lower pressure. Furthermore, the parabola-shaped pressure profile suggests some communications between the grooves on the cylinder surface.

As for the required support forces, estimates by Eq. 5 are provided in Figure 59. The supporting pressure difference is taken from Figure 58.

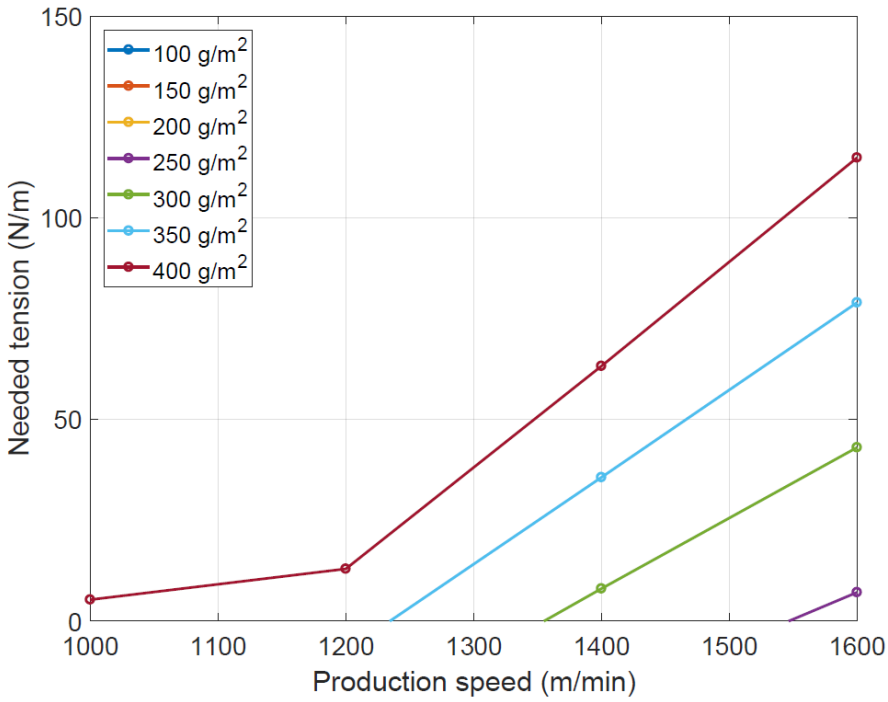

Figure 59 Needed tension for Concept D in the ideal case.

From the figure one can see that at low velocities even high grammage paper grades can be run without any added tension. As velocities and grammages increase, the required support increases, to finally become too high that the support from the pressure difference becomes insufficient.

Concept E seems to quite well support the web even at high velocities and is able to eliminate the closing nip effects. However, the limiting factor is normally the conditions in the edge area. The aerodynamic forces are also higher at the edge, which will require better support at the edge compared to the middle. The sensor output from the edge area Concept E is illustrated in Figure 60.

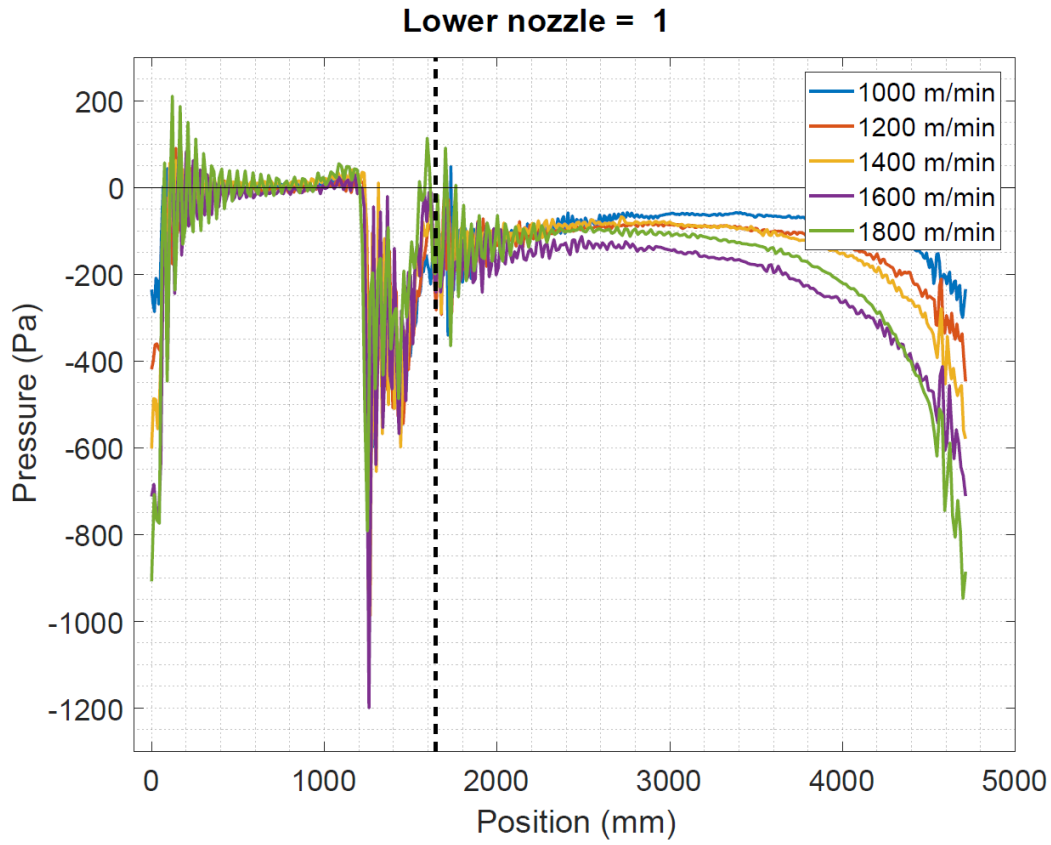

Figure 60 Edge area of Concept E with the currently dimensioned volumetric flow.

The under-pressure decreases substantially compared to the middle of the cylinder. One can clearly see that there is leakage from the surroundings to the groove. The model presented in Subsection 5.1.1 describes the situation. However, instead of the fabric and web being permeable, air leaks into the low-pressure groove. In Concepts A and B, the edge showed approximately same pressures as the middle area, since the vacuum hinders the crossflow of air into the grooves. The support force is clearly not high enough in this case to prevent flow into the groove. Also, the closing-nip pressures are higher at the edge compared to the middle, since air flows into the wedge area, from the surroundings, because of the under-pressure produced by the nozzle. This consequently produces a bigger mass flow towards the nip, which then has to decelerate, increasing the static pressure. The closing nip pressure peak is below ambient pressure until the machine speed increases over 1600 m/min, which is worse compared to the middle area. However, it is significantly better compared to the edge area of Concept D.

There is still an under-pressure over the rotation, which produces some support. For higher machine speed, the pressure difference is also higher. This is similar to the suction roll cases; due to the higher air velocity in the groove, the static pressure will decrease. The support provided by the pressure difference can enhance the stability. However, the ideal case in Eq. (5) probably describes the edge area quite poorly, since the web is disturbed by pressure forces from the surrounding. To give a idea of the harmful forces and the required compensation force, Figure 61 illustrates the tension needed for the pressure differences of Figure 60. The velocities are here in the range 1000-1600 m/min. The highest machine speed was left out since the closing nip pressure exceeded ambient pressure and smooth runnability cannot therefore be guaranteed.

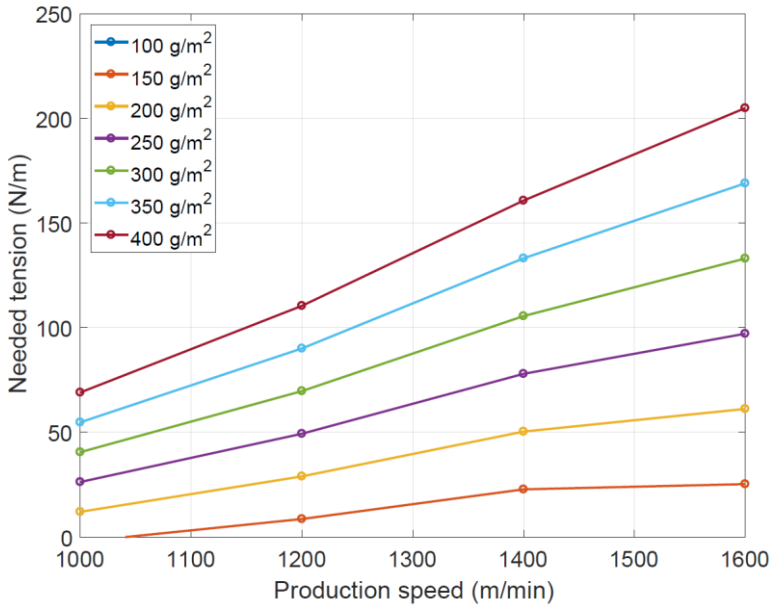

Figure 61 Ideal needed support at the edge area for Concept D.

The required tension is significantly higher than for the middle area and even at low machine speeds added support is needed when grammages increase. In analysing these results one should keep in mind the quite nd Of course, the model in Eq. (5). In real systems, there are supporting forces by the adhesion between the paper and fabric as well as interfibre bonds creating support to the web. On the other hand, the web is subjected to other lateral forces, which additionally could cause web flutter and other undesired movement.

8. Comparison

In the previous chapter the concepts were discussed merely based on the functionality and the phenomena occurring in the system. Here the aim is to compare the concepts in a certain environment. Key factors in the comparison are cost efficiency and energy consumption. The intent is to determine the concept that is appropriate and the most cost-effective solution for a certain production set-up.

Other important factors are the usability of the concept as well as the required production break needed to install the equipment.

8.1. Framework for the comparison

The comparison focuses on rebuilds of existing single run paper and board machines. Because the need for support varies in the drying section, the area inspected is the third dryer group. There, the tension of the web is small or negligible, which requires higher support from the surrounding surfaces. Additionally, the dry solids content is approximately 60%, which means that the paper is somewhat heavier compared to the finished product. The grammages of interest are presented in Table 4; paper grades within this grammage range are, among others, liner and fluting grades.

Table 4 Grammages in the comparison

Finished product (moisture 10%, g/m^2)	Wet product (dry contents 60%, g/m^2)
100	150
120	180
140	210
160	240
180	270
200	300

The grammages are used to analyse the forces over the rotation using Eq. 5. As the third group of cylinders is of interest, the tension factor in the equation was set to zero.

The appropriate closing nip pressure is determined to be below zero because the allowed pressure is unknown. Concepts A and B are known to work within the measuring interval, even though the closing nip shows over-pressures due to the support from the vacuum. The limitation to analyse only Concepts A and B is justified by the fact that for Concept C, D or E there are currently no reference machines.

8.2. Functionality of the concepts and energy consumption

The comparison begins by comparing the closing nip pressures, with results are presented in Figure 62. The black line indicates the ambient pressure and when the points are below the line, no over-pressure peak occurs.

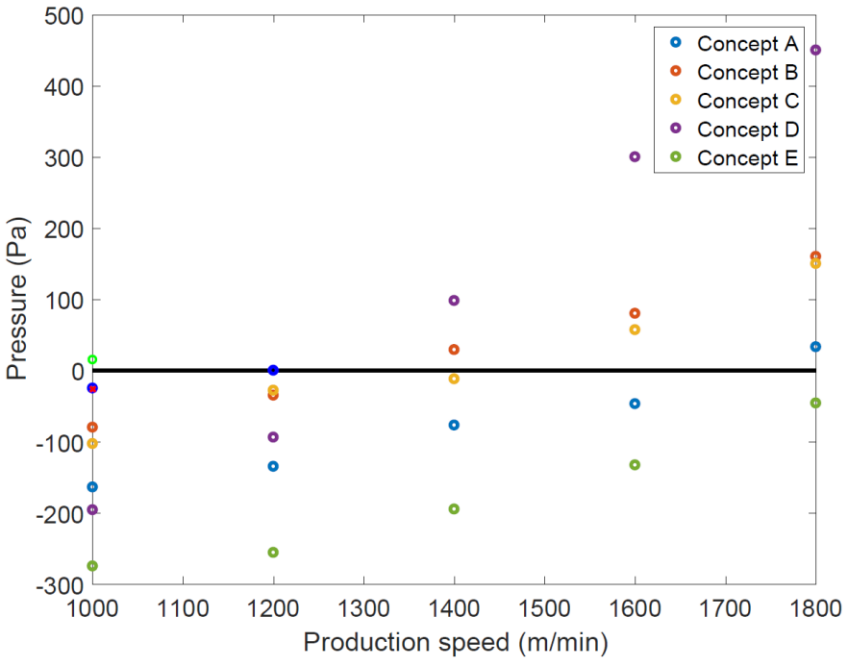

Figure 62 Closing nip pressures for the concepts.

The figure clearly illustrates the effect of the lower nozzle especially at lower velocities. Concepts A, D and E are equipped with the lower nozzle and as seen from

the figure the highest under-pressures occur for these concepts, especially at the lower velocities. This would suggest that a lower nozzle effectively reduces the peak pressures.

Because the pressures are very low for Concepts D and E, the quantity of air from the lower nozzle could be reduced at lower machine velocities. This would also reduce the energy consumption of the concepts. These operation points are seen in Figure 62 as bright blue points for Concept D and red point for Concept E.

The same analysis can be undertaken for the Concept C at the machine speed of 1000 m/min: By lowering the evacuation from the cylinder by 25% from the dimensioned value, the green operating point can be used. The point is somewhat over the ambient pressure, but then again, the under-pressure that follows is much greater than in Concepts A and B, which will support the web.

Next, the support over the rotation is studied using Eq. 5 and the grammages are introduced. As there was an over-pressure over the cylinder for Concept D, the equation will only give negative values for the operation points. The model is likely to overestimate the required support since it neither considers interfibre strength nor any frictional or adhesion effects, which might add support of the web. From references at real paper and board machines, it is known that the concepts with a smooth cylinder work. However, this particular concept is not currently in use, which is why the author cannot guarantee smooth runnability based only on the static pressure profile.

Figure 63 is drawn based on the grammages of liner and fluting grades at a consistency of 60 %. The points are taken from the drawn pressure profiles in Section 7.2, that produced an under-pressure in the closing nip.

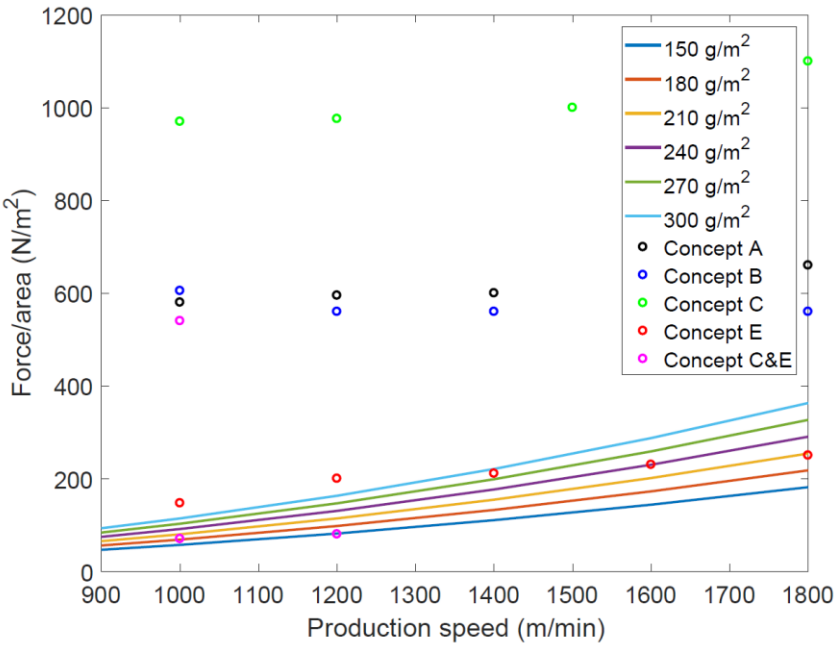

Figure 63 Support of the different concepts over the rotation.

As Kauppinen, 2018, and Pitkäniemi, 2000, suggested, the vacuum inside the suction rolls is enough to stabilise the web over the rotation and the dimensioned airflow is likely due to the closing nip effects (Pitkäniemi, 2000, p. 63). The same can be suggested by the values obtained within this thesis. Since the closing nip peak pressure is reduced, the amount of suction air used in the trails of the concepts seems excessive. By decreasing the vacuum and still ensuring the closing nip, the energy consumption of Concepts A and B could be significantly reduced. For Concept C, the reduction is not possible since it will still require the suction for the stabilising the nip. However, the volumetric airflow could be reduced for the lowest measured machine speed (1000 m/min) to 75 % of the current dimension value, as seen as the magenta-coloured point in Figure 63. The concept needs more support, but decreasing the suction would result in higher closing nip pressures. A decrease in the evacuated air flow will produce savings in the energy consumption.

The red dots in Figure 63 for Concept E are in the same magnitude as the results from Eq. (5), but the support becomes insufficient for some grammages as the machine speed increases. When the speed is low, the support along the perimeter is sufficient. By lowering the airflow from the nozzle, close to the closing nip, the operations points denoted by the two magenta points in the lower part of the figure, are obtained.

Summarising, the dimensioning value of the airflow from the nozzle should be such that the pressure falls between those of the red and magenta points. The downside of Concept E is the conditions in the edge area. From Figure 60 one can observe that the leakage into the groove will decrease the functionality of the concept.

The functionality of the concepts depends also on other factors. These are, for instance, tail threading and the maintenance need associated with the concepts. Tail threading affects many aspects of the comparison, since the investment varies between the concepts and whether the tail threading is with or without ropes will affect how easy the threading will be.

The maintenance need of the concepts depends on a variety of factors and they are different for each concept. For the stabilisers, the common factor affecting the functionality is the mechanical seals, which restrict the pressure areas. The seals are important for lowering the required airflow, thus lowering energy consumption. However, the seals are in contact with the moving surfaces, which can strain both the fabric and the seals. Additionally, the tension profile is non-uniform, which may cause uneven attrition, especially at the edges where the tension is lowest and bending is highest (Leimu, 2017). The rate in which the seals wear off is case specific and depends on the geometry and how the seals are installed, which is why it is hard to know how often the seals must be changed or how the life time of the fabric will change. Therefore, Concept A has an advantage compared to the other concepts, as it does not have any mechanical seals against the fabric or the cylinder.

Additionally, the active stabilisers and cylinders require cleaning of the nozzles and suction holes. As comprehensively discussed in Subsection 5.1.2, the holes of the suction rolls clog, when particles accumulate on the inner wall of the cylinder. Also, the nozzles of the blow boxes will lose their functionality when the nozzles are clogged. This is usually more common for the suction nozzles than for blow nozzles.

Table 5 summarises, the usability factors and based on this some conclusions can be made on, how much the concepts require maintenance.

Table 5 Summary of usability.

	Mechanical seals	Clogging of suction roll	Clogging of blow nozzles
Concept A		x	x
Concept B	x	x	x
Concept C	x	x	
Concept D	x		x
Concept E	x		x

Cost efficiency and energy consumption are becoming increasingly important. The power consumption is calculated according to Eq. (24), where merely a theoretical value is obtained as the comparison does not take a stand on the fan to be used. The pressure required to overcome the pressure losses is measured at the flange and the volumetric flows are dimensioned based on the framework for the functionality. The values are presented in Table 6 as relative values compared to the energy consumption of Concept A at 1000 m/min. The grey areas are the ones where the runnability cannot be guaranteed. As seen from the table, the concepts with evacuation from the cylinder have larger consumption as the machine speed increases and simply because the rotating motion of the cylinders create an increase in the pressure loss, which has to be compensated for by the fan (Kauppinen, 2018, p. 44).

Table 6 The relative energy consumption of the concepts.

	1000 m/min	1200 m/min	1400 m/min	1600 m/min	1800 m/min
A	100.0 %	102.1 %	106.4 %	110.6 %	117.0 %
B	72.3 %	72.3 %	78.7 %	83.0 %	87.2 %
C	34.0 %	80.9 %	87.2 % (1500 m/min)	93.6 % (1700 m/min)	97.9 %
D	131.9 %	206.4 %			
E	38.3 %	38.3 %	131.9 %	131.9 %	131.9 %

The highest consumption is for the Concept E, largely due to the large volumetric airflow needed, to stabilise the closing nip. The second largest consumption is for Concept A and this depends on the high evacuation of the suction roll and the usage of both upper and lower nozzle. The lowest energy consumption depend on the

production speed of the machine; for lower velocities in the range of 1000-1200 m/min Concept C appears to be the most appropriate solution, but the concept has some restrictions on the kind of paper that can be run with the lower airflow. When velocities are over 1400 m/min, the suction roll concepts become the most effective solutions from an energy consumption point-of-view.

8.3. Case specific investment cost and energy consumption

Throughout the thesis, the focus has been on the importance of cost-effective solution for runnability and, therefore, the investment needed for the concept is central in evaluating the concepts. Because each paper and board machine has its own requirements, a framework is made for the investment costs. First and foremost, the investment cost considered is for the rebuild of an old machine, i.e., on-site work is required. The investment includes the complete concept for 12 positions for a nine metres wide machine. The investment does not include any geometry changes, so the machine is already taken to be of slalom construction. The investment includes the cost of the stabilisers and the needed fans for the stabiliser and suction rolls as well as the on-site work.

The relative investment and shutdown time required presented in Figure 64. The values are related to Concept A, because the concept is accepted widely as the best solution for high speed paper machines. It is apparent that the concepts using a suction roll, all have the largest investment cost. This is likely due to the modifications made on-site on the bottom cylinder as well as the need of separate fans and ductwork. The lowest cost is for the smooth roll concept, Concept D, which does not require modifications on the bottom roll. Concept D is approximately requires half of the investment of Concept A and the grooved roll concept, Concept E, is roughly 25% cheaper than the suction roll concepts. The same trend can be seen in the required shutdown time for the installation of the equipment.

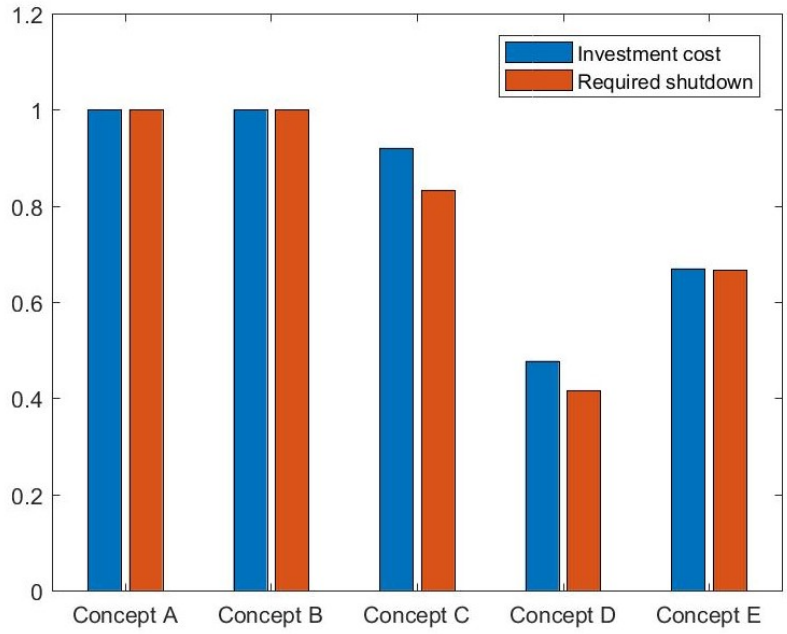

Figure 64 Relative investment costs and required shutdown time for installation.

The required shutdown time for the rebuild will affect the production rate of the machine and with higher shutdown time, the latency will increase, so it is commonly desired to reduce the needed shutdown time. For the suction roll concepts, most time is required by the grooved suction roll, which requires 20 % more time compared with the perforated roll, which further seems logical since the cylinder is grooved and perforated.

When the energy consumption for this case is considered, the results in Figure 65 are obtained. The values are calculated from Table 6 and multiplied by the width of the machine and the amount of positions. Since all mills have different expenses for electricity and different production hours, the electricity price is assumed to be 8 c/kWh and the annual production hours are 6800.

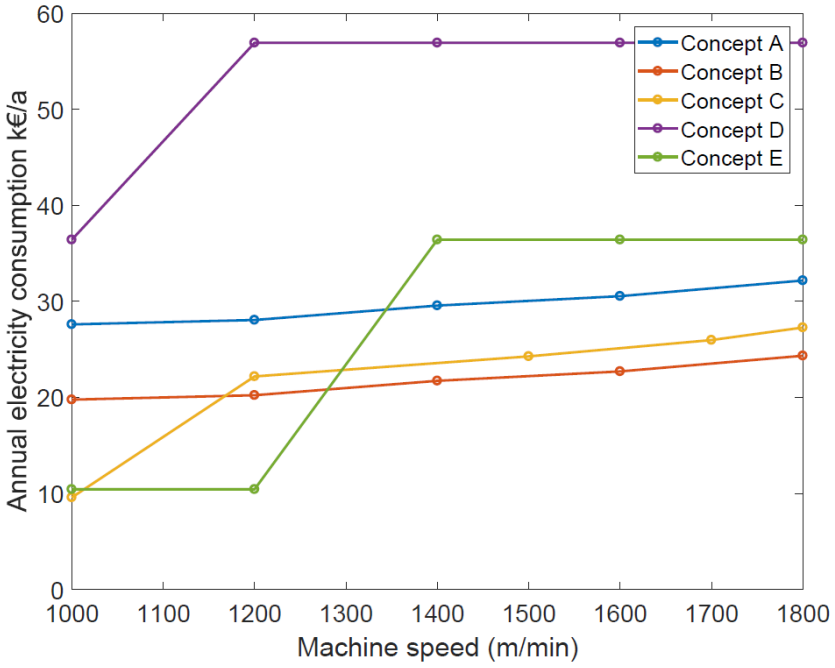

Figure 65 Annual electricity cost for the concepts at different machine speeds.

Combining the investment costs with the operational costs, keeping in mind the functionality of the concepts discussed in Section 8.2, it seems that the suction roll concepts are too robust and cost intensive for low machine speeds. For lower speeds Concepts C, D and E seem viable. The functionality of Concept D is questionable in the beginning of the drying section, but it could be a good solution for the groups with higher consistency. Concept C, on the other hand, has lower investment costs compare to the other suction roll solutions, but the investment cost was higher compared to Concepts D and E. As the machine velocities increase the volumetric flow for the concepts must increase to stabilise the nip effects and other harmful effects, which increases the electricity consumption. Therefore, at higher machine velocities the more robust concepts could be the plausible option, since they are able to better secure the web with lower consumption. Based on the trials and calculations made the limit lies around 1400 m/min.

9. Discussion and conclusions

As seen from the analysis made in the previous chapter, all the concepts have advantages and disadvantages, so it culminates to what the requirements are for the runnability. The key variables, which have arisen during the trials, are the production speed, the paper quality factors and the strategies for eliminating the harmful effects.

The pressure development in the nip areas can be clearly seen in all the concepts and the dependence on machine speed is evident. Assessing the bottom cylinders, the grooved options consistently have lower closing nip pressures compared with the other options, which would suggest that utilising the naturally occurring pressures of the closing and opening nip as a driving force is beneficial. The highest pressure peaks were created with the smooth cylinder and the lowest with the grooved suction roll. The grooved suction roll requires evacuation from the roll in order to work. However, it is interesting that the effect of the groove seemed to be more central compared to the amount of suction. In Figure 39 and Figure 41, the pressure in the closing nip is in the same order of magnitude for both the grooved suction roll and merely the grooved roll. The suction of the cylinder could be made more efficient by isolating the pocket, like in the perforated roll case; use in Figure 41 the whole pocket was not isolated, which allowed air to leak into the pocket reducing the under-pressure created. Additionally, between the two grooved suction roll concepts, the one without a lower nozzle, Concept B, benefitted more of the increase in the volumetric flow of the suction roll, than Concept A with the lower nozzle. This suggests that the doctor blade is beneficial in the grooved suction roll case and that the lower nozzle in Concept A is the decisive factor of the closing nip over-pressure.

The closing nip is also controlled by the lower blow box nozzle, which created the under-pressures in the closing nip reducing the peak formation. Comparing the concepts at the closing nip, the ones with the lower nozzle are able to reduce the closing nip positive peak more efficiently, especially when the machine velocities were below 1400 m/min. This would suggest that having a nozzle targeting the closing nip is beneficial compared to the concepts only relying on suction of the cylinder.

Over the rotation, the suction rolls were able create a high pressure difference over the web, which secures the web on the surface. However, the dimensioned evacuation is

relatively high when the ideal case for the detaching forces is analysed. The dimensioned values are likely so high, because the suction rolls are designed to independently stabilise the closing nip, which is why a higher evacuation is required. However, the doctor blade and the lower nozzle in Concepts A and B reduced the peak formation, so that no pressure peak occurs, which would suggest that the suction is still over dimensioned. As the machine velocities increase, the dimensioning becomes more appropriate, since the closing nip pressures increase as well as the need for support.

The Concept D, with the smooth roll, could not be compared with the same methodology as the other concepts, since the pressure was greater or equal to the atmospheric pressure, which would then suggest that Concept D cannot be used without any additional support, such as more tension. However, this seems unlikely as reference machines use the smooth roll without any additional stabilising. This implies that the equation used for the equilibrium may be too approximate, as it does not consider the interfibre bonds and the strength properties of wet paper. Anyway, merely based on the static pressure, the runnability of Concept D cannot be guaranteed, especially in the beginning of the drying section.

The concept best fitted for the grammage range chosen was Concept E, the grooved roll with the stabiliser, which can reduce the closing nip over-pressure and based on the model used for the forces over the perimeter, the support was sufficient for the grammage range chosen.

The problem with Concept E is the edge area of the paper. As seen in Figure 40, even the middle part had some leakages to the other grooves, and for the edge area the leakage is significantly higher. This means the same kind of under-pressures, which could secure the web on the surface, do not exist. And as the velocities become higher the disturbing effects of the edge can cause web breaks.

As discussed, the edge differs from the middle both with respect to quality, the support and aerodynamic forces. Among other factors the tension of the web is non-uniform and the friction between the fabric and the paper is lower at the edge, which reduces the support provided to the edge. If the edge area of active cylinder concepts is compared to the middle part, the edge has almost the same vacuum levels as the middle

part of the roll, which would suggest there is less leakage into the grooves from the ambient air. This is because normally the paper web is narrower than the perforated area of the cylinder, which means at the edge of the cylinder before the web edge, the suction of the cylinder hinder the crossflow towards the middle by evacuating the air. Hence, when comparing the edge area, the suction roll is able to control it in the best manner.

The best choice of concept is clearly dependent on the production speed and the product produced. Based on the comparison in Chapter 8, Concept E has the most appropriate investment and operational costs combined with functionality for low machine speeds. Concept D may be a good option when the tension can be added, i.e., closer to the dry end of the drying section and the velocities are low below 1300 m/min.

When machine speed increases over 1400 m/min, the power consumption of Concept E rises and an over-pressure is formed at the closing nip for Concept D , so these two concepts may not be feasible anymore. Therefore, at higher machine speeds, the suction roll concepts seems most feasible. By further optimising the functionality of these concepts to the needed support, they could further save operational costs.

9.1. Further research prospects

Most of the analysis made in this thesis is based on qualitative arguments, studying variables that affect the closing nip pressure peaks as well as the phenomena in the grooves and over the perimeter. Therefore, in making a comparison, the author had to make gross estimates of the conditions characterisin good runnability. Additionally, some other targets could be optimised in the future.

The closing nip behaviour has been well studied in earilier work, but studies on the actual consequences of the high pressure peak are limited. The FSI model developed by Immonen et.al., 2009, modelled the transverse displacement of the web in the nip regions and the authors claimed, that their study was first of its kind. Thus, there could be a potential to further develop the model, since the computational tools have improved and computer capacity has grown. Simulation by such models could give

indications on the pressure levels causing transverse displacement of the web that increases the risk for web break.

Other matters which could benefit from further investigation are the optimisation of the concepts for saving energy and efficiently eliminate the harmful effects. Based on the results, the suction roll concepts were found over-dimensioned, largely due to the need of stabilisation in closing nip. Therefore, it could be interesting to determine how to stabilise the closing nip as well as how to benefit from the vacuum created by the suction roll. At low velocities, Concept E seemed to have the lowest cost and produce the most appropriate runnability, but the pressure profile at the edge area differ from the middle of the web, due to the leakage from the surroundings. The same problems are seen for the smooth roll concept, Concept D. To secure the web and enable higher velocities, the concept could be further developed to stabilise the closing nip. This could be done by either optimising the blow box nozzle to reduce the inlet pressure of the groove, so that the energy consumption does not increase, or making the cylinder a partial suction roll to secure the edge area. The stabilisers could also be modified to target the edge area and reduce the leakage.

Perforating the grooved roll will on the other hand increase the investment cost of the equipment due to the need of separate ductwork and fans as well as since the on-site modification time will increase costs. Therefore, one could study the optimal geometry and dimensions for the groove and the holes and how the on-site work could be reduced.

As the present comparison of concepts was made based on rebuild and upgrades of existing machines, a similar study on new machine deliveries could be made. The cost of producing the concepts is likely to be lower for new machine deliveries, but, on the other hand, the Concept E could be used at the dry end and thereby could produce savings in manufacturing.

Additionally, this thesis disregarded thermodynamic effects on runnability, which in practise are improtant since the drying section is a humid and warm environment and the properties of humid air at 80°C differs from those of dry air at 20°C. Also, the effect of the drying fabric on the closing nip pressure peak was neglected in the trials, which is why it would be interesting to inspect the differences of the existing fabrics

and study how the fabric could be modified to reduce the harmful forces, whilst still providing the needed drying properties.

Another factor which was completely excluded was the tail threading of the concepts and its effect on the investment cost. The efficiency of the tail threading is important, when considering the latency and the production rates, which is why this area could benefit from further studies and comparisons.

Svensk sammanfattning - Swedish Summary

En experimentell jämförelse av slalomkonsept

Under senaste årtiondet har pappersindustrin genomgått betydliga ändringar. Till följd av bl.a. digitaliseringen har konsumtionen av olika slag av tryckpapper minskat. Detta har lett till nerkörning av produktionsanläggningar eller ombyggnad av hela pappersmaskiner. Digitaliseringen har medfört även andra förändringar: Tillväxten av näthandel har ökat behovet av förpackningsmaterial, vilket har lett till en 20 % ökning i den finländska produktionen av kartong (Lukkari, 2018). Detta har inneburit att flera kartongmaskiner fordrat kapacitetsökning för att tillfredsställa behovet på marknaden. Kapacitetsökningen möjliggörs vanligtvis antingen genom omformning av maskinlinjen eller genom att öka produktionshastigheten, där det senare är det vanligare alternativet. Flaskhalsen i ökningen av produktionshastighet är vanligtvis körbarheten och pappersbanans hantering.

Körbarhet hos en pappers- eller kartongmaskin bestäms av hur väl banan förs genom maskinen, utan att den utsätts för överdriven belastning. Körbarheten kan kontrolleras med olika körbarhetskomponenter, som t.ex. sugvalsar eller stabilisatorer. Målet med körbarhetskomponenterna är att neutralisera de krafter som bidrar till oönskad rörelse av banan. Den största delen av körbarhetskomponenterna utvecklades vid slutet av 1900-talet och produktionshastigheter upp till 2000 m/min kunde nås. Nu ligger focus på kostnadseffektivitet och minimering av energiförbrukningen (Siverä, 2017).

I detta diplomarbete undersöks de fenomen som förknippas med hastighetsökning av pappers- och kartongmaskiner med slalom konstruktion. En inblick ges även i vilka faktorer som påverkar pappersmaskinens körbarhet. Inom ramen av arbetet utfördes experiment på fem olika körbarhetskoncept i pilotskala och deras funktionalitet studerades samt jämfördes.

Verkande krafter och körbarhetskoncept för slalom konstruktion

Målet med körbarhetskomponenter är att motverka de krafter som pappersbanan utsätts för. Dessa krafter kan härstamma från pappret eller förorsakas av den yttre omgivningen. Då krafterna blir starka kan de inverka på stabiliteten hos banan samt papprets kvalitetsegenskaper.

På grund av geometrin hos torkpartiet med slalom konstruktion bildas det lokala över- och undertryck vid ingående samt utgående nyp. Dessa bildas genom luftens rörelse i gränsskikten, som uppstår vid de rörliga ytorna, som t.ex. cylindrarna och torkviran. Då pappersbanan och torkviran rör sig mot den lägre cylindern, kommer luft att transporteras i gränsskiktet mot det ingående nypet. Detta leder till att luften pressas in i det smala nypet och tvingas retardera, vilket orsakar en ökning i det statiska trycket. Den snabba tryckökningen kan orsaka en kraft i torkvirans och papprets riktning, som kan förorsaka böjning av viran och pappret eller i värsta fall lösgöra pappret från torkvirans yta, vilket kan orsaka banbrott. Diverse faktorer kommer att inverka på storleken av trycket, såsom t.ex. torkvirans aerodynamiska egenskaper, geometrin hos det ingående nypet och naturligtvis maskinhastigheten. Ytterligare kommer andra krafter att bidra till pappersbanans stabilitet vid det ingående nypet. Adhesions- och friktionskrafter mellan viran och pappret stabiliserar banan, medan centrifugalkraften driver banan utåt. Centrifugalkraften är central även under rotationen över den lägre cylindern. För det ideala fallet då aerodynamiska krafterna försummas, kommer de verkande krafterna att vara summan av centrifugal krafterna samt gravitationen. Dessa krafter kan bilda luftblåsor mellan banan och stödytorna.

Körbarhetskoncepten baserar sig vanligen på att bilda en tryckskillnad över viran och banan som är riktad i motsatt håll i förhållande till de skadliga krafterna. Koncepten kan vara antingen sugvalsar i kombination med aktiva eller passiva stabilisatorer eller enbart aktiva stabilisatorer med passiva botten cylindrar. Funktionsprincipen för sugvalsarna är att bilda ett undertryck mellan banan och cylindern som fäster banan på valsytan. Valsens yta kan vara enbart perforerad eller kan ha en ytstruktur, vars uppgift är att stabilisera tryckskillnaden mellan det ingående och utgående nypet. Användningen av sugvalsar möjliggör höga hastigheter och kombinerat med

stabilisatorer kan hastigheterna ökas ytterligare. De passiva stabilisatorerna måste vanligen kombineras med sugvalsar, eftersom de enbart isolerar volymen som bör evakueras. Stabilisatorn har vanligen isolerande tätningar mot stödytorna. Användning av passiva stabilisatorer möjliggör minskning av volymflödet evakuerad luft från sugvalsen och därmed reduceras energibehovet. Sugvalsarna kan kombineras även med aktiva stabilisatorer, som eliminerar lokala tryckpikar. De aktiva stabilisatorerna bildar ett lokalt undertryck genom att antingen evakuera luft lokalt eller blåsa luft och skapa en ejektor effekt som bildar ett lokalt undertryck. De aktiva stabilisatorerna kan även kombineras med passiva cylindrar som antingen är släta eller har någon typ av ytstruktur.

Experiment

För att kunna identifiera problemen i slalom konstruktionen samt objektivt jämföra olika koncept sinsemellan, utfördes experiment i pilotskala vid försöksanläggningen hos Valmet i Reso. Fem olika koncept testades med samma konfigurationer, där diametern av cylindern samt maskinens geometri hölls lika. Torkviran var den samma och ytan var tejpad med maskeringstejp så permeabiliteten och ytans skrovlighet var lika för alla koncept. Under mätningen testades olika maskinhastigheter med varierande volymflöde från de aktiva komponenterna och de statiska trycken uppmättes vid cylinderytan av piezoresistiva trycksensorer och genom punktmätningar av det statiska trycket vid det öppna draget gjordes. Koncepten som testades var följande:

Koncept A:

- Cylinder: Sugvals med ytstruktur och med öppen yta som representerar ungefär 0,4 % av den totala ytan.
- Stabilisator: Blåslåda med munstycke vid utgående nyp hos den övre cylindern samt munstycke vid ingående nyp hos den lägre cylindern. Inga tätningar.

Koncept B:

- Cylinder: Sugvals med ytstruktur och med öppen yta som representerar ungefär 0,4 % av den totala ytan.
- Stabilisator: Blåslåda med munstycke vid utgående nyp hos den övre cylindern samt en justerbar tätning mot cylinderytan.

Koncept C:

- Cylinder: Slät sugvals och med öppen yta som representerar ungefär 0,4 % av den totala ytan.
- Stabilisator: En passiv stabilisator som isolerar hela fickan med tätningar vid övre cylindrarna.

Koncept D:

- Cylinder: Passiv slät cylinder.
- Stabilisator: Blåslåda med munstycke vid utgående nyp hos övre cylinder samt munstycke vid ingående nyp hos den lägre cylindern. Bägge munstyckena har isolerande teflontätningar.

Koncept E:

- Cylinder: Passiv cylinder med ytstruktur.
- Stabilisator: Blåslåda med munstycke vid utgående nyp hos övre cylindern samt munstycke vid ingående nyp hos den lägre cylindern. Bägge munstyckena har isolerande teflontätningar.

Resultaten från experimenten

Resultaten studeras genom att först identifiera de fenomen som kan inverka på körbarheten. Detta görs genom att betrakta valsarna och deras funktionsprinciper. Ur resultaten kan tydligt ses, att det ingående nypets övertryck stiger med ökad maskinhastighet. Hastigheten inverkar alltså på luftens hastighet i gränsskiktet, vilket påverkar hur mycket luften måste retardera då den närmar sig det ingående nypet. De högsta tryckpikarna kan observeras för slät cylinder, där gränsskiktets omfattning inte

minskar genom evakuering av luft eller genom förekomsten av skåror. Den lokala tryckökningen kan reduceras väl med den skårade cylindern, då luften från gränsskiktet kan röra sig in i skåran istället för att retardera och flöda tillbaka utåt. Dessutom utnyttjar skåran det faktumet att det ingående och det utgående nypet kommunicerar genom skårorna och luften naturligt strömmar från det ingående till det utgående nypet. Dessutom bildas ett undertryck i skårorna, vilket anses vara bra med tanke på körbarheten över valsytan.

En ideal modell gjordes för att kvantifiera magnituden av de krafter som verkar över rotationen. På basen av resultat av modellen samt experimenten kan man med belägg påstå att sugvalsarnas volymflöde är överdimensionerat i förhållande till de verkande krafterna. Dimensioneringen är antagligen vald för att kunna stabilisera det ingående nypet.

Då koncepten kombinerade med stabilisatorerna betraktades kan man iaktta att det nedre munstycket vid närheten av det ingående nypet minskar det statiska trycket väl, så att trycket i nypet ligger under omgivningens tryck; inga positiva tryckpikar förekommer således. Ett annat sätt att minska övertrycket som bildas i nypet är att isolera nypet och genom suget från valsen bilda ett undertryck kring området kring nypet.

Eftersom körbarhet är en egenskap som beror av omgivande krafter och deras storlek samt papprets egna egenskaper, så är det svårt att fastställa randvillkoren för god körbarhet. I litteraturen behandlas utförligt vilka krafter som bidrar till banans stabilitet, men fenomenen kvantifieras sällan och simuleringsmodeller som uppställts blir ofta krångliga och kräver värden för ett stort antal okända parametrar. Därför antas i detta arbete att bra körbarhet kan garanteras då övertrycket i det ingående nypet är lågt samt stödet över rotationen är tillräcklig för att motverka centrifugal samt gravitationskrafterna.

Ekonomisk jämförelse samt slutsatser

En ekonomisk jämförelse görs genom att beakta ett specifikt fall för ombyggnad av en befintlig pappersmaskin.

Jämförelsen visar att koncepten med sugvalsar har förhållandevis höga investeringskostnader när de jämförs med de övriga koncepten. Dessutom är produktionsstoppet för installationen av maskineriet för sugvalsarna längre än för de övriga koncepten. Investeringskostnader och produktionsstoppets längd är störst för koncepten med sugvalsarna, eftersom de valsarna kräver separata fläktar och rörledningar. Dessutom måste modifieringsarbete utföras på plats, vilket kräver mer tid och leder till högre kostnader. Därför är konceptet med enbart slät cylinder förmånligast.

Då elektricitetsförbrukningen beräknas för koncepten, visar sig konceptet med den släta cylinder vara det mest oförmånliga alternativet. Den höga energiförbrukningen beror av det stora volymflödet luft som behövs för att stabilisera nypet. Energieffektiviteten är dessutom beroende på den rådande maskinhastigheten. För lägre hastigheter är den passiva cylindern med ytstruktur den mest energieffektiva, medan för höga hastigheter är konceptet med sugvalsar det mest energieffektiva valet.

Sammanfattningsvis kan sägas att sugvalsarna är tydligt överdimensionerade vid låga hastigheter, speciellt då det lägre munstycket stabiliserar övertrycket i nypet. Det lägre munstycket var effektiv för stabiliseringen av övertrycket i nypet, men vid höga hastigheter uppstod ett övertryck i nypet. Enligt de resultat som erhölls är den passiva cylindern med ytstruktur i kombination med den aktiva stabilisatorn det bästa valet för låga hastigheter (<1400 m/min) och för högre hastigheter blir koncepten med sugvalsarna det bättre alternativet, tack vare deras funktionalitet samt energiförbrukning.

Framtida undersökningar kunde betrakta pappersbanans kanter, för att utreda hur körbarheten kunde effektiveras vid det mest kritiska området. Modellering och simulering av banas rörelse i geometrin kunde också utföras. Ytterligare kunde dimensioneringen justeras för att kunna öka kostnadseffektiviteten hos koncepten.

References

Agilent Technologies, 2009. *Agilen InfiniiVision 5000/6000/7000 Series Oscilloscope; Users Guide.* 1st ed. Colorado Springs: Agilent Technologies, Inc..

Carlsson, J., 1990. Arkfladder - boven avslöjas. *Svensk Papperstidning,* Issue 14, pp. 44-46.

Draper, N. R. & Smith, H., 1998. *Applied Regression Analysis.* 3 ed. s.l.:John Wiley & Sons Inc..

Fagervik, K., 2009. *Processindustriell mätteknik.* Turku: Åbo Akademi University, Technical Faculty.

Hauser, L., 1991. Analyse von Laufproblemen in der Papiermachine und moderne Konzeptionen der Papiertrockung. *Wochenblatt für Papierfabrikation,* 119(11/12), pp. 433-434, 436, 438, 440-441.

Heikkilä, P. et al., 2010. Multicylinder dryer and drying concepts. In: M. Karlsson, ed. *Papermaking Science and Technology; Papermaking Part 2, Drying.* Helsinki: Paper Engineers' Association/Paperi ja Puu Oy, pp. 80-125.

Honeywell Process Solutions, 2012. *Technical Notes,* Fort Washington: Honeywell International Inc..

Häggblom-Ahnger, U. & Komulainen, P., 2005. *Kemiallinen metsäteollisuus II, Paperin ja kartongin valmistus.* 3rd ed. Jyväskylä: Opetushallitus.

Häggblom, K.-E., 2015. *Reglerteknik I: Grundkurs.* Turku: Åbo Akademi University: Process Control Laboratory.

Immonen, E. et al., 2009. *A 2D FSI Model for Small Deflections of Fast Paper Webs Moving in Geometries Containing Nips and Boundaries.* Kuopio, Papermaking Research Symposium.

Juppi, K., 2001. *Experimental and Theoretical Study of the Effect of a new Dryer Construction on Paper Machine Runnability.* Doctoral Thesis. Espoo: Helsinki University of Technology.

Karlsson, J., 1989. *Teoretisk undersökning av Torkvirans Inverkan på Arkfladder i en Pappersmaskin.* Masters' thesis. Göteborg: Chalmers Tekniska Högskola.

Karlsson, M. & Paltakari, J., 2010. Introduction to paper drying and its principles. In: M. Karlsson, ed. *Papermaking Science and Technology.* Helsinki: Paper Engineers' Association/Paperi ja Puu Oy, pp. 14-38.

Kauppinen, K., 2018. *Paperikoneen Kuivatusosan Uusi Imutela.* Master's Thesis ed. Oulu: Oulun Yliopisto.

Krabbe, K., 2017. Paperia tarvitaan yhä. *Paperi ja Puu*, 6 June.

Kulite - Semiconductor Products, Inc., 2018. *Product Advisor.* [Online]
Available at: https://www.kulite.com/products/product-catalog/high-temperature-miniature-pressure-transducer-xce-093-xce-093/
[Accessed 20 6 2018].

Kulmala, M., 2012. *Airi - Ajettavuussimulaattorin Mittausjärjestelmän Modifiointi.* Bachelors Thesis. Turku: Turku University of Applied Sciences, Koneautomaatiotekniikka.

Kurki, M., Martikainen, P., Saarikivi, P. & Salminen, K., 2010. Web handling. In: M. Karlsson, ed. *Papermaking Science and Technology; Papermaking Part 2, Drying.* Helsinki: Paper Engineers' Association/Paperi ja Puu Oy, pp. 486-541.

Lang, I., 2004. Drying performance and fabric tension: Mill trials. *Pulp and Paper Canada,* III(105:11), pp. 47-50.

Leimu, J., 2008. *Theoretical and experimental investigation of the cylinder dryer opening nip.* Doctoral thesis. Turku: Åbo Akademi University.

Leimu, J., 2017. Why the seals wear in the cylinder dryer runnablility systems. *Paper Technology International,* 58(1), pp. 14-17.

Lukkari, J., 2018. Paperin tuotanto enää puolet huippuvuosista - kartonki ja sellu nousussa. *Tekniikka ja talous*, 26 March.

McGregor, C. & Knight, P., 1996. Utilizing process chemicals to improve water removal. *Paper Technology,* 37(8), pp. 31-37.

Metsäteollisuus ry, 2018. *Massa- ja paperiteollisuus.* [Online]
Available at: https://www.metsateollisuus.fi/tilastot/massa-ja-paperiteollisuus/
[Accessed 8 8 2018].

Miulus, T., 2010. *Measuring System Development and Virtual Instrumentation.* Bachelor thesis ed. Turku: Turku University of Applied Sciences.

Muhonen K., 2018. RE: Ilmanvirtaus viiran läpi [E-mail]. Recipient: Ella Pirttikangas. Sent: 4.6.2018 1:06 pm (GMT +0200), Valmet Technologies Oy, Raisio.

Neuendorf, R. & Wygnanski, I., 1999. On a turbulent wall jet flowing over a circular cylinder. *Journal of Fluid Mechanics,* Volume 381, pp. 1-25.

Nurmi, S. A., 2009. *Computational and Experimental Investigation of the Grooved Roll in Paper Machine Environment.* Doctoral thesis. Lappeenranta: Lappeenrannan teknillinen yliopisto.

Paavolainen, J., 2015. *Valmet Clothing days 2015; New dryer fabric designs to improve efficiency.* s.l., Valmet Technologies Inc..

Pakarinen, P., Kiiskinen, H., Kekko, P. & Paltakari, J., 2009. Drying and paper quality. In: M. Karlsson, ed. *Papermaking Science and Technology; Papermaking Part 2, Drying.* Helsinki: Paper Engineers' Assocciation/Paperi ja Puu Oy, pp. 239-285.

Pikulik, I. & Poirier, N., 2003. New Development in Paper and Board Drying. *WPP,* pp. 56-64.

Pitkäniemi, T., 2000. *Paperikoneen Kuivatusosan Imutelan Virtaukset.* Masters Thesis ed. Turku: Tampereen teknillinen Korkeakoulu; Konetekniikan osasto.

Sikanen, J., 1998. *Paperikoneen Ajettavuusjärjestelmän Mitoituksen Optimointi Radanhallinnan ja Energiakulutuksen Kannalta.* Masters thesis ed. Turku: Lappeenrannan Teknillinen Korkeakoulu.

Siverä, I., 2017. Valmetin tehdas tykittää kartonkikoneita ennätystahtia - Kiinalaiset ostavat jopa kokonaisia valmistuslinjoja. *Kauppalehti*, 21 12.

Skjäl, A., 2016. *Course 400212.0. Försöksplanering.* Turku: Åbo Akademi.

Sundqvist, H., 2010. Drying section ventilation and heat recovery. In: M. Karlsson, ed. *Papermaking Science and Technology; Papermaking Part 2, Drying.* Helsinki: Paper Engineers' Association/Paperi ja Puu Oy, pp. 446-454.

Tsilingiris, P. T., 2008. Thermophysical and transport properties of humid air at temperature range between 0 and 100 C. *Energy Conversion and Management,* Volume 48, pp. 1098-1110.

Ukkola, K., 1997. *Alipainetelan rakenteen kehittäminen paperikoneen kuivatusosan päällepuhalluskonseptiin.* Masters thesis. Jyväskylä: Lappeenrannan teknillinen korkeakoulu, Konetekniikan osasto.

Valmet Technologies Inc., 2012. *Valmet Technical Paper Series, Upgrading Runnability,* s.l.: s.n.

Westerlund, T., 2013. *Anläggnings- och systemteknik.* Turku: Åbo Akademi University, Process Design and Systems Engineering Laboratory.

Widlund, O. N. G., Ragvald, H. S., Halldin, C. B. H. & Lindqvist, N. L. O., 1997. Aerodynamics of high-speed paper machines. *Tappi Journal,* 80(4), pp. 113-118.

Voith Paper GmbH & Co. KG, 2017. *ProRelease+.* [Online]
Available at: http://voith.com/corp-en/papermaking/prorelease.html
[Accessed 22 May 2018].

Zevenhoven, R., 2013. *Introduction to Process Engineering.* Turku: Åbo Akademi University, Thermal and Flow Engineering Laboratory.

Zevenhoven, R., 2018. *Course material, 424521, Fluid and Particulate Systems.* Turku, Åbo Akademi University, Thermal and Flow Engineering.

APPENDIX A: Groove and suction roll models

APPENDIX A.1. The groove model

The main function of the grooved model

```
%% Groove modelling, only mass balance and viscous losses accounted
for!
% Copyright Prof. Henrik Saxén & B.Sc. Ella Pirttikangas

clear all
close all
clc
format compact
tic
%% Define the parameters for the groove
pstart = 101000;      % Initial pressure, Pa
pend   = 100500;      % End pressure, Pa
p0     = 101300;      % External pressure, Pa
n=99;                 % Discretization steps
D=0.005;               % Channel width
L=10;                  % Channel length
w = 1200/60;          % Cylinder speed, m/s
t=0:L/(w*(n+1)):L/w;  % Time steps simulated, s
KV = [0 1 10 50 400 650 1000 1750]/3600;    % Fabric permeability
factors m^3/m^2*s

%% Set up initial guess of the pressure field
dp=(pstart-pend)/(n+1);    % Pressure step (uniform)

% Set up the solver for needed set up (Fsolve solves normally only
400
% iterations)

OPTS =
optim.options.Fsolve('MaxIterations',10000,'MaxFunctionEvaluations',
500000);

%% Initialize the matrices to build up, this will make your code
faster
k = length(KV);
DM = zeros(n,k);
P = zeros(n,k);
M = zeros(n+1,k);
MV = zeros(n,k);
WW = zeros(n,k);

 %% Solve the pressures, masses and velocities for each permeability
for i=1:k
     K=KV(i);
     % Initial guesses
     if i==1
         pini0 = [pstart:-dp:pend];  % Initial pressure vector
         pini(1:n)=pini0(2:n+1);    % Skip boundary values
         %f = 0.03*ones(1,n+1);
```

```
     else
        pini=pold;
        %f = fold;
     end
    p = pini;
    %pf = [pini f]; % Solve the variables for pressure and friction

    % Solve the pressure field
    [p, dm] =
fsolve(@groove_pressure,p,OPTS,K,pstart,pend,p0,w,L,D,n);
    P(:,i) = p;
    %F(:,i) = PF(n+1:end);
    DM(:,i) = dm;
    pold = p; %use the answer as guess for the following round
    %fold = PF(n+1:end);


    % Get the mass flows and velocities
    [m, mv, ww] =
groove_pressurefield_results(p,K,pstart,pend,p0,w,L,D,n);

    % Save the answers to the matrices
    M(:,i) = m;
    MV(:,i) = mv;
    WW(:,i) = ww;


end
 figure(1)
%     subplot(3,1,1);
%    plot([0 1:n n+1],[pstart/1000 p(1:n)/1000 pend/1000]);
    Pstart = pstart*ones(1,length(KV));
    Pend = pend*ones(1,length(KV));
    Pa =[Pstart;P;Pend]/1000;
    plot(1000*t,Pa);
    hold on
%    plot([0 n+1],[p0 p0]/1000,'k--')
    plot(1000*[0 t(n+1)],[p0 p0]/1000,'k--')
    ylabel('p (kPa)')
    figure(2)
    %subplot(3,1,2);
    plot(1000*t(1:n),1000*M(1:n,:));
    hold on;
    plot(1000*t(1:n),1000*MV,'r--')
    %axis([0 n+1 -10 10])
    ylabel('m, m_v (g/s)')
    figure(3)%subplot(3,1,3);
    hold  on
    plot(1000*t(1:n),WW);
 %   axis([0 n+1 -5 70])
    xlabel('t (ms)')
    ylabel('w (m/s)')
%% Include Reynolds and friction coefficient, use the obtained
answer as initial guess

F = 0.03*ones(n+1,length(KV));
PF = [P;F];
Pnew = zeros(n,length(KV));
Fnew = zeros(n+1,length(KV));
```

```
DMnew = zeros(n+1,length(KV));
Mnew = zeros(n+1,length(KV));
MVnew = zeros(n,length(KV));
WWnew = zeros(n+1,length(KV));

OPTS =
optim.options.Fsolve('MaxIterations',10000,'MaxFunctionEvaluations',
500000, 'FunctionTolerance',1*10^-4);

for i = 1:length(KV)
 K=KV(i);
 p = PF(1:n,i);
 f = PF(n+1:end,i);

 pfini = [p;f]; % initial guess for the friction coeff and the
pressure

    % Solve the pressure field
    [pf, dm] =
fsolve(@groove_friction,pfini,OPTS,K,pstart,pend,p0,w,L,D,n);
    Pnew(:,i) = pf(1:n);
    Fnew(:,i) = pf(n+1:end);
    DMnew(:,i) = dm;



    % Get the mass flows
    [m, mv, ww] = groove_friction(pf,K,pstart,pend,p0,w,L,D,n);%
    Mnew(:,i) = m;
    MVnew(:,i) = mv;
    WWnew(:,i) = ww;

end

%% Plot the results
    figure(4)
%     subplot(3,1,1);
%    plot([0 1:n n+1],[pstart/1000 p(1:n)/1000 pend/1000]);
    Pstart = pstart*ones(1,length(KV));
    Pend = pend*ones(1,length(KV));
    Pa =[Pstart;Pnew;Pend]/1000;
    plot(1000*t,Pa,'linewidth',2);
    hold on
%    plot([0 n+1],[p0 p0]/1000,'k--')
    plot(1000*[0 t(n+1)],[p0 p0]/1000,'k--','linewidth',2)
    ylabel('p (kPa)','fontsize',22)
    %title('Pressure profile over the groove with inlet pressure 102
kPa and outlet pressure 99,8 kPa, wall velocity 1200 m/min')
    legend('0 m^3/m^2*h','10
m^3/m^2*h','50m^3/m^2*h','400m^3/m^2*h','650
m^3/m^2*h','1000m^3/m^2*h','1750m^3/m^2*h')
    xlabel('Time step (ms)','fontsize',22)
    set(gca,'fontsize',20)
    orient('landscape')
    print('-bestfit','groove_pressure_102', '-dpdf')
    figure(5)
    %subplot(3,1,2);
    plot(1000*t(1:n),1000*Mnew(1:n,:),'linewidth',2);
```

```
    hold on;
    plot(1000*t(1:n),1000*MVnew,'r--','linewidth',2)
    %axis([0 n+1 -10 10])
    ylabel('mass flow and mass flow losses (g/s)','fontsize',22)
    xlabel('Time step (ms)','fontsize',22)
    set(gca,'fontsize',20)
    %title('Mass flow profile over the groove with inlet pressure
102 kPa and outlet pressure 99,8 kPa, wall velocity 1200
m/min','fontsize',22)
    legend('0 m^3/m^2*h','100
m^3/m^2*h','200m^3/m^2*h','400m^3/m^2*h','650
m^3/m^2*h','1000m^3/m^2*h','1750m^3/m^2*h','location','southwest')
    orient('landscape')
    print('-bestfit','groove_mass_102', '-dpdf')
    figure(6)%subplot(3,1,3);
    hold  on
    plot(1000*t(1:n+1),WWnew,'linewidth',2);
 %   axis([0 n+1 -5 70])
    xlabel('Time step (ms)','fontsize',22)
    ylabel('air velocity (m/s)','fontsize',22)
    set(gca,'fontsize',20)
    %title('Velocity profile over the groove with inlet pressure 102
kPa and outlet pressure 99,8 kPa, wall velocity 1200
m/min','fontsize',22)
    legend('0 m^3/m^2*h','100
m^3/m^2*h','200m^3/m^2*h','400m^3/m^2*h','650
m^3/m^2*h','1000m^3/m^2*h','1750m^3/m^2*h')
     orient('landscape')
    print('-bestfit','groove_velo_102', '-dpdf')
%     pause(0.2)
%% The friction and Reynolds number change over the iteration
figure(7)
plot(1:n+1,Fnew);
title('Frictionfactor over the time steps')
ylabel('Friction factor')
xlabel('Time steps (ms)')

figure(8)
Dh = 2*D^2/(4*2*D);
Re =((WW-w)*Dh)/(1.568*10^-5);
plot(1:n,Re,'linewidth',2);
%title('Reynolds number over the time steps')
ylabel('Reynolds number','fontsize',22)
xlabel('Time steps (ms)','fontsize',22)
set(gca,'fontsize',20)
legend('0 m^3/m^2*h','100
m^3/m^2*h','200m^3/m^2*h','400m^3/m^2*h','650
m^3/m^2*h','1000m^3/m^2*h','1750m^3/m^2*h')
orient('landscape')
print('-bestfit','groove_rey_102', '-dpdf')

toc
```

The `groove_pressure` function:

```
function [f] = groove_pressure(p,K,pstart,pend,p0,w,L,D,n)

%Parameters
dL=L/n;
rho=1.25; %kg/m^3 density of the air
kvis = 1.568*10^-5;   %[m^2/s] Kinematic viscosity

% Internal variables
pp(1)=pstart;
pp(2:n+1)=p(1:n);
pp(n+2)=pend;
fg = p(n+1:end);
Dh = 4*D^2/(2*2*D);
x = 0.046*10^-3;
for i=2:n+1
%     ww(i-1)=sqrt(2*Dh/(dL*rho*fg(i-1)))*(pp(i-1)-
pp(i))/sqrt(abs(pp(i-1)-pp(i)))+w;
%     ww(i)=sqrt(2*Dh/(dL*rho*fg(i)))*(pp(i)-
pp(i+1))/sqrt(abs(pp(i)-pp(i+1)))+w;
%     %fg(i-1)=0.25/(log10(x/(3.7*Dh)+5.74/(sign(ww(i-1)-
w)*(((abs(ww(i-1)-w)*Dh)/kvis)^0.9))))^2;
%     fg(i)=0.25/(log10(x/(3.7*Dh)+5.74/(sign(ww(i)-w)*((abs(ww(i)-
w)*Dh)/kvis)^0.9)))^2;
    m(i-1)=(sqrt(2*Dh/(dL*rho*0.03))*(pp(i-1)-pp(i))/sqrt(abs(pp(i-
1)-pp(i)))+w)*D^2*rho;
    mv(i-1)=sign(p0-p(i-1))*K*(abs(p0-p(i-1))/100)^0.7*rho*dL*D;
    m(i)=(sqrt(2*Dh/(dL*rho*0.03))*(pp(i)-pp(i+1))/sqrt(abs(pp(i)-
pp(i+1)))+w)*D^2*rho;
    dm(i-1)=m(i-1)+mv(i-1)-m(i);
end
f=1000*dm;
%pause
```

The `groove_pressurefield_results` function:

```
function [m mv ww] =
groove_pressurefield_results(p,K,pstart,pend,p0,w,L,D,n)

% Parameters
dL=L/n;
rho=1.25;

% Internal variables
pp(1)=pstart;
pp(2:n+1)=p(1:n);
pp(n+2)=pend;
Dh = 4*D^2/(2*2*D);
for i=2:n+1
    m(i-1)=(sqrt(2*Dh/(dL*rho*0.03))*(pp(i-1)-pp(i))/sqrt(abs(pp(i-
1)-pp(i)))+w)*D^2*rho;
    mv(i-1)=sign(p0-p(i-1))*K*(abs(p0-p(i-1))/100)^0.7*rho*dL*D;
    m(i)=(sqrt(2*Dh/(dL*rho*0.03))*(pp(i)-pp(i+1))/sqrt(abs(pp(i)-
pp(i+1)))+w)*D^2*rho;
    dm(i-1)=m(i-1)+mv(i-1)-m(i);
```

```
    ww(i-1)=sqrt(2*Dh/(dL*rho*0.03))*(pp(i-1)-pp(i))/sqrt(abs(pp(i-
1)-pp(i)))+w;
end
pf=1000*dm;
%pause
```

The `groove_friction` function:

```
%% Groove frictioncoeff. and Reynolds calculated
% Ella Pirttikangas, 11.6.2018, Masters thesis
function [m, mv, ww] = groove_friction(p,K,pstart,pend,p0,w,L,D,n)
%Parameters
dL=L/n;
rho=1.25; %kg/m^3 density of the air

kvis = 1.568*10^-5;   %[m^2/s] Kinematic viscosity

pp(1)=pstart;
pp(2:n+1)=p(1:n);
pp(n+2)=pend;
fg = p(n+1:end);
Dh = 4*D^2/(2*2*D);
x = 0.046*10^-3; %[m] surface roughness


for i=2:n+1
    ww(i-1)=sqrt(2*Dh/(dL*rho*fg(i-1)))*(pp(i-1)-
pp(i))/sqrt(abs(pp(i-1)-pp(i)))+w;
    ww(i)=sqrt(2*Dh/(dL*rho*fg(i)))*(pp(i-1)-pp(i))/sqrt(abs(pp(i-
1)-pp(i)))+w;
    fg(i-1) = 0.25/(log10(x/(3.7*Dh)+sign(ww(i-1))*5.74/((abs(ww(i-
1)-w)*Dh)/kvis)^0.9))^2;
    fg(i) = 0.25/(log10(x/(3.7*Dh)+sign(ww(i))*5.74/((abs(ww(i)-
w)*Dh)/kvis)^0.9))^2;
    m(i-1)=(sqrt(2*Dh/(dL*rho*fg(i-1)))*(pp(i-1)-
pp(i))/sqrt(abs(pp(i-1)-pp(i)))+w)*D^2*rho;
    mv(i-1)=sign(p0-p(i-1))*K*(abs(p0-p(i-1))/100)^0.7*rho*dL*D;
    m(i)=(sqrt(2*Dh/(dL*rho*fg(i)))*(pp(i)-pp(i+1))/sqrt(abs(pp(i)-
pp(i+1)))+w)*D^2*rho;
    dm(i-1)=m(i-1)+mv(i-1)-m(i);
end
```

APPENDIX A.2. The Suction roll model

The main function for the suction roll model

```
%% VacRoll simple simulation, only mass and viscous losses
calculated
% Ella Pirttikangas and Prof. Henrik Saxén
%Code bases on the model created by PRof. Saxén

clear all
clc
clf
close all

tic
pstart = 100700;       % Initial pressure, Pa
pend   = 99800;       % End pressure, Pa
p0     = 101300;       % External pressure, Pa
pvac   = 99300;       % Pressure in the suctionroll
n=30;                 % Discretization steps
dhole = 0.005;          % Diameter of vac roll hole
D=0.01;               % Channel width
L=2;                   % Channel length
w = 2200/60;           % Cylinder speed, m/s
t=0:L/(w*(n+1)):L/w;   % Time steps simulated, s

% Set up initial guess of the pressure field
dp=(pstart-pend)/(n+1);     % Pressure step (uniform)
%options = optimoptions('fsolve','MaxFunctionEvaluations',10000);
OPTS =
optim.options.Fsolve('MaxIterations',10000,'MaxFunctionEvaluations',
500000);
KV = [0 50 200 500 650 1000 1750]/3600;     % Fabric permeability
factors m^3/m^2*s
DM = zeros(n,length(KV));
P = zeros(n,length(KV));
M = zeros(n+1,length(KV));
MV = zeros(n,length(KV));
MVAC = zeros(n,length(KV));
WW = zeros(n,length(KV));


for i=1:length(KV)
     K=KV(i);
     % Initial guesses
     if i==1
         pini0 = [pstart:-dp:pend];  % Initial pressure vector
         pini(1:n)=pini0(2:n+1);     % Skip boundary values
     else
        pini=pold;
     end

     % K=input('\n K = ');

    % Solve the pressure field
```

```
    [p, dm, exitflag] =
fsolve(@Vacsim_pressurefield,pini,OPTS,K,pstart,pend,p0,pvac,w,L,D,d
hole,n);
    P(:,i) = p;
    DM(:,i) = dm;
    pold=p;


    % Get the mass flows
    [m, mv,mvac, ww] =
Vacsim_pressureresults(p,K,pstart,pend,p0,pvac,w,L,D,dhole,n);%
    M(:,i) = m;
    MV(:,i) = mv;
    MVAC(:,i) = mvac;
    WW(:,i) = ww;

end

  figure(1)
%     subplot(3,1,1);
%    plot([0 1:n n+1],[pstart/1000 p(1:n)/1000 pend/1000]);
    Pstart = pstart*ones(1,length(KV));
    Pend = pend*ones(1,length(KV));
    Pa =[Pstart;P;Pend]/1000;
    plot(1000*t,Pa);
    hold on
%    plot([0 n+1],[p0 p0]/1000,'k--')
    plot(1000*[0 t(n+1)],[p0 p0]/1000,'k--')
    ylabel('p (kPa)')
    figure(2)
    %subplot(3,1,2);
    plot(1000*t(1:n),1000*M(1:n,:));
    hold on;
    plot(1000*t(1:n),1000*MV,'r--')
    plot(1000*t(1:n),1000*MVAC,'b--')
    %axis([0 n+1 -10 10])
    ylabel('m, m_v (g/s)')
    figure(3)%subplot(3,1,3);
    hold  on
    plot(1000*t(1:n),WW);
 %   axis([0 n+1 -5 70])
    xlabel('t (ms)')
    ylabel('w (m/s)')


%% Calculate the pressures with Reynolds and friction coefficient
F = 0.03*ones(n+1,length(KV));
PF = [P;F];
Pnew = zeros(n,length(KV));
Fnew = zeros(n+1,length(KV));
DMnew = zeros(n+1,length(KV));
Mnew = zeros(n+1,length(KV));
MVnew = zeros(n,length(KV));
MVACnew = zeros(n,length(KV));
WWnew = zeros(n+1,length(KV));

OPTS =
optim.options.Fsolve('MaxIterations',10000,'MaxFunctionEvaluations',
500000, 'FunctionTolerance',1*10^-4);
```

```
for i = 1:length(KV)
 K=KV(i);
 p = PF(1:n,i);
 f = PF(n+1:end,i);

 pfini = [p;f]; % initial guess for the friction coeff and the
pressure

    % Solve the pressure field
    [pf, dm] =
fsolve(@Vacsim_friction,pfini,OPTS,K,pstart,pend,p0,pvac,w,L,D,dhole
,n);
    Pnew(:,i) = pf(1:n);
    Fnew(:,i) = pf(n+1:end);
    DMnew(:,i) = dm;



    % Get the mass flows
    [m, mv,mvac, ww] =
Vacsim_friction(pf,K,pstart,pend,p0,pvac,w,L,D,dhole,n);%
    Mnew(:,i) = m;
    MVnew(:,i) = mv;
    MVACnew(:,i) = mvac;
    WWnew(:,i) = ww;

end

%% Plot the results
    figure(4)
%     subplot(3,1,1);
%    plot([0 1:n n+1],[pstart/1000 p(1:n)/1000 pend/1000]);
    Pstart = pstart*ones(1,length(KV));
    Pend = pend*ones(1,length(KV));
    Pa =[Pstart;Pnew;Pend]/1000;
    plot(1000*t,Pa, 'linewidth',2);
    hold on
%    plot([0 n+1],[p0 p0]/1000,'k--')
    plot(1000*[0 t(n+1)],[p0 p0]/1000,'k--','linewidth',2)
    ylabel('p (kPa)','fontsize',22)
    xlabel('Time step (ms)','fontsize',22)
    %title('Pressure in cylinder 99,3 kPa, inlet pressure 100,7 kPa
and outlet pressure 99,8 kPa, wall velocity 1200
m/min','fontsize',22)
    legend('0 m^3/m^2*h','50
m^3/m^2*h','200m^3/m^2*h','500m^3/m^2*h','650
m^3/m^2*h','1000m^3/m^2*h','1750m^3/m^2*h')
    set(gca,'fontsize',20)
    orient('landscape')
    print('-bestfit','Vac_pressure_100,7', '-dpdf')
    figure(5)
    %subplot(3,1,2);
    plot(1000*t(1:n),1000*Mnew(1:n,:),'linewidth',2);
    hold on;
    plot(1000*t(1:n),1000*MVnew,'r--','linewidth',2)
    plot(1000*t(1:n),1000*MVACnew,'b--','linewidth',2)
    %axis([0 n+1 -10 10])
```

```
    ylabel('mass flow, mass flow losses and mass flow evacuated from
groove (g/s)')
    xlabel('Time step (ms)','fontsize',22)
    set(gca,'fontsize',20)
    %title('Pressure in cylinder 99.3 kPa, inlet pressure 100.7 kPa
and outlet pressure 99.8 kPa, wall velocity 1200
m/min','fontsize',22)
    legend('0 m^3/m^2*h','50
m^3/m^2*h','200m^3/m^2*h','500m^3/m^2*h','650
m^3/m^2*h','1000m^3/m^2*h','1750m^3/m^2*h')
    orient('landscape')
    print('-bestfit','Vac_mass_100,7', '-dpdf')
    figure(6)%subplot(3,1,3);
    hold  on
    plot(1000*t(1:n+1),WWnew,'linewidth',2);
 %   axis([0 n+1 -5 70])
     xlabel('Time step (ms)','fontsize',22)
    ylabel('Air velocity (m/s)','fontsize',22)
    set(gca,'fontsize',20)
    %title('Pressure in cylinder 99.3 kPa, inlet pressure 100.7 kPa
and outlet pressure 99.8 kPa, wall velocity 1200
m/min','fontsize',22)
    legend('0 m^3/m^2*h','50
m^3/m^2*h','200m^3/m^2*h','500m^3/m^2*h','650
m^3/m^2*h','1000m^3/m^2*h','1750m^3/m^2*h')
    orient('landscape')
    print('-bestfit','Vac_velocity_100,7', '-dpdf')
%     pause(0.2)
%% The friction and Reynolds number change over the iteration
figure(7)
plot(1:n+1,Fnew);
ylabel('Friction factor')
xlabel('Time steps (ms)')

figure(8)
Dh = 2*D^2/(4*2*D);
Re =((WW-w)*Dh)/(1.568*10^-5);
plot(1:n,Re);
title('Reynolds number over the time steps')
ylabel('Reynolds number')
xlabel('Time steps (ms)')

toc
```

The `Vacsim_pressurefield` function:

```
%% This function calculates the pressuresan masses
function [f] =
Vacsim_pressurefield(p,K,pstart,pend,p0,pvac,w,L,D,dhole,n)
%Parameters
dL=L/n;
rho=1.25; %kg/m^3 density of the air
kvis = 1.568*10^-5;   %[m^2/s] Kinematic viscosity

% Internal variables
pp(1)=pstart;
pp(2:n+1)=p(1:n);
pp(n+2)=pend;
Dh = 4*D^2/(2*2*D);
```

```
x = 0.046*10^-3;
fel = 0.5+1.1; %the friktion coeff of elements
fg = 0.03;
for i=2:n+1
    m(i-1)=(sqrt(2*Dh/(dL*rho*fg))*(pp(i-1)-pp(i))/sqrt(abs(pp(i-1)-
pp(i)))+w)*D^2*rho;
    mv(i-1)=sign(p0-p(i-1))*K*(abs(p0-p(i-1))/100)^0.7*rho*dL*D;
    mvac(i-1) = rho*0.25*pi*dhole^2*sqrt(2*fel/rho)*((p(i-1)-
pvac)/sqrt(p(i-1)-pvac));
    m(i)=(sqrt(2*Dh/(dL*rho*fg))*(pp(i)-pp(i+1))/sqrt(abs(pp(i)-
pp(i+1)))+w)*D^2*rho;
    dm(i-1)=m(i-1)+mv(i-1)-m(i)-mvac(i-1);
end
f=1000*dm;
%pause
```

The `Vacsim_pressureresults` function:

```
%% This calculates the results of the pressurefield optimisation
function [m mv mvac ww] =
Vacsim_pressureresults(p,K,pstart,pend,p0,pvac,w,L,D,dhole,n)%

% Parameters
dL=L/n;
rho=1.25;

% Internal variables
pp(1)=pstart;
pp(2:n+1)=p(1:n);
pp(n+2)=pend;
Dh = 4*D^2/(2*2*D);
fel = 0.5+1.1;
fg = 0.03;
for i=2:n+1
    m(i-1)=(sqrt(2*Dh/(dL*rho*fg))*(pp(i-1)-pp(i))/sqrt(abs(pp(i-1)-
pp(i)))+w)*D^2*rho;
    mv(i-1)=sign(p0-p(i-1))*K*(abs(p0-p(i-1))/100)^0.7*rho*dL*D;
    mvac(i-1) = rho*0.25*dhole^2*sqrt(2*fel/rho)*((p(i-1)-
pvac)/sqrt(p(i-1)-pvac));
    m(i)=(sqrt(2*Dh/(dL*rho*fg))*(pp(i)-pp(i+1))/sqrt(abs(pp(i)-
pp(i+1)))+w)*D^2*rho;
    dm(i-1)=m(i-1)+mv(i-1)-m(i)-mvac(i-1);
    ww(i-1)=sqrt(2*Dh/(dL*rho*fg))*(pp(i-1)-pp(i))/sqrt(abs(pp(i-1)-
pp(i)))+w;
end
pf=1000*dm;
%pause
```

The `Vacsim_friction` function:

```
%% The effect of the friction coefficient on the viscous losses
% Ella Pirttikangas, 11.6.2018, Masters thesis
function [m, mv,mvac, ww] =
Vacsim_friction(p,K,pstart,pend,p0,pvac,w,L,D,dhole,n)
%Parameters
dL=L/n;
rho=1.25; %kg/m^3 density of the air

kvis = 1.568*10^-5;   %[m^2/s] Kinematic viscosity
```

```
pp(1)=pstart;
pp(2:n+1)=p(1:n);
pp(n+2)=pend;
fg = p(n+1:end);
Dh = 4*D^2/(2*2*D);
x = 0.046*10^-3; %[m] surface roughness
fel = 0.5+1.1; %the friktion coeff of elements


for i=2:n+1
    ww(i-1)=sqrt(2*Dh/(dL*rho*fg(i-1)))*(pp(i-1)-
pp(i))/sqrt(abs(pp(i-1)-pp(i)))+w;
    ww(i)=sqrt(2*Dh/(dL*rho*fg(i)))*(pp(i-1)-pp(i))/sqrt(abs(pp(i-
1)-pp(i)))+w;
    fg(i-1) = 0.25/(log10(x/(3.7*Dh)+sign(ww(i-1))*5.74/((abs(ww(i-
1)-w)*Dh)/kvis)^0.9))^2;
    fg(i) = 0.25/(log10(x/(3.7*Dh)+sign(ww(i))*5.74/((abs(ww(i)-
w)*Dh)/kvis)^0.9))^2;
    m(i-1)=(sqrt(2*Dh/(dL*rho*fg(i-1)))*(pp(i-1)-
pp(i))/sqrt(abs(pp(i-1)-pp(i)))+w)*D^2*rho;
    mv(i-1)=sign(p0-p(i-1))*K*(abs(p0-p(i-1))/100)^0.7*rho*dL*D;
    mvac(i-1) = rho*0.25*pi*dhole^2*sqrt(2*fel/rho)*((p(i-1)-
pvac)/sqrt(p(i-1)-pvac));
    m(i)=(sqrt(2*Dh/(dL*rho*fg(i)))*(pp(i)-pp(i+1))/sqrt(abs(pp(i)-
pp(i+1)))+w)*D^2*rho;
    dm(i-1)=m(i-1)+mv(i-1)-m(i)-mvac(i-1);
end
%f = 1000*dm;
```

APPENDIX B: Experiments; methodology and analysis

Most of the analysis of the pilot machine is based on pressure measurements, but also other values such as the running speed and fabric tension are measured and controlled. Two Bachelors theses studied the measurement setup and the functions of the machinery, which is why the present author refers to the two theses for further details.

To obtain the pressure profile over the perimeter of the cylinder, pressure sensors were installed on the casing of the cylinder. The concept of converting of the signal into data is seen in Figure B1; first the pressure signal at the sensor is transformed to an electrical signal and wires drawn from the cylinder inner wall to the axis transfer signals through a slip ring to the bridge amplifier and to the oscilloscope, where they can be monitored. The oscilloscope creates a csv-file with the sensor output. The output is then converted and analysed using MatWorks® MatLab.

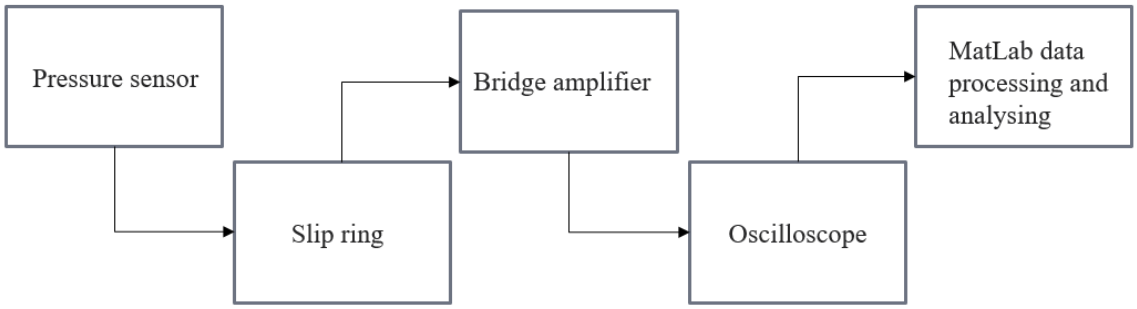

Figure B1 Data collection of the pressure sensors at the cylinder surface.

The sensors used were piezoresistive sensors, where the sensor materials are semiconductors, which change their resistivity with applied force. Semiconductors are ten times more sensitive compared to metal or alloy strain gauges (Fagervik, 2009, p. 30) and they fit well to a dynamic measuring environment (Miulus, 2010, p. 11). The pilot machine has two kinds of sensors, which have different accuracies and form. The more accurate sensor is illustrated in Figure B2 and the data sheets for both sensors are found in Appendix B.3 and Appendix B.4.

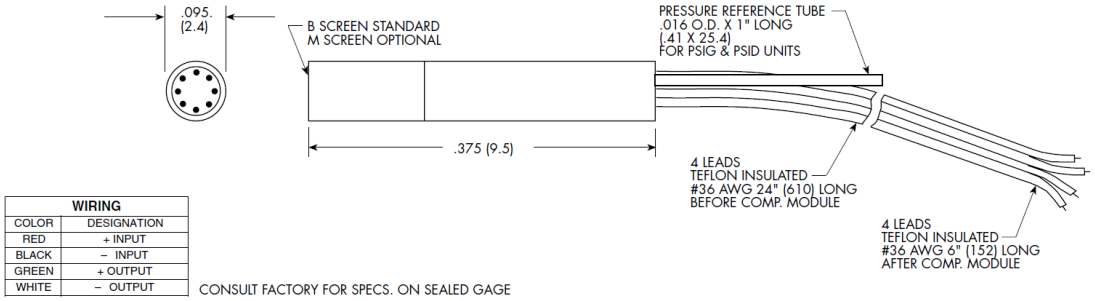

Figure B2 Piezoresistive sensor Kulite XCE-093 Series (Kulite - Semiconductor Products, Inc., 2018)

The sensors are installed on the surface in different ways to obtain information on how the installation will affect the measurement signal. Miulus mentions that the measuring signal should be less than 20% of the resonance frequency caused by the installation pipe, in the installation set up, to be able to neglect the effect of the installation. The method of calculation is found in Miulus, 2010, p.12.

The rotating movement of the cylinder produces some problems for the transmission of the electrical signal out of the cylinder. In this pilot machine the problem is solved by using a slip ring. Figure B3 shows the head and the body of the slip ring used in the trials. The electronical signal is sent through wiring to the axis of the cylinder, where the signals is transported in the slip ring through the carbon brushes further to the measuring equipment (Kulmala, 2012, p. 28). The transmission through carbon brushes is not the ideal solution due to the resistance of the brushes and the possible disturbances of the rotational motion of the cylinder (Miulus, 2010, p. 15).

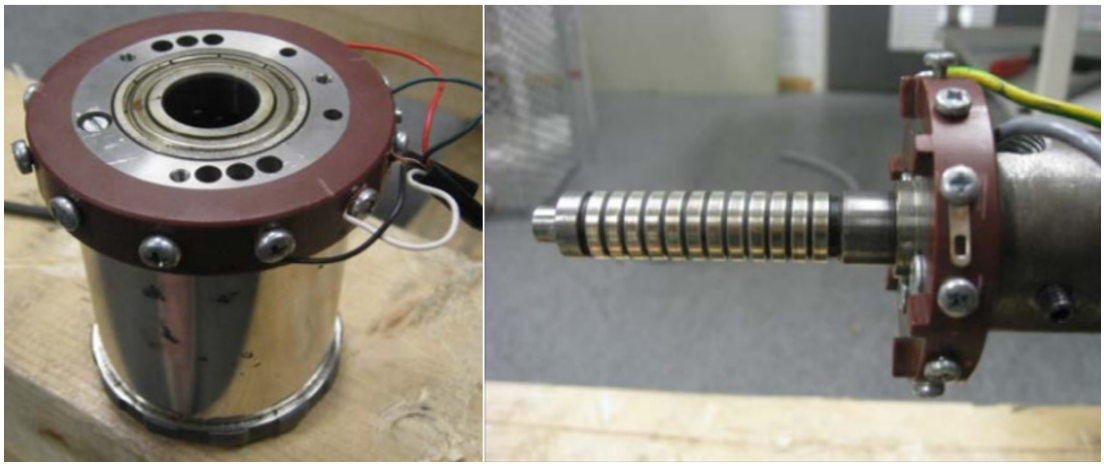

Figure B3 Slip ring head and body (Kulmala, 2012).

When the signal is successfully transferred outside the cylinder, the signal is amplified, by the scalar chosen, which is 20 times the incoming signal (Miulus, 2010, p. 17). The bridge amplifier is important for obtaining a good signal/noise ratio and the calibration of the signal occurs in the bridge amplifier. The sensors are calibrated, when they are installed and the calibration requires the sensor to be stationary and in atmosheric pressure. This will set the output signal to be zero. Zeroing is done after the sensors have been on for 15 minutes to reduce creeping of the signal.

The signals are measured and saved at the digital oscilloscope. According to Miulus 2010, the number of samples per measuring sequence is 125 000. This will make the sample distance on the cylinder surface 0.3-0.5 mm depending on the cylinder diameter. The oscilloscope has some built-in calulation algorithms to average the signal to filter out noice. This produces an average over a certain number of rotations, in our case eight. The rotations are measured by a laser trigger, which gives a signal that starts the measuring in the oscilloscope. It is important for the averaging that the pressure signal is periodical, so the same outcome is approximately produced in each rotation (Miulus, 2010, p. 23). Additionally, one should remember that the averaging algorithm will reduce the amount of samples to 1000, regardless of the measurement time chosen. The restricted sample amount is due to restricted inner memory and calculation capacity (Miulus, 2010, p. 24). This will consequently affect the physical sample distance between the the recorded samples.

The oscilloscope produces a data file, which will be converted and handeled through a Matlab algorithm. After the data is loaded to the MatWorks® MatLab enviroment the data is converted from electronical signal (mV) to a pressure signal (Pa). The MatLab code found in Appendix B.2 utilises calibration curves made according to the quality standards of Valmet. Measuring equipment, used for the calibrations, is calibrated by an accredited third party and the actual measuring equipment is then further calibrated using the accredited equipment. The pressure is created at the sensor using a pump with known characteristics and the potential after the bridge is measured. Next, calibration curves as illustrated in Figure B4 can be drawn. The grey curve is for the Kulite sensor, where the pressure interval was ±35 kPa and the two remaining curves

are for the Honeywell sensors, where the pressure interval was ±7 kPa. The measuring voltage stayed the same, which explains the angular coefficient of the curves.

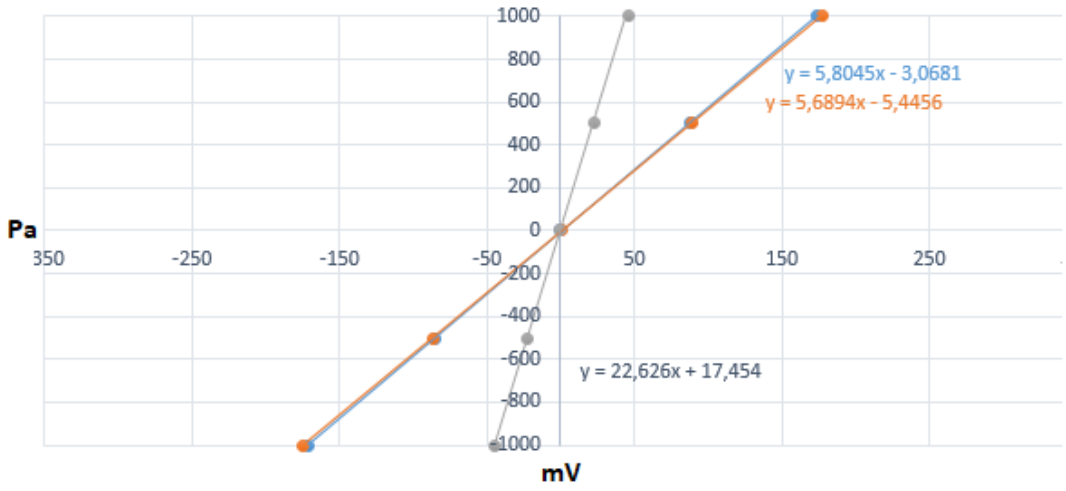

Figure B4 Calibration curves of the three pressure sensors.

Pressure measurements are often used as secondary measurements of other variables for instance volumetric flow and levels (Fagervik, 2009, p. 27). In the pilot machine, the volumetric flow to the blow box nozzles is measured by measuring the dynamic pressure at the inlet of the blow box. The pressure measurement is made using an autozeroing micromanometer (Mikor TT370S), the technical data sheet of which is found in Appendix B.5. These devices are calibrated internally once a year, in accordance with to the quality standards of the company. The same digital pressure devices are used to measure the static point measurements (cf. Figure 32).

The airflow to the blow box are measured by dynamic pressure measurements using the following empirical equation given by the manufacturer of the graduated collar:

$$Q_1 = k_1\sqrt{\frac{\Delta p}{[Pa]}} \quad \left[m^3/_h\right] \tag{27}$$

$$Q_2 = k_2\sqrt{\frac{\Delta p}{[Pa]}} \quad \left[m^3/_s\right] \tag{28}$$

The constants, $k_1$and k_2 are obtained empirically and they are dependent on the diameter of the graduated collar.

APPENDIX B.1. Analysis of the methodology

The pressure profiles obtained in the runnability trials were of interest, especially in the crucial areas from a web-handling point-of view. Since the measuring environment is dynamic and the pressure changes are minor, some special conditions need to be set for the measuring equipment. In this Appendix, the sensitivity and limitations of the conducted measurements is discussed, but temperature effects are not considered. For further reading and more detailed calculations on the compatibility of the equipment in this measuring environment, please refer to Miulus 2010. One should consider the calculated values merely as indicative, since one cannot accurately determine how the manufacturers have defined the reported errors.

The airflow and the point measurements are made using an autozeroing micromanometer (Mikor TT370S). The device is known to be reliable and it is widely used in field measurements. The micromanometer measurement interval is ±1999 Pa and the error is ± 1 % of the output value, according to the data sheet in Appendix B.5. The only known disturbance from earlier experience is that the sensors may be disturbed by external magnetic fields, which might cause error in the reset of the devices.

The system has very fast dynamics, which consequently sets some requirements for the dynamics of the equipment. Particularly, the pressure sensors on the cylinder surface need to be assessed, because the analysis of the concepts are largely based on the data produced by the sensors. Additionally, the dynamics over the nip areas are very fast, which set some constraints on the sensor dynamics. In the trials, three sensors were installed on the cylinder casing, one at the edge, so that the masking tape still covers the sensor, one in the middle of the cylinder and one in between the other two.

Two types of sensors were used by different manufacturers. One of the sensors was more expensive and accurate, whereas two of the sensors were cheaper and of lower accuracy. Data sheets for the sensors are given in Appendix B.3 and in Appendix B.4. When mapping the accuracy of the pressure sensors, the dynamics of the sensors have

to be inspected as well as the total accuracy of the system, including the sensors, the amplifier bridge and the oscilloscope accuracy.

The digital oscilloscope used in the studies was manufactured by Agilent Technology (Agilent Technologies, 2009). Miulus, 2010, mentions that the total vertical resolution has a large impact on the uncertainty of the oscilloscope. The vertical resolution is bases on quant size, which further is dependent on the ADC-converter of the oscilloscope and the available memory. Miulus states that the optimal setup for the oscilloscope is a built in High Resolution set up, which produces more data points over the measuring sequence and with smaller quant size. The High Resolution set up records 3200 points over a measuring sequence and the maximum 12 bit accuracy (Miulus, 2010, pp. 39-40), which will according to the manufacturer improve the vertical resolution and the signal and noise ratio (Agilent Technologies, 2009, p. 266). Another built-in set up, which was used during the studies is called Average 8. As referred in the previous section, the averaging requires a stable trigger and the pressure profile should be somewhat uniform; using a higher number of averaging will produce better vertical total resolution (Agilent Technologies, 2009, p. 267). The Average 8-function produces fewer measuring points (1000 points) and the vertical accuracy is 9 bits (Miulus, 2010, p. 40). Miulus calculated the accuracy of the oscilloscope with

$$\varepsilon = \frac{U_{Oscilloscope,FS} / N_{adc}}{U_{Sensor,FSO} \cdot X_{amplifier}} \cdot 100\ \% \qquad (29)$$

The quant size is the measuring interval for the oscilloscope, $U_{Oscilloscope,FS}$, divided by the vertical resolution, N_{adc}. Dividing the quant size by the incoming signal, which is the sensor voltage, $U_{Sensor,FSO}$, times the amplification of the bridge, $X_{amplifier}$, will give the error of the oscilloscope. The data and results can be found in Table B1.

Table B1 Calculation of the error for the oscilloscope

	Kulite (HR)	Kulite (Avg8)	Honeywell (HR)	Honeywell (Avg8)
$U_{Oscilloscope,FS}$	4000 mV	4000 mV	200 mV	200 mV
N_{adc}	2^{12}	2^{9}	2^{12}	2^{9}
$U_{Sensor,FSO}$	100 mV	100 mV	5 mV	5 mV
$X_{amplifier}$	20	20	20	20
ε	± 0.05	± 0.39	± 0.05	± 0.39

As seen from the table, the accuracy was calculated for the High Resolution set up to ± 0.05%, whereas for the Average 8-function the accuracy was ± 0.39%. To obtain the total error, the bridge accuracy of ± 0.05% and the accuracies of the two different sensors, for the Honeywell sensors ± 0.25% and for the Kulite sensor ± 0.1%, have to be included. The error is calculated as the root sum of squares.

$$\varepsilon_{RSS} = \pm\sqrt{\varepsilon_{sensor}^2 + \varepsilon_{bridge}^2 + \varepsilon_{oscilloscope}^2} \qquad (30)$$

By inserting the figures for each sensor and oscillator set up the total error is obtained as shown in Table B2.

Table B2 Error for the cylinder surface pressure measurement

	Kulite XCE-093	Honeywell 176PC
High-Resolution	± 0.12%	± 0.26%
Average 8	± 0.41%	± 0.47%

The error is smaller for the High-Resolution function compared to the Average 8-function. However, for the difference between the sensors is smaller with the Average 8- function than for the High-Resolution. Summarising, the High-Resolution mode provides a more accurate output; the measurement is in the range ± 2000 Pa, which would in the worst case give an error of approximately ± 10 Pa, which must be considered acceptable.

Also, the dynamics of the sensors should be addressed. Miulus verified that the Kulite XCE-093 sensor has appropriate dynamics for the measurement environment by calculating the response time for the sensor to 8.4 µs. He concluded that at the maximum machine speed (2400 m/min) the response time is equivalent to about 0.3 mm distance at the cylinder surface (depending on the cylinder radius) which is appropriate considering that the diameter of the sensor is 2.4 mm. In the studies, however, two different sensors were used so these two will be compared. The response time for the Kulite XCE-093 sensor was the calculated 8.4 µs, whereas the same number given for the Honeywell 176PC sensor from the data sheet was 1 ms. This would, in a running speed of 1800 m/min and with a roll radius of 1500 mm, mean

approximately 30 mm distance on the cylinder surface. Consequently, during the response time, the sensor is displaced 30 mm from its original position. This means that the Honeywell sensor cannot accurately determine the pressure over the nip area and the sensor is inaccurate compared to the Kulite sensor.

To explain the noise of the sensor and the noise it is producing, the two sensors were approximated to first order systems and modelled with Matworks® MatLab Simulink. The response time is defined by the manufacturer as seen in Figure B5, so the total response time is the sum of the dead time and the time constant. The dead time is defined as the time between the pressure change and the moment when the transmitter reacts to the pressure change, shown in the figure as, $< T_d >$. The time constant, $< T_c >$, is the time when the sensor reaches 63.2% of the total change (Honeywell Process Solutions, 2012).

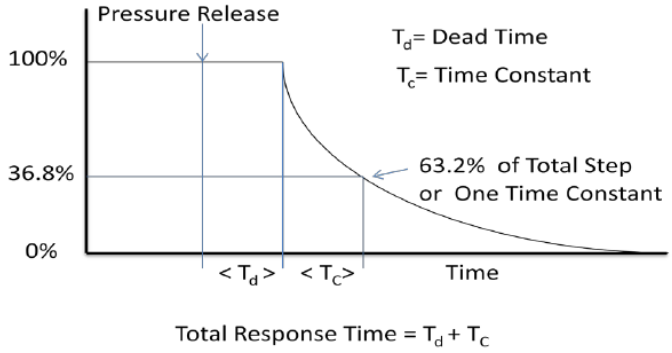

Figure B5 Response time definition given by the manufacturer (Honeywell Process Solutions, 2012)

In Häggblom, 2015, the time, when 63.2% of the step change is reached can often be approximated to the time constant of a first order system since the time constant is hard to determine using the tangent method (Häggblom, 2015, pp. 5-3). The sensors were modelled using the given response time as the time constant, assuming zero dead time. The Simulink block scheme of Figure B6**Error! Reference source not found.**.

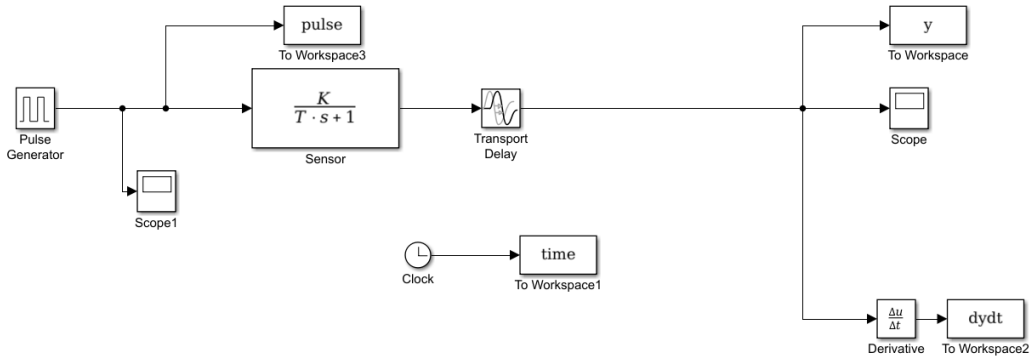

Figure B6 Simulink block scheme for the sensor.

In the data produced by the oscilloscope the time step between the outputs was 0.5 ms, which is why the systems were modelled using 0.5 ms as the width of the input signal steps and the amplitude of the steps was 5 mV. The results are illustrated in Figure B7.

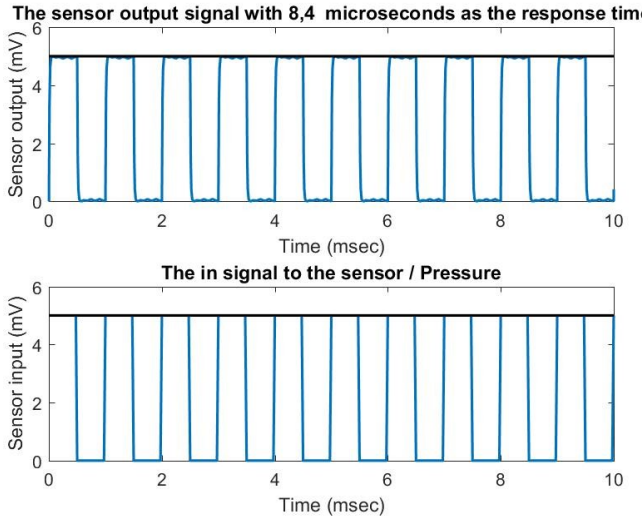

Figure B7 Simulated response to pulse changes for the sensor Kulite XCE-093.

The model is seen to follow the given signal extremely well, which would suggest that it will work well in the measuring environment. The same test was made for the model of the Honeywell sensor, but the model did not cope well with the high frequency of the pulse length so the pulse was increased to 1 ms and the results are shown in Figure B8.

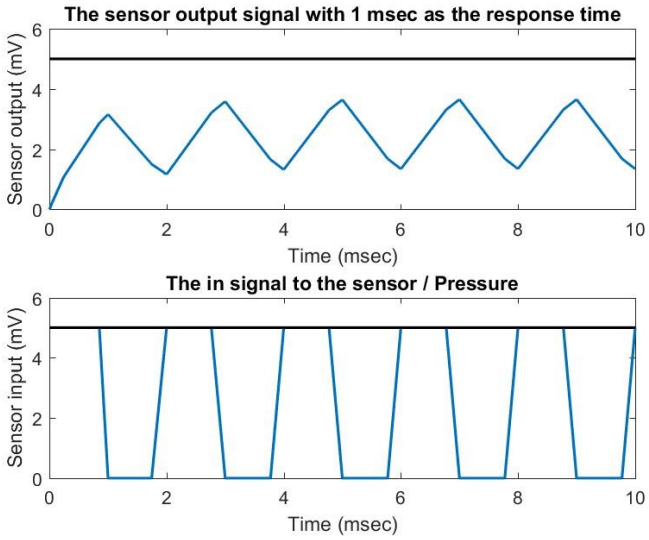

Figure B8 Simulated response of the Honeywell 176 sensor.

Clearly, the sensor does not reach the set-point value at any point and the output signal stays in the middle of the chosen range. Based on this, it can be concluded that the dynamics of the two Honeywell sensors are not good enough to provide accurate measurements. However, another question arose. Could the two sensors be good enough to determine the level of the pressure? This was studied by comparing one sensor sample sequence, which is shown in Figure B9.

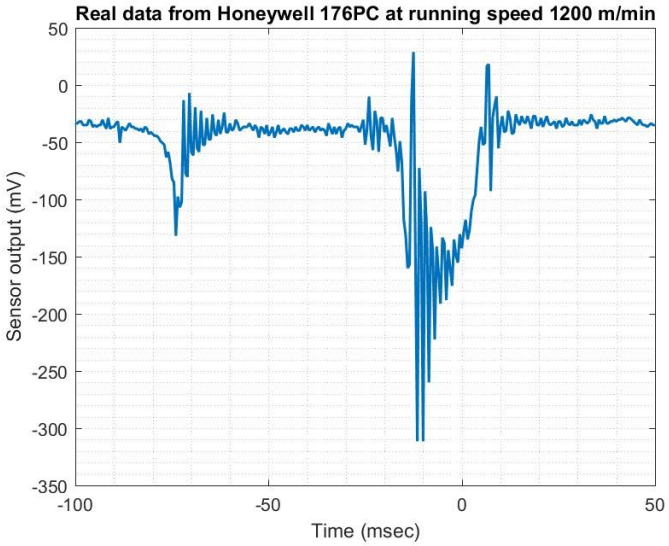

Figure B9 Real data from the Honeywell 176PC sensor

The area of interest was the impulse produced by the opening nip and whether the Honeywell sensor could produce data, which could be taken on a qualitative level. Therefore, the sensor model was tested with an impulse with the same length as the step change in the opening nip for the real data, which was 10 msec. With this impulse the following result, shown in Figure B10, was obtained.

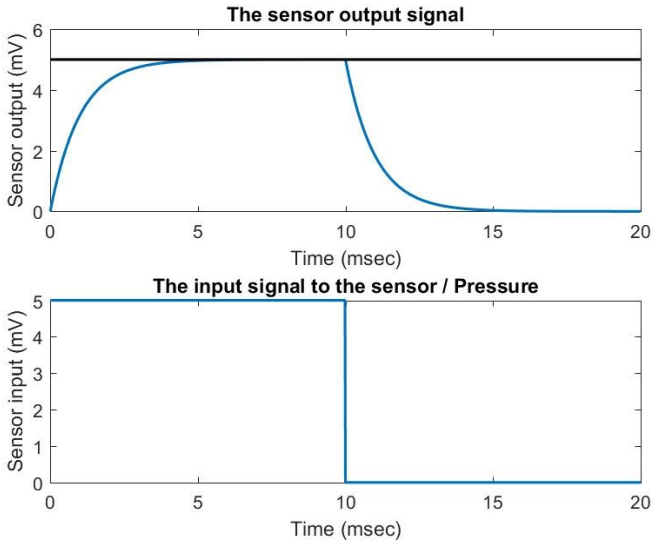

Figure B10 Time required to reach the total step change.

It can be seen that the sensor is able to reach the set-point within 6 ms, which would indicate that the dynamic is good enough to qualitatively accept the answers. Next, the model results should be compared with real data, to confirm that a first order approximation is good enough, because actual systems rarely follow a first order system behaviour. A comparison is presented in Figure B11.

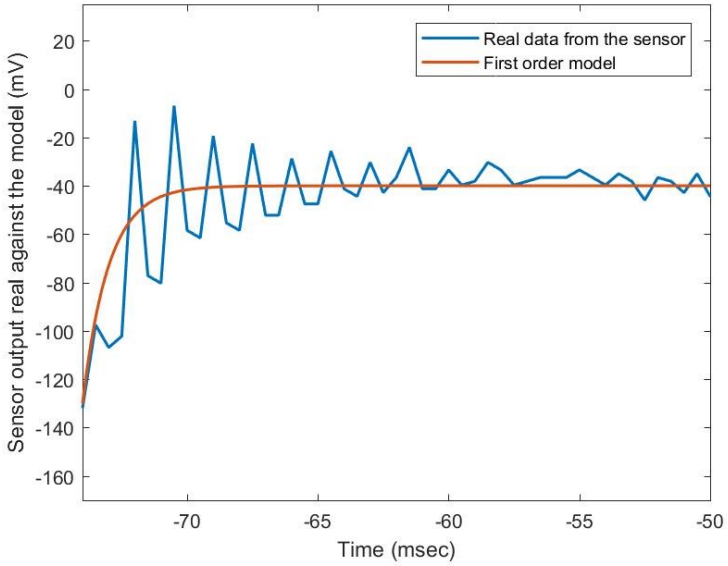

Figure B11 Comparison of real sensor data and model data

The model seems to follow relatively well the real signal, but the sensor shows relatively much noise and oscillations occur long after a large impulse, which would suggest that this is a higher order system.

Another problem discussed in Miulus, 2010, concerning the pressure sensor is creeping. After the reset of the amplifier bridge, the measuring equipment tend to differ from the installed setpoint, due to the electrical properties of the devices and temperature effects. Even a rapid change in pressures after the reset of the amplifier bridge might cause creep (Miulus, 2010, p. 40). Miulus observed that the creeping abates after a certain point in time, as seen in Figure 66. The different colours represent three consecutive tests, where the pressure was measured over a 15-minute period (Miulus, 2010, p. 42).

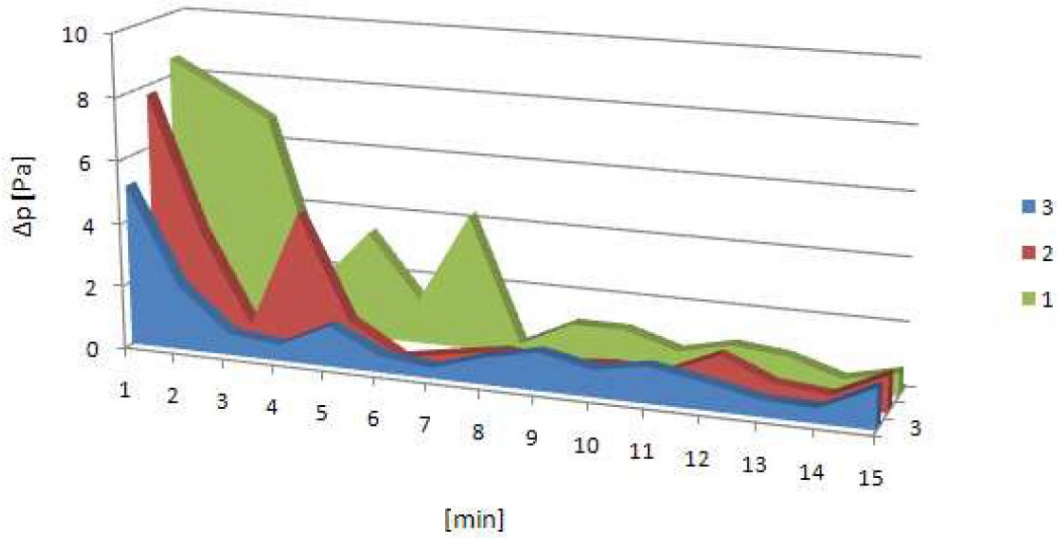

Figure 66 Decrease of sensor creeping with time (Miulus, 2010, p. 42)

Finally, Miulus recommended that the sensors be started 15 minutes before the reset of the bridge to reduce the creeping of the signal (Miulus, 2010, p. 43).

To summarise, the weak points found in the measurement system by the author and previous investigators (Miulus, 2010) are; the carbon brushes at the slip ring, the two lower response time sensors and the creep of the sensors after calibration. It is particularly difficult to determine the effects of the carbon brushes and to consider the effects in the measurement analysis is challenging. However, the sensor creep can be taken into account by normalising pressure values around a predetermined value. In these experiments the pressure values at the top of the cylinder were normalised to zero. This was additionally verified by manual measurements from the top of the cylinder using a pitot tube and the micromanometer. Due to the dynamic properties of the Honeywell sensors, the values from the sensors were taken merely as suggestive values.

APPENDIX B.2. Matlab code for data-converting

Data and algorithms for experiments.

MatLab code for converting a csv. -file and calibrating the pressure sensor results

```
%% Ella Pirttikangas Diplomarbete 22.3.2018
%Data converting from .csv to excel in right format

%clean up command window and workspace
clear all
close all
clc
format compact

%% Download data from csv-file
numfiles = 2;  %define the amount of .csv files
data = cell(1, numfiles); %define the size of the cell

for k = 1:numfiles
  filename = sprintf('scope_%d.csv', k+288); %define filename as
string
  data{k} = csvread(filename,2,0); %load and pick out the cells
end

%% Calculate the mV to Pa from the cell
datap = cell(1,numfiles); %new data cell with mV as Pa
for i = 1:numfiles
   A = data{i}; %chooses the matrix to work on
   A(:,2) = 5.8045*(A(:,2)*1000)-3.0681; %use the calibration
formula for the sensors
   A(:,3) = 5.6894*(A(:,3)*1000)-5.4456;
   A(:,4) = 22.626*(A(:,4)*1000)+17.454;
   A(:,5) = []; %deletes the trigger point from the data
   datap{i} = A;
end

%% Correction of level differences
% % Setting edge and tail to zero
for m = 1:numfiles
    S = datap{m};
    corr = 0;
    corre = corr + 230;
    corrt = corr + 400;
    S(:,2) = S(:,2)+corre;%edge
    S(:,3) = S(:,3)+corrt;%tail
    S(:,4) = S(:,4)+corr; % middle
    datap{m} = S;
end

%% Write the tables to excel sheets

%use this script part if you want to export the cell arrays to excel
%the script will write each .csv file to an own excelfile
% the first column is seconds, second is the edge, third the tail
```

```
%and the fourth is the middle

% for n = 1:numfiles
%     filename2 = sprintf('excelscope_%d.xlsx', n+445);
%     E = datap{n};
%     xlswrite(filename2,E);
% end
```

APPENDIX B.3. Kulite XCE-093 pressure sensor data sheet

kulite

HIGH TEMPERATURE MINIATURE IS® PRESSURE TRANSDUCER

XCE-093 SERIES

- Excellent Static And Dynamic Performance
- Ideal For Turbine Engine Probes
- Wide Temperature Capability -65°F To 525°F

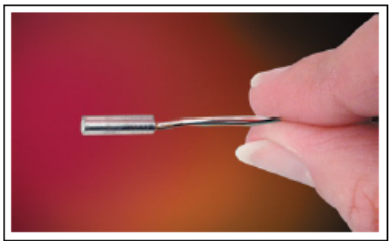

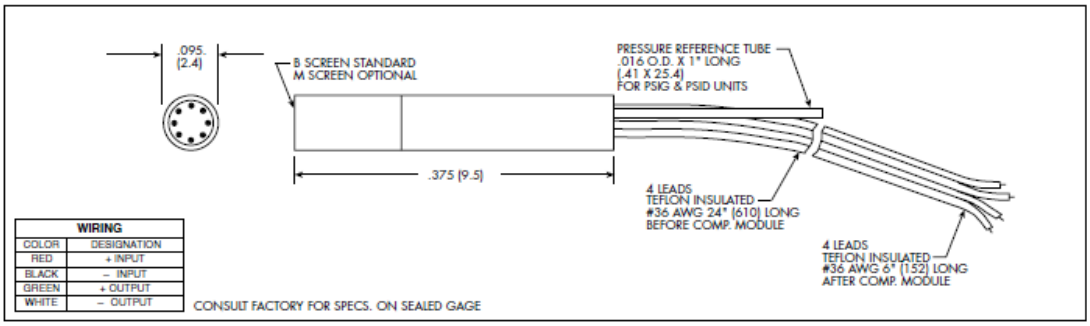

WIRING	
COLOR	DESIGNATION
RED	+ INPUT
BLACK	– INPUT
GREEN	+ OUTPUT
WHITE	– OUTPUT

CONSULT FACTORY FOR SPECS. ON SEALED GAGE

INPUT Pressure Range	0.35 5	0.7 10	1.7 25	3.5 50	7 100	17 250	35 500	70 BAR 1000 PSI
Operational Mode	Absolute, Gage, Sealed Gage, Differential					Absolute, Sealed Gage		
Over Pressure	2 Times Rated Pressure With No Change In Calibration							
Burst Pressure	3 Times Rated Pressure							
Pressure Media	All Nonconductive, Noncorrosive Liquids or Gases							
Rated Electrical Excitation	10 VDC/AC							
Maximum Electrical Excitation	15 VDC/AC							
Input Impedance	1000 Ohms (Min.)							
OUTPUT Output Impedance	1000 Ohms (Nom.)							
Full Scale Output (FSO)	100 mV (Nom.)							
Residual Unbalance	± 5 mV (Typ.)							
Combined Non-Linearity, Hysteresis and Repeatability	± 0.1% FSO BFSL (Typ.), ± 0.5% FSO (Max.)							
Resolution	Infinitesimal							
Natural Frequency (KHz) (Typ.)	150	175	240	300	380	550	700	1000
Acceleration Sensitivity % FS/g Perpendicular Transverse	1.5×10^{-3} 2.2×10^{-4}	1.0×10^{-3} 1.4×10^{-4}	5.0×10^{-4} 6.0×10^{-5}	3.0×10^{-4} 4.0×10^{-5}	1.5×10^{-4} 2.0×10^{-5}	1.0×10^{-4} 9.0×10^{-6}	6.0×10^{-5} 6.0×10^{-6}	4.5×10^{-5} 3.0×10^{-6}
Insulation Resistance	100 Megohm Min. @ 50 VDC							
ENVIRONMENTAL Operating Temperature Range	-65°F to +525°F (-55°C to +273°C)							
Compensated Temperature Range	80°F to +450°F (25°C to +235°C)							
Thermal Zero Shift	± 1% FS/100°F (Typ.)							
Thermal Sensitivity Shift	± 1% FS/100°F (Typ.)							
Steady Acceleration	10,000g. (Max.)							
Linear Vibration	10-2,000 Hz Sine, 100g. (Max.)							
PHYSICAL Electrical Connection	4 Leads 36 AWG 30" Long							
Weight	.4 Gram (Nom.) Excluding Module and Leads							
Pressure Sensing Principle	Fully Active Four Arm Wheatstone Bridge Dielectrically Isolated Silicon on Silicon							

Note: Custom pressure ranges, accuracies and mechanical configurations available. Dimensions are in inches. Dimensions in parenthesis are in millimeters. Continuous development and refinement of our products may result in specification changes without notice - all dimensions nominal. (G)

KULITE SEMICONDUCTOR PRODUCTS, INC. • One Willow Tree Road • Leonia, New Jersey 07605 • Tel: 201 461-0900 • Fax: 201 461-0990 • http://www.kulite.com

APPENDIX B.4. Honeywell 176PC pressure sensor data sheet

Pressure Sensors

170PC Series

Low Pressure Gage & Differential/Unamplified

Temperature Compensated Sensors

FEATURES

- Miniature package
- Low pressure measurement
- Calibrated Null and Span
- Temperature compensated for Span over 0 to 50°C
- Provides interchangeability

176PC SERIES PERFORMANCE CHARACTERISTICS at 10.0 ±0.01 VDC Excitation, 25°C

	Min.	Typ.	Max.	Units
Excitation	---	10	16	VDC
Null Offset	–2	0	+2	mV
Null Shift, 25° to 0°, 25° to 50°C	---	±3.0	---	mV
Sensitivity Shift, 25° to 0°, 25° to 50°C	--- ---	--- ---	±4.0[1] ±3.5[2]	%Span %Span
Repeatability & Hysteresis	---	±0.25	---	%Span
Response Time	---	---	1.0	msec
Input Resistance	---	6.3 K	---	ohms
Output Resistance	---	4.0 K	---	ohms
Stability over One Year	---	±0.5	---	%Span
Weight	---	7	---	grams

Key: 1 = 0-7", 0-14" H_2O only
2 = 0-28" H_2O only

ENVIRONMENTAL SPECIFICATIONS

Operating Temperature	–40° to +85°C (–40° to +185°F)
Storage Temperature	–55° to +125°C (–67° to +257°F)
Compensated Temperature	0° to +50°C (32° to +122°F)
Shock	MIL-STD-202, Method 213 (150 g, half sine, 11 msec)
Vibration	MIL-STD-202, Method 204 (10 to 2000 Hz at 20 g)
Media	P2 port Wetted materials; polyester housing, epoxy adhesive, silicon, borosilicate glass, and silicon-to-glass bond*
	P1 port Dry gases only

* Liquid media containing some highly ionic solutions could potentially neutralize the chip-to-glass tube bond.

ELECTRICAL CONNECTIONS

(Internal Circuitry Shown)

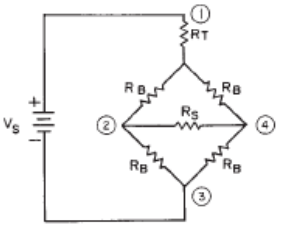

NOTES

1. Circled numbers refer to sensor termination.
2. $V_o = V_2 - V_4$ (referenced to pin 3).
3. R_B = Strain gage resistors (~4.8 kΩ).
4. R_T = Sensitivity temperature compensation resistor.
5. R_S = Sensitivity calibration resistor.

When a positive pressure is applied to port P2, the differential voltage $V_2 - V_4$ (voltage at pin 2, with respect to ground, increases and voltage at pin 4 decreases) increases linearly with respect to the input pressure. When a vacuum pressure is pulled at port P2 (or positive pressure applied to port P1) the voltage $V_2 - V_4$ decreases linearly with respect to the input pressure.

176PC SERIES ORDER GUIDE

Catalog Listing	Pressure Range H_2O	Span, mV			Sensitivity mV/"H_2O	Overpressure "H_2O	Linearity, %Span	
		Min.	Typ.	Max.	Typ.	Max.	P2 > P1 Max.	P2 < P1 Max.
176PC07HG2	0-7	26	28	30	4.00	140	±3.00	±1.50
176PC07HD2	0-7	26	28	30	4.00	140	±3.00	±1.50
176PC14HG2	0-14	33	35	37	2.50	140	±3.00	±1.50
176PC14HD2	0-14	33	35	37	2.50	140	±3.00	±1.50

Unamplified

APPENDIX B.5. Mikor Micromanometer TT370S data sheet

ASSOCIATED INSTRUMENTS REPAIRS

SUPPLIERS OF INSTRUMENTS AND CONSUMABLES

CALIBRATION AND REPAIR SERVICE AVAILABLE

T T SERIES MICROMANOMETERS

for Measurement of Air Velocity and Pressure Positive Negative or Differential

Applications: These hand held digital micromanometers are compact lightweight bidirectional battery operated units with excellent stability and resolution. The very wide range of applications will include:

1. HVAC Commissioning and maintenance
2. Gas flow measurement in land fill operations
3. Aerodynamics and air flow research
4. COSHH requirements relating to air flow and pressure
5. Furnace draught measurement
6. Paint booth and clean room pressure measurement

General Specification:

Instrument Dimensions	45 x 92 x 185mm
Instrument Weight (approx)	400 grams
Power Source (dry battery)	9 Volt IEC6LR61 (PP3 etc)
Power Source (rechargeable)	8.4 volt 120mAh NI MH
Battery Life (alkaline dry)	Approx 120 hours
Battery Life (rechargeable)	Approx 30 hours with full charge
Recharge Time	18 / 20 hours
Electrical Output Signal	1 mV per displayed count
Electrical Output Impedance	2000 Ω
Safe Line / Differential Pres	15kPa
System Air Leakage (typical)	0.1ml/minute at 5kPa
Operational Temp Limits	5° to 45°c
Storage Temp Limits	-5° to + 50°c
Short Term Temp Limits	-10° to + 55°c (30 minutes)

Models	TT 370S / TT 470S
Ranges	199.9 Pascals
Pressure	1999 Pascals
	7.00 kPa
Velocity	1.2 - 100 m/sec
Models	TT 370M / TT 470M
Ranges	19.99 mm H20
Pressure	199.9 mm H20
	700 mm H20
Velocity	1.2 - 100 m/sec
Models	TT 370B / TT 470B
Ranges	1.999 millibar
Pressure	19.99 millibar
	70.0 millibar
Velocity	1.2 - 100 m/sec
Models	TT 370A / TT 470A
Ranges	1.999 in H20
Pressure	19.99 in H20
	30.0 in H20
Velocity	240 - 19990 ft/min

Accuracy Specification:

Accuracy at 20°c (all ranges)	
Readings > 100 counts	1% of reading ± 1 count
Readings < 100 counts	± 2 counts
Span Temperature Coefficient	Better than 0.1% /°c (any range)
Zero Drift	(1 minute warm up) Negligible due to autozero system
Zero System Accuracy	± 1 count (any range)
Orientation Effect	(any 45° change) 0.1 Pa typical
Electrical Output	(10MΩ load) 1mV displayed count ± 0.3%

Accessories:

3m clear and 3 m brown flexible tubing. Tubing adaptors. Jack plug. Cradle. Carrying Case. Charger for rechargeable instrument. Instruction Manual.

NOTES: TT 3xxx Instruments have a density correction facility on the velocity range.
TT 4xxx Instruments have the velocity range calibrated for standard air.
All instruments have a bipolar pressure measurement capability.
Velocity readings must be POSITIVE. NEGATIVE velocity readings not valid.
TT 370A / 470A instruments display velocity in steps of 10ft/min due to the limitations of the display (max count 1999).
For example a velocity of 5680ft/min will be displayed as 568. Therefore FT/MIN = Reading x 10.
In view of our continuous programme of improvement we reserve the right to change the specification, colour range and price for any item described. Prices excludes VAT.

Unit 3 Monument Ind. Pk. Chalgrove Oxford OX44 7RW Tel/Fax 01865 891700 / 400240

APPENDIX C: Regression analysis on the closing nip over-pressure

The simulations in Chapter 5 described the behaviour along the cylinder, but due to the complicated behaviour of the closing nip, simulations on these conditions could not be made. The quantity of obtained data could however be enough to build a model based on linear regression.

The linear regression model is built for the smooth and the modified roll, because the concepts have the same stabiliser, which reduces the number of predictors in the regression. The aim is to determine, how much the velocity will influence the static pressure in the nip and how much the pressure decrease by the nozzle will affect the end pressure. Thus, the predictors of the models are the velocity and the pressure at the nozzle. Three regression models are developed; one for the smooth roll concept, one for the modified surface D and one for both.

APPENDIX C.1. The results from the regression analysis

The data matrix for the smooth roll regression model consists of 25 observations with the same size of the response vector with the closing nip pressures:

$$y = b_0 + b_1 x_1 + b_2 x_2 \qquad (31)$$

where x_1 is the machine speed (m/s) and x_2 is the pressure after the nozzle (Pa). The model with the modified surface is based on the same linear model, but the number of observations is 20. The estimators of the smooth roll regression are:

Table C1 Estimators for the linear smooth roll regression.

b_0	-356.98
b_1	43.47
b_2	1.1

The estimator for the machine speed predictor is clearly the more determining factor compared to the pressure at the nozzle, of course depending on the variables chosen to the regression. The increase of one unit in the speed will increase, according to the model, the closing nip pressure by approximately 40 Pa, whereas the relation between the pressure at the nozzle and the pressure at the nip is almost proportional. The estimate and the real response is illustrated in Figure C1, which shows that the model is steeper in the machine speed direction than in the nozzle pressure direction.

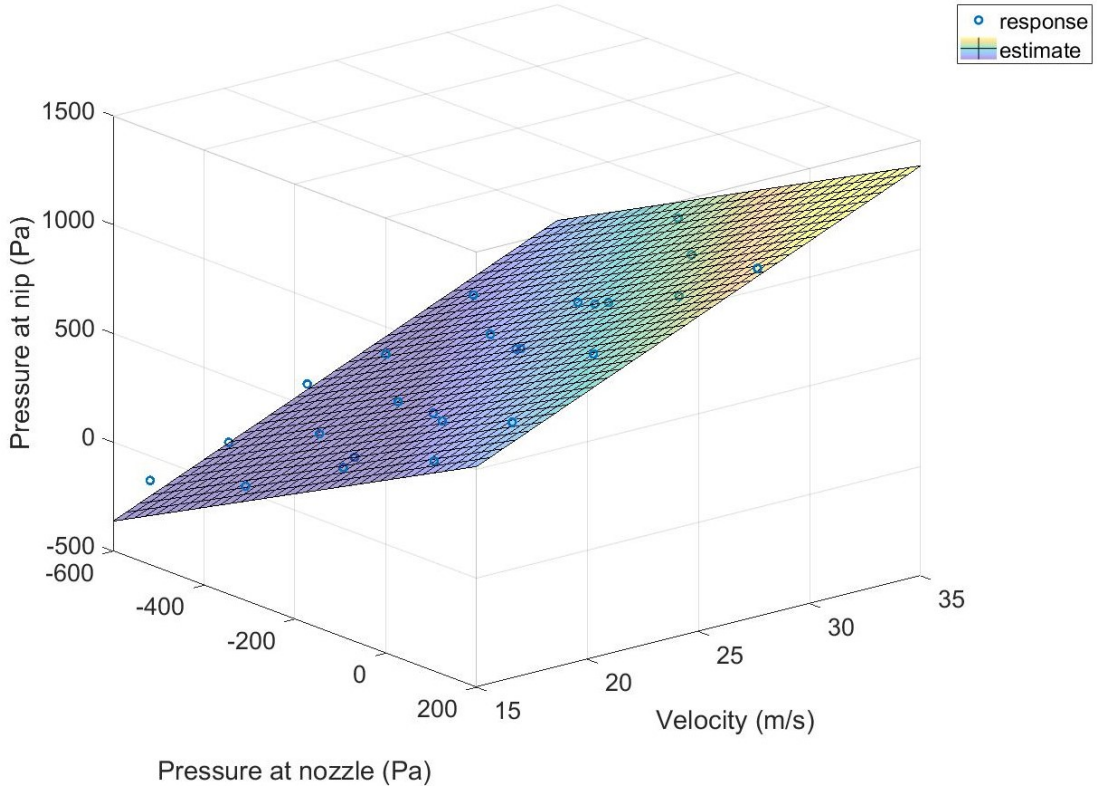

Figure C1 Estimate and response for the linear regression of the smooth roll.

What can be predicted from the results discussed in Chapter 8, is that the results for the grooved roll are less dependent on the speed as the angular coefficient is smaller. For the linear regression of the modified surface, the estimators are reported in Table C2.

Table C2 Estimators for the linear regression of the modified roll.

b_0	-99.21
b_1	9.98
b_2	0.76

The estimators are smaller compared to the smooth roll and the model is less steep with respect to both predictors, which is also presented in Figure C2.

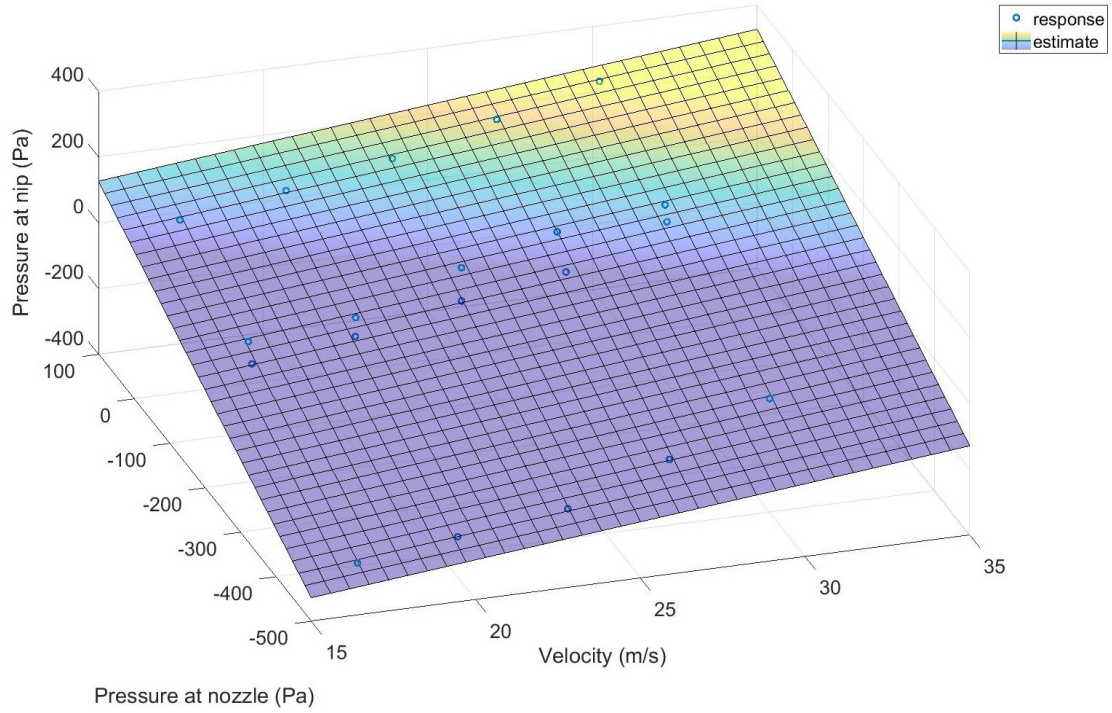

Figure C2 Estimates and real response for the linear regression of the modified roll.

Clearly, the modified surface is less dependent on the predictors and the closing nip pressure will be significantly lower for the modified surface. When the two cylinders are combined in a linear model using a binary variable and the same predictor the linear model is

$$y = b_0 + b_1x_1 + b_2x_2 + b_3x_3 + b_4x_4 \qquad (32)$$

The additional predictors are the binary values for the smooth roll x_3 and the modified roll x_4. The angular coefficients will be the same for the speed and pressure predictors,

which provides information of the impact of the two cylinders. The estimators are presented in Table C3.

Table C3 Estimators for linear model of the two cylinders

b_0	-30.51
b_1	28.43
b_2	0.99
b_3	0
b_4	-460.69

The estimator b_4 is significantly below zero, which suggest that the modified surface will lower the closing nip pressure by more than 400 Pa. The difference is illustrated in Figure C3. The response for the modified surface is much lower compared to the response with the smooth roll, which represents the benefits of having a modified surface compared to a regular smooth surface.

Because the angular components are the same for the both cylinders the estimate does not fit as well as it did for the models with merely one surface type.

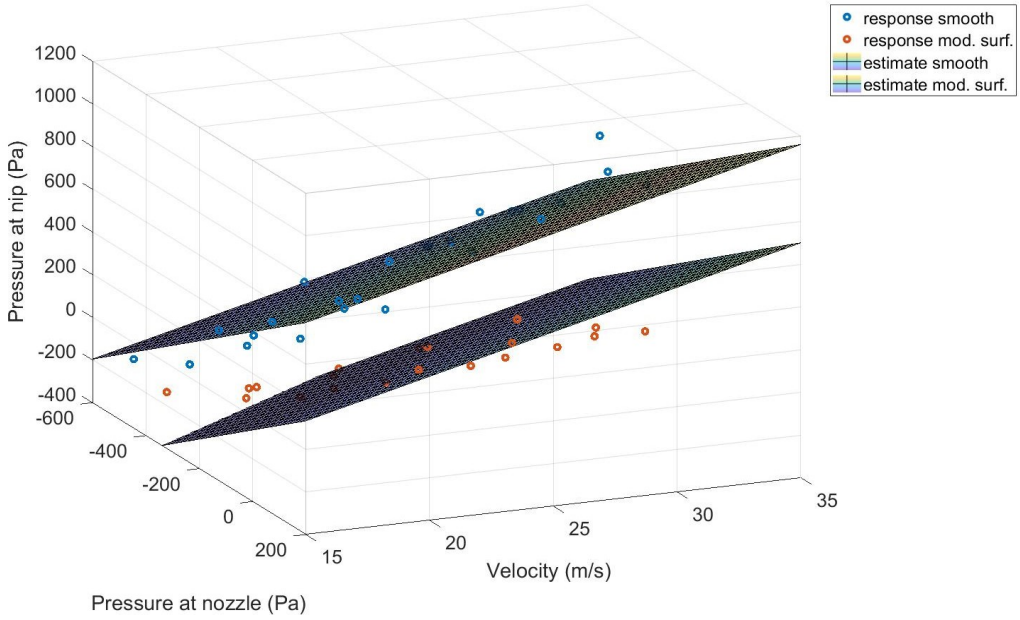

Figure C3 Estimate for the combined model and the real response.

APPENDIX C.2. The evaluation and validation of the linear models

In order to know whether the regression models are reliable or not, their significances and the data itself should be assessed. The significance of the models is determined the Coefficient of Determination (R^2), which is the ratio between the total sum of squares for the data and the sum of squares due to the regression (Draper & Smith, 1998). In other words, the R^2-values defines how well the regression model fits the data. The R^2-value can be between zero and one and typically the value should be between 0.85-0.95. This is because the risk for an over predicted model increases, especially if the number of predictors is high compared to the number of observations (Skjäl, 2016). The significance of the model is described by the p-value, which should be lower than the α-level chosen. The α-level refers to the likelihood that the test value will be outside of the confidence interval, this value is usually $\alpha = 0.05$. For good significance the p-value should be approximately 20% lower than the chosen α-level. These values are depicted in Table C4.

Table C4 Model evaluation figures.

	Smooth roll	Modified roll	Combined
CoD (R^2)	0.96	0.96	0.90
Significance (p-value)	$1.36 \cdot 10^{-16}$	$1.33 \cdot 10^{-12}$	$2.3 \cdot 10^{-21}$

All the models developed satisfy the R^2-value limits, but the smooth and modified roll have a somewhat high Coefficient of Determination, which anyway is acceptable, since the number of parameters is much less than the number of observations. The p-values for all models fulfil the limit of being over 20% lower than the α-level, which suggest that all the models are significant.

The model is evaluated to satisfy the common statistical values, but in addition to the model validation, the predictors' significance and the errors of the estimators can be discussed. These values are presented in Table C5. The standard error is for the estimators (b_1 and b_2) and the p-values are for the predictors (x_1 and x_2).

Table 7 Values for the determination of significant predictors.

	Machine speed (x_1)			Pressure at the nozzle (x_2)		
	Smooth roll	Modified roll	Combined	Smooth roll	Modified roll	Combined
Standard error	2.97	1.56	3.44	0.063	0.04	0.08
p-value	$7.9 \cdot 10^{-13}$	$6.9 \cdot 10^{-6}$	$2.8 \cdot 10^{-10}$	$2.3 \cdot 10^{-14}$	$1.5 \cdot 10^{-12}$	$1.9 \cdot 10^{-15}$

The standard error of the estimators is acceptable with respect to the uncertainties of the measurements made in the trials and the p-values are all smaller than the α-level. Thus, the predictors are all significant according to the limits.

The model fitted the data well according to the R^2-value, but the residuals can be still analysed to determine, if the data has outliers, which could reduce the reliability of the models. The Cook's distance is used to determine the validity of data points and for finding outliers in the data and defining the leverage of the single data points. The leverage expresses the impact of the single data point on the regression model and when a data point has a high Cook's distance the data point can be considered as an outlier. The leverage and the residuals are presented in the Figure C4.

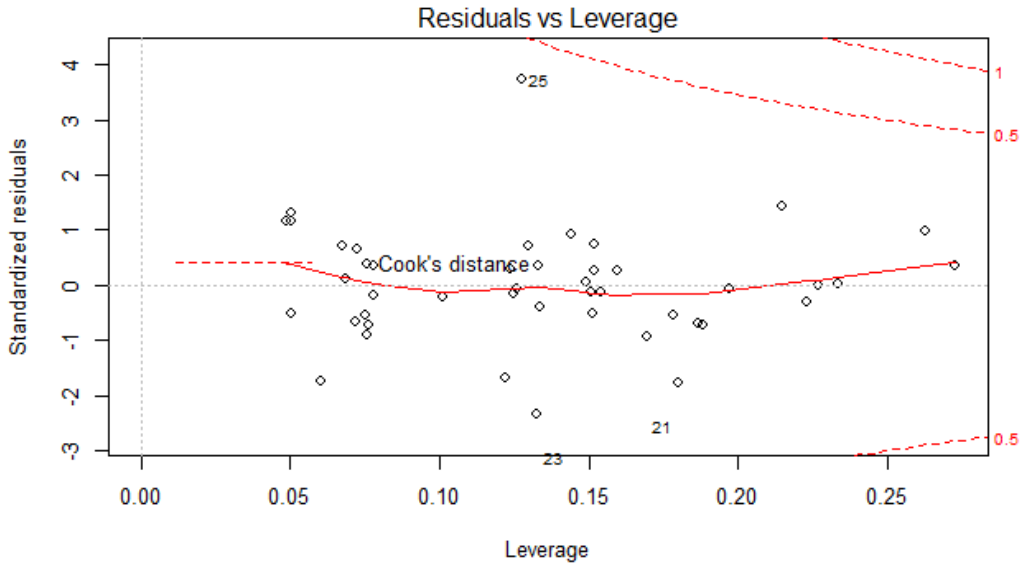

Figure C4 Residuals vs. Leverage.

All the data points lie inside of the 0.5 distance, which indicates that there is no clear outliers, but data points 21, 23 and 25 have the highest distances. The reason for the large distances can be due to the measurements at the trial machine. The possible outliers ought to be studied closer, therefore Figure C5 is illustrated where the fitted pressure values and the residual are shown. The residuals appear to increase as the nip pressures increase. This behaviour is undesired, since it indicates that the model gets less accurate as the nip pressure becomes higher. It ought to be kept in mind that the model is linear, which is likely not the case in the real system. Karlssons (1989) model for the opening nip included a logarithmic factor, which could explain the poor prediction at higher velocities with the linear model.

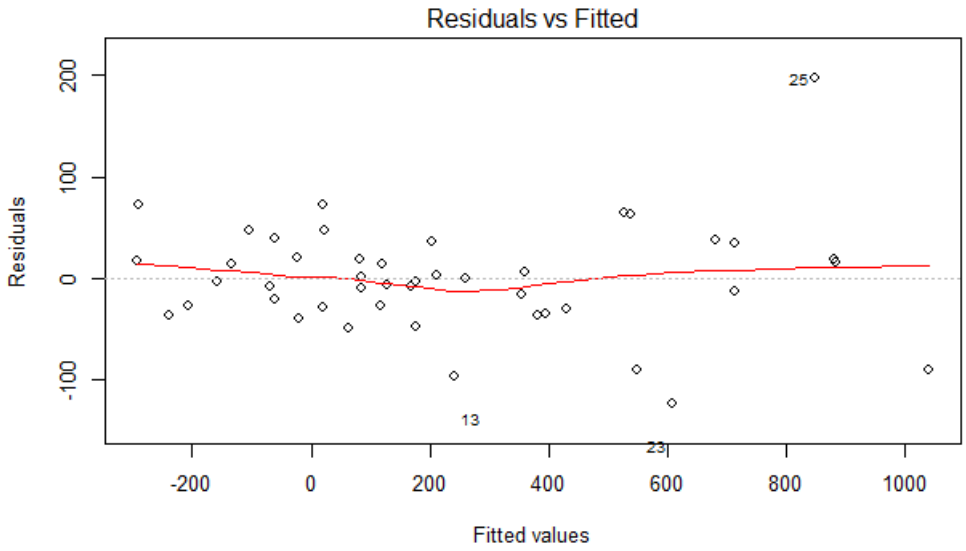

Figure C5 Residual vs. fitted values.

To improve the prediction at nip pressures over 400 Pa, more data points should be obtained from this interval because the residuals are very dispersed and the number of data points than for the lower velocities.

The linear regression models appear to fulfil the central limits and the models could be used as approximative tools for determining the pressure at the nip for different nozzle pressures and velocity of the boundary layer. Naturally, the regression models do not take any other predictors into account and the models are not usable always, since the pressures in the nip is also dependent on the stabiliser used, the radius of the roll and a variety of other variables discussed within this thesis.